การประเมินและตรวจสอบลำอนุภาคระยะใกล้ด้านหลังมอดูเลเตอร์แบบพิมพ์สามมิติสำหรับการบำบัดด้วยลำโปรตอน

นางสาววริศรา จารุจินดา

วิทยานิพนธ์นี้เป็นส่วนหนึ่งของการศึกษาตามหลักสูตรปริญญาวิทยาศาสตร์มหาบัณฑิต
สาขาวิชาฟิสิกส์ ภาควิชาฟิสิกส์
คณะวิทยาศาสตร์ จุฬาลงกรณ์มหาวิทยาลัย
ปีการศึกษา 2564

EVALUATION AND ASSESSMENT OF THE NEAR FIELD BEHIND 3D PRINTED-MODULATORS FOR PROTON BEAM THERAPY

Ms. Warisara Charuchinda

A Thesis Submitted in Partial Fulfillment of the Requirements

for the Degree of Master of Science Program in Physics

Department of Physics

Faculty of Science

Chulalongkorn University

Academic Year 2021

Thesis Title	EVALUATION AND ASSESSMENT OF THE NEAR FIELD BEHIND 3D PRINTED-MODULATORS FOR PROTON BEAM THERAPY
By	Ms. Warisara Charuchinda
Field of Study	Physics
Thesis Advisor	Assistant Professor Narumon Suwonjandee, Ph.D.
Thesis Co-advisor	Assistant Professor Burin Asavapibhop, Ph.D.
	Uli Weber, Dr.rer.nat.

Accepted by the Faculty of Science, Chulalongkorn University in Partial Fulfillment of the Requirements for the Master's Degree

Dean of the Faculty of Science

. . . . . .

(Professor Polkit Sangvanich, Ph.D.)

THESIS COMMITTEE

. . . . . Chairman

(Associate Professor Nakorn Phaisangittisakul, Ph.D.)

. . . . . Thesis Advisor

(Assistant Professor Narumon Suwonjandee, Ph.D.)

. . . . . Thesis Co-advisor

(Assistant Professor Burin Asavapibhop, Ph.D.)

. . . . . Thesis Co-advisor

(Uli Weber, Dr.rer.nat.)

. . . . . Examiner

(Chayanit Asawatangtrakuldee, Ph.D.)

. . . . . External Examiner

(Assistant Professor Chinorat Kobdaj, Ph.D.)

วริศรา จารุจินดา: การประเมินและตรวจสอบลำอนุภาคระยะใกล้ด้านหลังมอดูเลเตอร์แบบพิมพ์สามมิติสำหรับการบำบัดด้วยลำโปรตอน. (EVALUATION AND ASSESSMENT OF THE NEAR FIELD BEHIND 3D PRINTED-MODULATORS FOR PROTON BEAM THERAPY) อ.ที่ปรึกษาวิทยานิพนธ์หลัก : ผศ. ดร. นฤมล สุวรรณจันทร์ดี, อ.ที่ปรึกษาวิทยานิพนธ์ร่วม : ผศ. ดร. บุรินทร์ อัศวพิภพ, ดร. อูลี เวเบอร์ 99 หน้า.

มอดูเลเตอร์แบบพิมพ์สามมิติเป็นนวัตกรรมที่พัฒนาขึ้นสำหรับระบบนำส่งลำอนุภาคที่ใช้ในการรักษาโรคมะเร็ง ซึ่งสามารถช่วยกระจายปริมาณรังสีให้ครอบคลุมทั่วทั้งบริเวณเนื้องอกอย่างสม่ำเสมอได้ในระยะเวลาอันสั้น ในแผนการรักษาแบบปกติ มอดูเลเตอร์จะถูกวางอยู่ในตำแหน่งที่ห่างจากผู้ป่วยเพื่อหลีกเลี่ยงความไม่สม่ำเสมอของลำอนุภาคซึ่งเกิดจากการที่อนุภาคเดินทางผ่านโครงสร้างของมอดูเลเตอร์ อย่างไรก็ตาม การจัดวางมอดูเลเตอร์ในระยะใกล้กับผู้ป่วยอาจช่วยให้ปริมาณรังสีมีความสอดคล้องกับรูปร่างของเนื้องอกมากขึ้น วิทยานิพนธ์นี้จึงนำเสนอการศึกษาความไม่สม่ำเสมอของลำอนุภาคโปรตอนที่เกิดจากโครงสร้างของมอดูเลเตอร์แบบพิมพ์สามมิติด้วยโปรแกรมมอนติคาร์โล FLUKA เพื่อหาระยะที่ใกล้ที่สุดที่จะสามารถวางมอดูเลเตอร์ได้โดยยังคงความสม่ำเสมอของปริมาณรังสีที่ตกกระทบผิวของผู้ป่วย FLUKA user routine ได้ถูกพัฒนาและปรับปรุงให้ใช้เวลาน้อยลงในการจำลองโครงสร้างที่ซับซ้อนของมอดูเลเตอร์แบบพิมพ์สามมิติ นอกจากนั้นความไม่สม่ำเสมอของลำอนุภาคยังถูกทดสอบด้วยตัวแปรต่าง ๆ ซึ่งพบว่ามีการตอบสนองอย่างมากต่อการเปลี่ยนแปลงของพลังงานของอนุภาคและระยะห่างระหว่างเข็มของมอดูเลเตอร์ ผลจากการวัดปริมาณรังสีด้วย radiochromic film ยังแสดงความสอดคล้องกับผลจากการจำลองด้วยโปรแกรม FLUKA เป็นอย่างดี นอกจากนั้นวิทยานิพนธ์นี้เสนอการจัดวางมอดูเลเตอร์ในระยะใกล้กับผู้ป่วยเพื่อใช้ประโยชน์จากความไม่สม่ำเสมอของปริมาณรังสีที่เกิดขึ้นด้านหน้าของเนื้องอกซึ่งอาจช่วยถนอมเนื้อเยื่อดีส่วนหน้าได้ และเพื่อที่จะใช้ประโยชน์จากการจัดวางมอดูเลเตอร์ระยะใกล้โดยปราศจากการรบกวนของความไม่สม่ำเสมอของปริมาณรังสี ณ บริเวณเนื้องอก พลังงานที่ใช้จะต้องมีค่าไม่ต่ำกว่า 150 MeV สำหรับกรณีการรักษาเนื้องอกที่มีขนาด 5 เซนติเมตร

ภาควิชา	ฟิสิกส์	ลายมือชื่อนิสิต	.....
สาขาวิชา	ฟิสิกส์	ลายมือชื่อ อ.ที่ปรึกษาหลัก	.....
ปีการศึกษา	2564	ลายมือชื่อ.ที่ปรึกษาร่วม	.....
			.....

6270101123: MAJOR PHYSICS
KEYWORDS: PROTON THERAPY / 3D-PRINTED MODULATORS / MONTE CARLO SIMULATION / FLUENCE AND DOSE INHOMOGENEITIES

WARISARA CHARUCHINDA : EVALUATION AND ASSESSMENT OF THE NEAR FIELD BEHIND 3D PRINTED-MODULATORS FOR PROTON BEAM THERAPY. ADVISOR : ASST. PROF. NARUMON SUWONJANDEE, Ph.D., THESIS COADVISOR : ASST. PROF. BURIN ASAVAPIBHOP, Ph.D., ULI WEBER, Dr.rer.nat., 99 pp.

A 3D-printed modulator is an innovation developed for particle therapy delivery systems that enables a highly conformal and homogeneous dose distribution around the tumor within a very short irradiation time. In normal cases, the modulators are positioned far from the patient in order to avoid the field inhomogeneity resulting from the periodic structure of the modulators on patient's skin. However, a smaller distance between the modulator and patient would provide a better dose conformation in the target volume. In this thesis, the FLUKA Monte Carlo simulation program was used to investigate the fluence distributions of protons penetrating through 3D-printed modulators and to determine the minimum distance at which the dose is homogeneous on patient's skin. To implement the complex geometry of the 3D-printed modulator in FLUKA, a dedicated FLUKA user routine with a shorter run time was developed. The sensitivity of the fluence ripple was also tested and found to be strongly dependent on the initial beam energy and the pin period of the modulator. The results of radiochromic film and dose measurements show a qualitatively good agreement with the FLUKA simulations. Furthermore, this thesis introduces the idea of the short distance of the modulator setup which could exploit strong dose inhomogeneities induced by the 3D-printed modulator for normal-tissue sparing. The minimum energy, which can utilize the advantages of the small distance setup without the interference of the dose inhomogeneity in the tumor, is 150 MeV for a tumor with a maximum width of 5 cm.

Department:	Physics	Student's Signature	.....
Field of Study:	Physics	Advisor's Signature	.....
Academic Year:	2021	Co-advisor's signature	.....
			.....

Acknowledgements

First of all, I would like to express my most sincere gratitude to Asst. Prof. Dr. Narumon Suwonjandee and Asst. Prof. Dr. Burin Asavapibhop for introducing me to the field of radiotherapy, which enabled me to apply fundamental physics knowledge to help human life. Apart from their great support and encouragement since I was an undergraduate student, their academic and personal advice also motivates me to grow and improve myself in every aspect of my life.

I would like to show my great appreciation to Dr. Uli Weber who accepted and trusted me to work on his research topic in his research group at GSI Helmholtzzentrum für Schwerionenforschung. I would like to thank him for his dedication to giving me the best experience I could obtain from the internship. Even with his regular tight schedule as a group leader, I am really grateful for the time that he spent to supervise me on my research project in this thesis.

I gratefully acknowledge Assoc. Prof. Dr. Nakorn Phaisangittisakul, Dr. Chayanit Asawatangtrakuldee, and Asst. Prof. Dr. Chinorat Kobdaj for serving on my thesis committee. I am grateful for their insightful comments and suggestions that were very helpful in improving my thesis to its best form.

In particular, I would like to thank Dr. Felix Ernst Horst for helping me shape up this thesis from the start to the end. I would like to thank him for his enthusiastic response to my questions, the discussion concerning the technical issue, and his assistance with proofreading. I also would like to thank Dr. Christoph Schuy and Dr. Claire-Anne Reidel from the radiation physics group of GSI, Prof. Dr. Klemens Zink, Yuri Simeonov and Petar Penchev from the Institut für Medizinische Physik und Strahlenschutz, Technische Hochschule Mittelhessen, Dr. Mateusz Sitarz and Dr. Per Poulsen from the Danish Center for Particle Therapy (DCPT), and Dr. Simon Busold, Dr. Michael Folkerts and Dr.Michael Folkerts from Varian Medical System, for allowing me to use their experimental data and for providing me the information for the simulation.

This work is supported by the Development and Promotion of Science and Technology Talents Project (DPST) scholarship, the Association for the Promotion of Tumor Therapy with Heavy Ions e.V., and the GET_INvolved Programme.

CONTENTS

Page

Page

LIST OF FIGURES

Figure **Page**

Page

Page

Page

Chapter I

INTRODUCTION

Cancer is the second leading cause of death worldwide. It was reported that 10 million deaths in 2020 were caused by cancer and the diagnoses continue to be on the rise for decades, even among young people (WHO). To relieve the burden, the knowledge of prevention and treatment strategies has been improving unstoppably with the cooperation of physicians and scientists. Radiotherapy is one of the cancer treatment methods that more than half of all patients receive as part of their treatment, either as the only primary treatment or in combination with other treatments like surgery or chemotherapy. Apart from high-energy photons, which are commonly used in clinics as conventional radiation therapy, heavy-charged particles, i.e., protons and heavy-ions, have gained attention in the past decades due to their favorable physical dose transfer characteristics for radiotherapy (Newhauser and Zhang, 2015; Schardt et al., 2010) (dose in the meaning of radiotherapy is the energy deposited in matter per unit mass, which is usually in a unit of J/kg as known as Gy). In contrast to photons, whose dose is almost equally distributed both at proximal and distal parts of the tumour, heavy-charged particles, i.e., protons and heavy ions, have the advantage that they can transfer the maximum dose exactly at the position of the tumour target, right before they stop moving. Those properties serve the cancer treatment goal when high precision dose delivery is needed, especially in the case of a deep-seated or vital organ-surrounded tumours.

Because of the maximum dose planned for eradicating the tumour, even a small dose displacement would cause severe damage to the surrounding normal tissue. Hence, one of the main tasks in particle therapy is the development of beam delivery techniques for achieving precisely conformal and homogeneous dose in the target volume. The two basic techniques which are commonly used are “passive scattering” (Chu et al., 1993; Torikoshi et al., 2007) and “pencil beam scanning” (Haberer et al., 1993; Pedroni et al., 1995). However, these two methods have some drawbacks: passive scattering causes beam loss from the scattering devices and production of secondary neutrons, and active scanning takes relatively long treatment time due to energy layer switching. So, some advanced innovations have been developed additionally. One of the techniques that have been introduced is the use of pencil scanning technique with an application of a static device, i.e., a “3D-printed

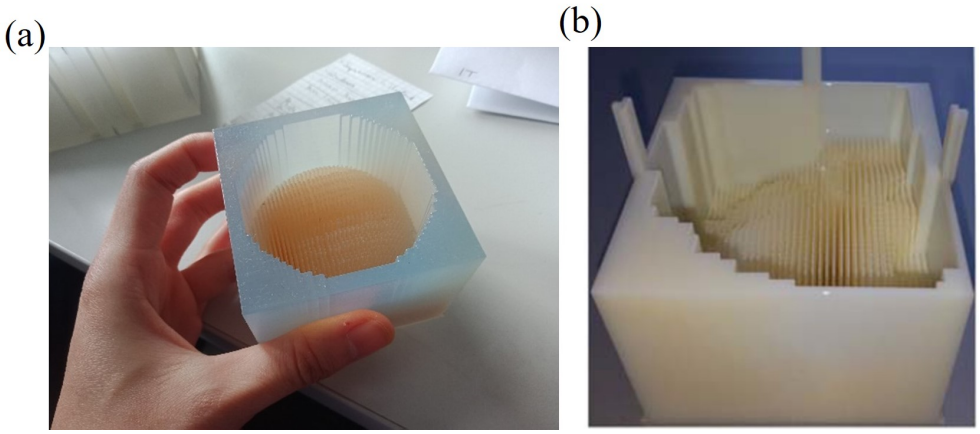

Figure 1.1: Prototypes of the 3D-printed modulators for (a) a spherical target and designed specifically for (b) a lung tumour (Simeonov et al., 2022).

modulator" (Simeonov et al., 2017, 2022). The device is a combination of a range compensator and a ridge filter (Chu et al., 1993), which consists of many different pyramid structures (pins) with a well-defined profile that is optimized to deliver a conformal dose in a specific target volume. The examples of the 3D-printed modulators are shown in Figure 1.1. Due to the fast total irradiation time of 3D-printed modulator modality, it is promising to be applied for clinical use in the near future, especially for the fast treatment of the mobile tumour (Simeonov et al., 2022). Moreover, it is considered to be one of the most possible options to perform FLASH therapy (Favaudon et al., 2014; Jolly et al., 2020; Weber et al., 2022; Tinganelli et al., 2022b) which is in the spotlight of radio-oncology research at the moment.

A particular effect induced by the periodic fine structure of the modulator in ion beam therapy is the inhomogeneous field, i.e., fluence and dose, in the near field region (Ringbæk et al., 2014). Because it might cause strong dose inhomogeneities on the skin, in the proximal normal tissue, or even in the target volume, modulators are normally placed far away from the target. Nevertheless, if one desires to achieve the best efficiency for the treatment, the devices should be kept as close as possible to the target to prevent losing dose conformity in the target volume. Thus, the first objective of this work is to validate the determination method of the "minimum distance" behind the modulator at the exact position where the inhomogeneous field completely disappears. The main tool used for this study is the Monte Carlo simulation package FLUKA (Böhlen et al., 2014) which was used to score fluence and dose distributions in air and water. Moreover, this fluence oscillating pattern was also investigated and its sensitivity was tested by the possible variables, i.e., initial

energies and angular spread of the beam, and pin period of the modulator.

The second part of the thesis describes the validation of the FLUKA simulation results by the experimental data. We performed these simulations for the purpose of comparing results from radiochromic film measurements, which were conducted to observe the modulated beam field behind the 3D-printed modulator as well as to measure the dose distribution in the water phantom. The geometry of the setup and the magnetic scanning of the proton beam was precisely considered here.

Even though the dose inhomogeneities are usually avoided for the normal treatment plan, the research on "minibeam particle therapy" (Meyer et al., 2019) suggests the opposite by using the fractionated beam to reduce the damage to the patient's skin while maintaining the tumour control efficiency. This inspired the idea of exploiting the field inhomogeneities induced by the 3D-printed modulators to spare the normal tissues. If this hypothesis turned out to be true, it would have a second advantage, because then the modulator could be placed close to the patients resulting in reducing the scattering effect and therefore improving the dose conformity to the tumour. This leads us to the last part of the thesis. The near field inhomogeneities in the target for a clinical setup were simulated and investigated.

Chapter II

THEORETICAL BACKGROUND

2.1 Interaction of Protons with Matter

All charged particles whose mass is equal to or heavier than an atomic mass unit are categorized as "heavy-charged particles", i.e., protons and heavy ions. Because of their much heavier mass compared to an electron (a proton is roughly 1840 times heavier than an electron), heavy-charged particles have partly similar physical interaction with matter as electrons, but in particular, the scattering behavior is much different. Three important interactions play significant roles in radiotherapy, i.e., inelastic Coulomb scattering with atomic electrons, elastic Coulomb scattering with target's nuclei, and non-elastic nuclear interaction with target's nuclei. The mechanisms and their contributions to particle therapy will be described in the following subsections.

Energy Loss of Heavy Charged Particles

When heavy-charged particles traverse through matter, they constantly lose energy through the Coulomb interactions with the shell electrons and the atomic nuclei, which are technically called "electronic energy loss" and "nuclear energy loss", respectively. As opposed to the light-charged particles, "radiative energy loss" is negligible when it comes to heavy-charged particles because of the inverse proportionality of bremsstrahlung to the square of the particle's mass. At high energies in the therapeutic range (70 – 250 MeV for protons), electronic energy loss completely dominates, while nuclear energy loss practically plays no role but will be influential in very low energy region (< 10 keV/u) which affects only the last few microns of the particle range (Elsässer et al., 2009). The quotient of electronic energy loss (dE) and unit path length (dx) of charged particles or the so-called "stopping power" can be described by the Bethe-Bloch formula (Bethe, 1930; Bloch, 1933). The relativistic version added the shell correction C/Z_T and density correction $\delta/2$ is given by

$$-\frac{dE}{dx} = 4\pi N_A r_e^2 m_e \frac{Z_T}{A_T}\frac{Z_p^2}{\beta^2}\left[\ln\frac{2m_e c^2\gamma^2\beta^2}{I} - \beta^2 - \frac{\delta}{2} - \frac{C}{Z_T}\right] \tag{2.1}$$

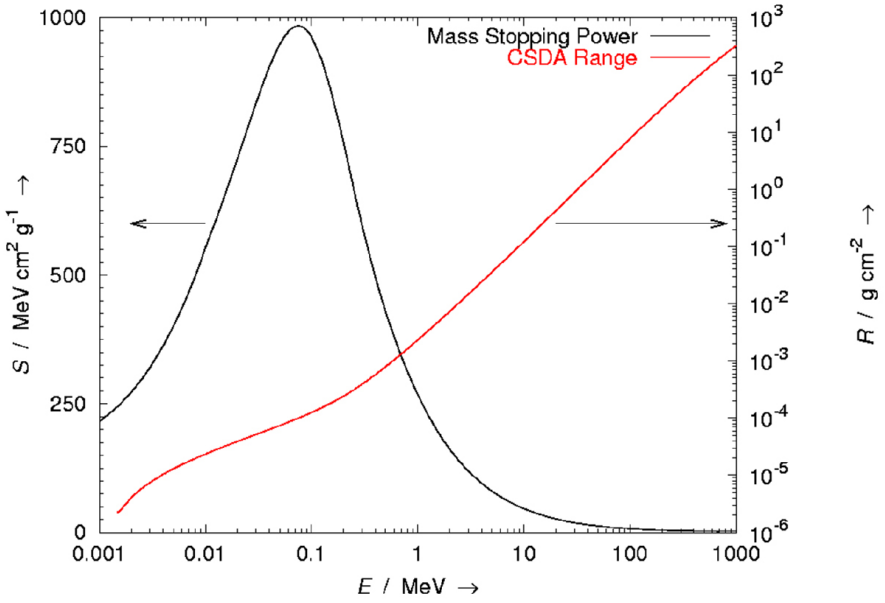

Figure 2.1: The plots of mass stopping power (black line) and CSDA range (red line) against kinetic energy in unit of MeV (Newhauser and Zhang, 2015).

where N_A is the Avogadro constant, r_e is the electron radius, m_e is the electron rest mass, Z_T and A_T are the atomic and mass numbers of the target atom, respectively. Z_p is the atomic number of the projectile, e is the elementary charge, β is the ratio of particle velocity to speed of light c, $\gamma = 1/\sqrt{1-\beta^2}$ and I is the mean ionization energy of the target molecule. Figure 2.1 shows the energy loss rate of a proton as a function of its kinetic energy in the unit of MeV. We can see that the energy loss rate increases sharply with a decrease in the kinetic energy due to the dominant factor β^2 which is inversely proportional to the energy loss function. This explains the large amount of energy deposited in the matter when a charged particle nearly stops moving, resulting in the characteristic peak at the end of the range. This characteristic dose profile of ions was given a specific name called the "Bragg curve" (Bragg and Kleeman, 1904), shown in Figure 2.2. In contrast to photons that the dose distributes almost equally in depth, the precise peak in the ion profile is better in sparing the normal tissue both at proximal and distal parts of the target tumour. This is one of the main advantages of particle therapy, especially for the treatment of deep-seated tumours.

When a highly energetic heavy-charged particle interacts with an atomic electron, it kicks the electron away from its trajectory, thus its charge is still equal to the atomic number charge Z_p. However, if the projectile is slowed down until the energy is lower than 10 MeV/u, the electron capture will cause a reduction of the total

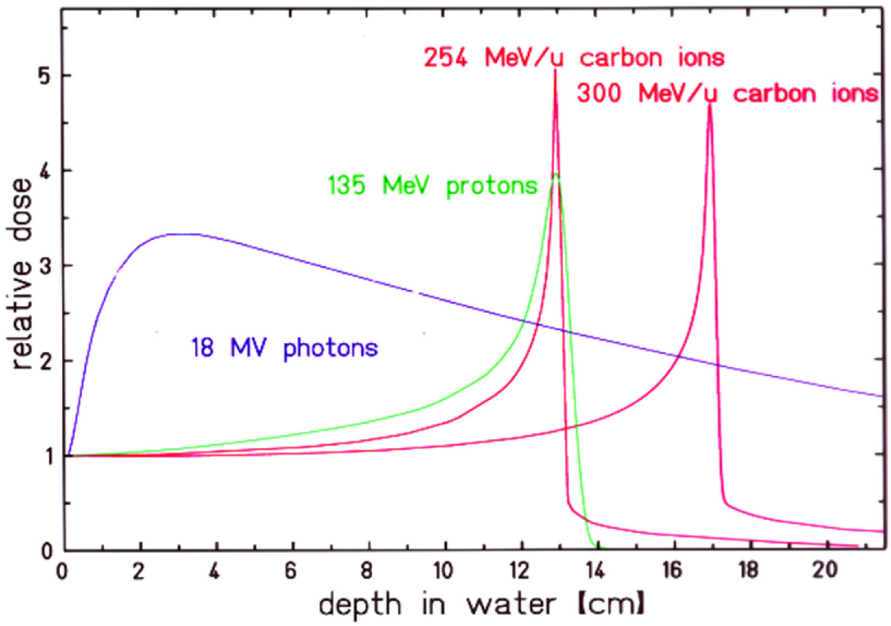

Figure 2.2: Proton (green line) and ^{12}C ion (red lines) Bragg curves compared to a photon depth dose profile (blue line) (Weber and Kraft, 2009).

mean charge of the ion which can be described by the Barkas's formula (Barkas, 1963):

$$Z_{eff} = Z_p \left[1 - \exp(-125\beta Z_p^{-2/3})\right] \tag{2.2}$$

where Z_{eff} is the "effective charge".

Another advantage of the Bragg peak is that its location can be adjusted by changing the kinetic energy of the projectile. That means the peak can be precisely positioned in the tumour region. To determine the range, or the total path length of the particle numerically, one of the simple calculations is the integration of the stopping power over the respective energies which is given by

$$R(E) = \int_0^{E_0} \left(\frac{dE}{dx}\right)^{-1} dE \tag{2.3}$$

where E_0 is the initial kinetic energy. Noted that the calculation is under the assumption that the projectiles only travel forward while losing the energy continuously at the rate of stopping power. That means the statistical fluctuation of the energy loss is neglected. This range is called "Continuous Slowing Down Approximation (CSDA)" range. The plot of the CSDA range as a function of the kinetic energy is also exhibited in Figure 2.1.

As a matter of fact, an individual particle in the beam loses a different amount

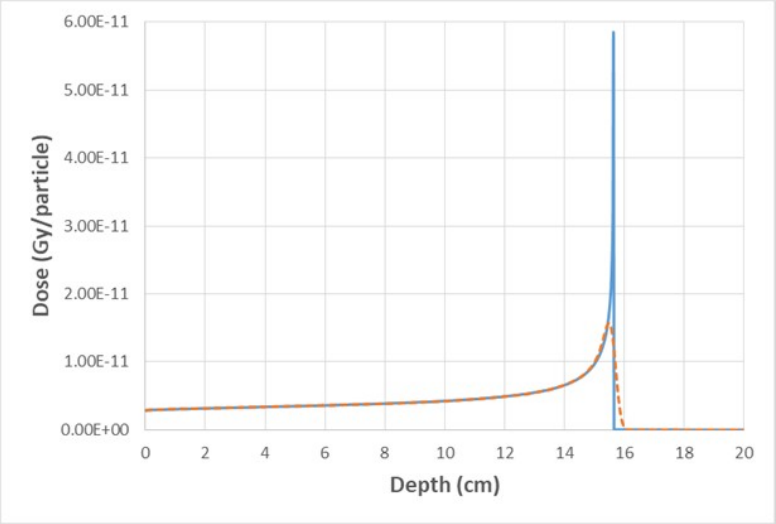

Figure 2.3: The depth dose distributions of a proton with an initial energy of 150 MeV in water without energy straggling (solid line) and with energy loss straggling (dashed line) simulated by PHITS (Niita et al., 2006).

of energy to the absorber. This variation of energy loss is called "energy loss straggling" and the accumulation of the small energy loss straggling along the total trajectory path contributes to the variation of the range or so-called "range straggling". In the case that particles pass through a thin absorber which implies a small number of collisions, the energy-loss distributions are asymmetric and can be described by Vavilov model (Vavilov, 1957). For a thick absorber where a large number of collisions occurs, the distributions converge to the central limit and become Gaussian which are approximated by Bohr's theory (Bohr, 1940; Ahlen, 1980):

$$f(\Delta E) = \frac{1}{\sqrt{2\pi\sigma}}\exp\frac{(\Delta E - \overline{\Delta E})^2}{2\sigma^2} \tag{2.4}$$

with

$$\sigma = 4\pi Z_{eff} Z_T e^4 N \Delta x \left(\frac{1-\beta^2/2}{1-\beta^2}\right) \tag{2.5}$$

where ΔE is the energy loss in a single collision, $\overline{\Delta E}$ is the mean energy loss in the entire absorber of thickness Δx.

The effect of the range straggling is important in defining the shape of the Bragg curve. Figure 2.3 shows that, without range straggling, the Bragg peak is incredibly sharp and has no peak width at all, because every particle stops at the same depth in the absorber. While the Bragg peak influenced by range straggling, is lowered and broadened.

Elastic Scattering

Although the elastic Coulomb scattering with target nuclei is insignificant in the stopping process, on the other hand, it is the dominating process causing lateral beam spreading. Inherently, the angular deflection from a single scattering event is very small, hence the observed beam spread (with a mean deflected angle θ) is the consequence of individual multiple scattering as illustrated in Figure 2.4.

The resulting angular distribution of the beam is approximately Gaussian. The most accurate and comprehensive model for describing multiple scattering was developed by Molière (Moliere, 1948) for which the estimated angular distributions agree very well with experimental data (Gottschalk et al., 1993). Afterwards, Molière's theory was simplified and parameterized by Highland (Highland, 1975, 1979), under the condition of small deflection (particles pass through a thin absorber). The Highland's angular spread θ is calculated accordingly of a Gaussian angular distribution as follows:

$$\sigma_\theta[\text{rad}] = \frac{14.1\,\text{MeV}}{\beta pc} Z_p \sqrt{\frac{d}{L_{rad}}} \left[1 + \frac{1}{9}\log_{10}\left(\frac{d}{L_{rad}}\right)\right] \tag{2.6}$$

where Z_p is the atomic number of the projectile, d is the thickness of the target and the Radiation length L_{rad} is a material-specific constant (Tsai, 1974). The lateral beam enlargement is critical for the pencil beam scanning system (details in section Pencil Beam Scanning) since it can reduce the conformity to the tumour, especially, for the lighter ions (which carry lower mass) like protons. Figure 2.5 shows the broadening of narrow monoenergetic jets of protons and ^{12}C ions, after emerging from the nozzle, traveling in 1 m of air, and water, respectively. It can be seen that protons are stronger scattered, and even stronger at the lower energies due to the dominant term βpc in Equation 2.6. Therefore, in the clinical setup of a proton

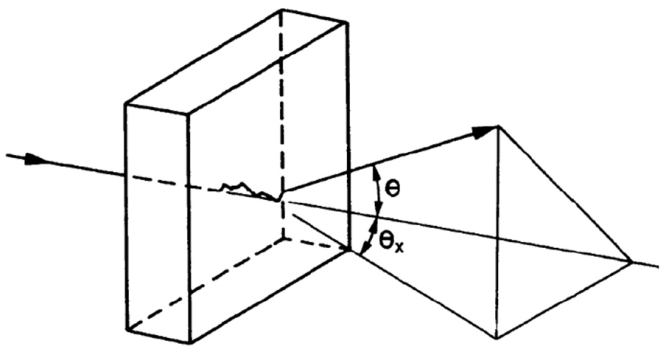

Figure 2.4: Schematic drawing of the multiple scattering effect on a particle traversing in an absorber (Newhauser and Zhang, 2015).

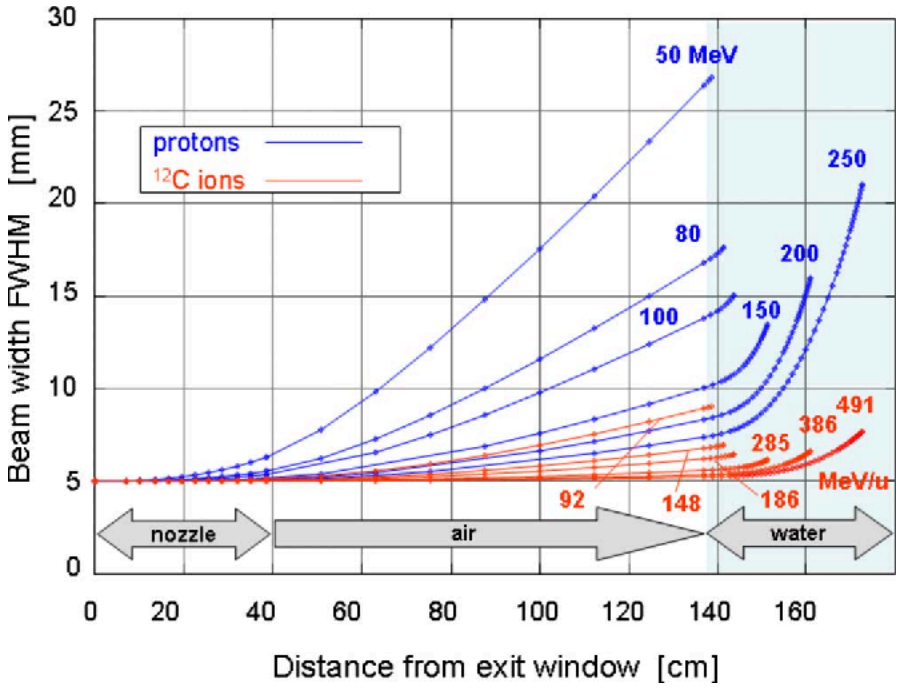

Figure 2.5: Lateral beam spread for protons and ^{12}C ions with an initial beam size of 5 mm FWHM when traversing through the nozzle, 1 m of air, and water, respectively (Schardt et al., 2010).

scanning system, the materials upstream the patient should be as thin as possible and kept as close as possible to the nozzle in order to decrease the scattering effect and keep the highest-possible dose conformity to the target tumour.

Nuclear Reaction

Nuclear reaction with target nuclei is the rarest interactions among the three significant processes for proton therapy. It is not only because of very small volume spaces that the nuclei occupy in the matter, but the incident particles also need to break through the Coulomb barrier to be in the range of the strong force of the nuclei and trigger the nuclear reaction. In the case of proton interaction, the primary proton typically knocks out either a proton or a neutron from the target nucleus and what comes out is the original primary proton which lost some energy (which is then also called a secondary proton by convention) plus another secondary proton or neutron. While the nucleus itself will transform to a lighter isotope or elements with a small amount of kinetic energy, which will then be absorbed locally very close to the colliding point. Because of the very low kinetic energy and higher atomic number of the target fragments, they will deposit high LET (Linear Energy Transfer) energy loss in accordance with Equation 2.1 which is non-negligible in

particle therapy. In the case of nucleus-nucleus collisions such as those between ^{12}C ions and the target nuclei, not only the target fragments but also the projectile fragments can be created. This process can be described by the abrasion-ablation model (Serber, 1947). Since the secondary projectile fragments are still carrying nearly the same energy as the primary projectiles but with a lighter mass, their range could generally exceed the primary range and leave the dose tail, i.e., fragmentation tail, behind the Bragg peak which can be spotted in Figure 2.2.

The other significant product is the neutron concerning radiation safety issues. The neutron-induced radiation hazards need to be considered both in patients and surrounding environments as neutrons have high penetrating power and their biological effectiveness could be 20 times higher than protons (Valentin, 2008). Likewise, the neutron production in the beamline upstream the patient also needs to be taken into account and should be minimized if possible.

2.2 Beam Delivery System

Although the Bragg curve's sharp-peaked characteristic is generally favorable for radiotherapy, such a narrow peak is still not clinically applicable because the width is typically much smaller than the whole target size. Therefore, the primary goal of particle therapy is to send the maximum dose in the planning, covering the entire target volume, both in transversal and longitudinal directions. This can be achieved by the proper beam delivery techniques which the two basic ones, passive beam application and active pencil beam scanning, will be explained in this section, as well as the discussion of their pros and cons.

Passive Beam Application

Passive beam application was the most commonly used in the past (but is replaced now more and by the scanning method). The main concept of this method is to use passive scatterers and energy modulators to spread the narrow monoenergetic beam of particles, initially delivered from the accelerator, to become a homogeneous tumour coverage. The systems of beam spreading and shaping devices are placed on the beam path in front of the patient. A simple schematic representation of the passive scattering system is illustrated in Figure 2.6 where the beams are sent from

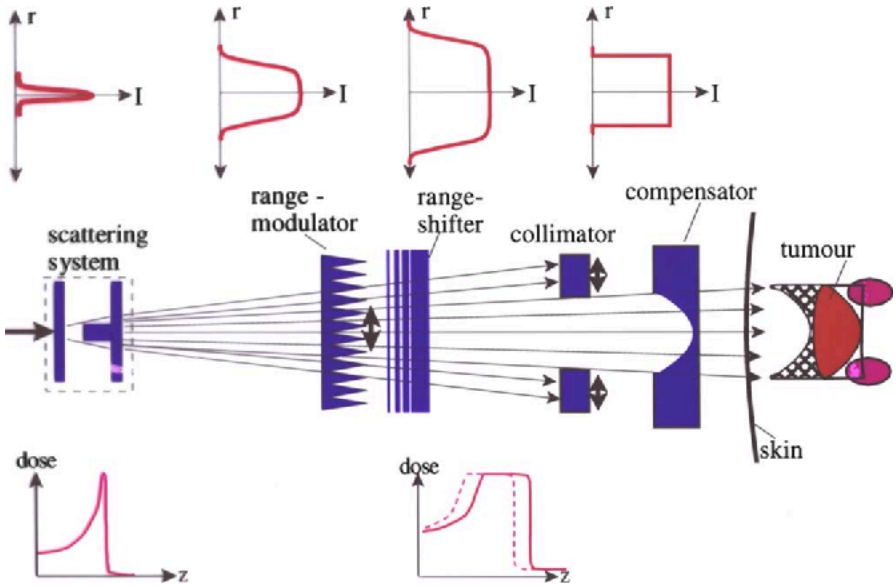

Figure 2.6: Schematic drawing illustrating fully passive beam scattering and modulating systems (Schardt et al., 2010).

the left-hand side and pass through the scattering system, the range modulator, the range shifter, the collimator, the compensator and reach the patient at the end.

Scattering System: Collimator and Bolus

In the first step, a delta function-shaped beam is transformed to a flat-topped transversal profile mostly by a "double-scattering system" (Koehler et al., 1977). Then, the beam field continues to broaden naturally as it translates in space and by multiple scattering with air molecules and other materials in the beam path. To protect the surrounding normal tissues from undesired radiation, the field out of the lateral tumour area is blocked by a high atomic material, e.g., brass, whose shape is manufactured precisely to match the largest tumour target cross-section. This patient-specific hardware is called a "collimator". Another important device serving for achieving the dose conformation to the target volume is a "compensator" or "bolus". The device is typically fabricated from a tissue-equivalent material (both equivalent in stopping and scattering power) which is used to compensate for the tissue inhomogeneities in front of the target as well as the curvature of the patient surface (Akanuma et al., 1982). By the analyzation of patient anatomy from the CT (Computed Tomography) scan data, the bolus structure can be designed and customized to adapt the beam range to the distal contour of the specific-patient tumour (Goitein, 1978). The examples of these patient-specific apertures are shown in Figure 2.7.

Figure 2.7: Examples of patient-specific apertures: a collimator (left) and a compensator (right) (Klyachko, 2017).

Energy Modulator: Ridge Filter

Secondly, the monoenergetic particle beam is modulated by an energy modulator which can be either a rotating wheel with different thicknesses ("modulation wheel") or a plate with periodically arranged wedge-shaped structures ("ridge filter" (Figure 2.8)). By passing the beam through the absorber with the various thicknesses of n steps, the predefined depth dose profile can be distributed into n number of Bragg curves of different ranges spreading over the longitudinal target dimension. Importantly, each Bragg curve must be weighted to form an equal dose peak, or known as "Spread-Out Bragg Peak (SOBP)" (Figure 2.9) at the target region. The resulting dose D at the position z_i which locates in the SOBP can be calculated by

$$D(z_i) = \sum_{j=1}^{n} w_j b_j(z_i) \tag{2.7}$$

w_j is the weighting factor for an individual Bragg curve b_j, which can be calculated from the minimization of the difference between the calculated dose D and the prescribed dose at the tumour. In order to manufacture the modulator, the weighting factors are converted to the areal fractions of the material thickness which then define the shape of the modulator. As you can see in Figure 2.8 (b) that shows the single structure of the ridge filter, the step width for each thickness is varied according to the weighting factors.

Additionally, the location of the SOBP can also be adapted by a series of homogeneous absorber plates of different thicknesses, or a so-called "range shifter".

Passive beam application has some major disadvantages. First, the dose distri-

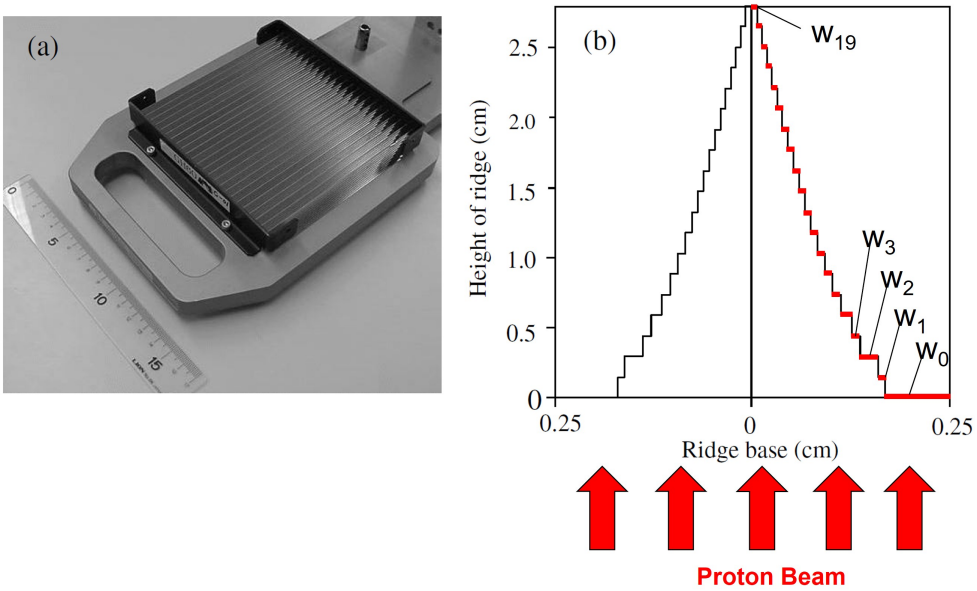

Figure 2.8: (a) An example of ridge filters for the proton beam and (b) the cross-sectional shape of the single ridge (Akagi et al., 2003).

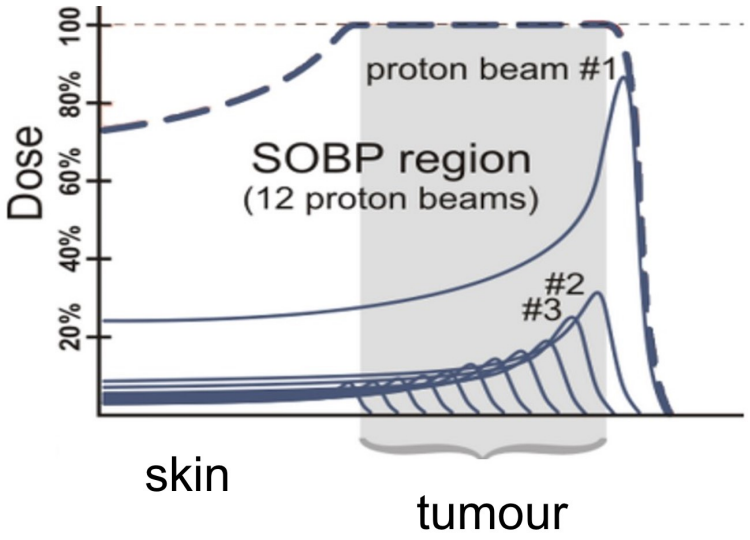

Figure 2.9: A visualization of a SOBP as a superposition of weighted Bragg curves of different ranges (Yokoi et al., 2008).

bution can only be adapted to the distal edge of the tumour, but not to the proximal one because of the fixed-SOBP width. Therefore, significant high doses are unavoidably absorbed in the healthy tissue in front of the target which is represented as the grid contour in Figure 2.6. Another disadvantage is that there are a lot of materials required in the beam path. This hugely reduces the beam intensity before reaching the patient. Moreover, it increases the nuclear reaction followed by higher production of unwanted secondary neutrons.

Pencil Beam Scanning

The more modern method is the pencil-beam scanning technique (Haberer et al., 1993; Pedroni et al., 1995). It is called a pencil beam because the beam is tiny as it is focused on an area of a few millimeters by strong magnets. The scanning plan is proceeded by dividing the arbitrary target volume into slices or layers of equal particle energies. Each energy layer is also dissected into a pattern of "scan spots" and the pencil beam will be scanned spot by spot along the continuous path until it covers the whole energy layer. The exact number of particles in each scan spot is calculated by the treatment planning system and the two magnetic dipoles are used to move the pencil beam in a predetermined way (Figure 2.10). The dose distribution at depth (the SOBP length) is determined by a gradual energy variation in the synchrotron or by changing the configuration of the degrader in cyclotron-based systems. Noted that the distance between the two closest energy layers has to be very small, i.e., smaller than the half-width of the Bragg peak maximum (Kraft, 2000), for avoiding the dose ripple at the SOBP. Thus, a large number of energy layers is required especially for ions with a sharp Bragg peak like ^{12}C ions to create a smooth SOBP.

The pencil beam scanning method enables a highly compliant dose adjustment to both the distal and also to the proximal edge of the tumour, which in turn offers better conformity of radiation dose. However, the total irradiation time is relatively long because the machine needs several seconds to switch the energy layer. Thus, for the treatment planning with a large number of energy layers requirement, the accumulated energy switching time could be extended to several minutes. This is a major disadvantage of a fully active scanning procedure, especially for the treatment of moving tumours (e.g. in the lungs or livers). The raster scan method leads to "interplay effects", i.e. interference pattern between the deflection of the beam and the tumour movement resulting in under- and over-dosing in both the tumour and in

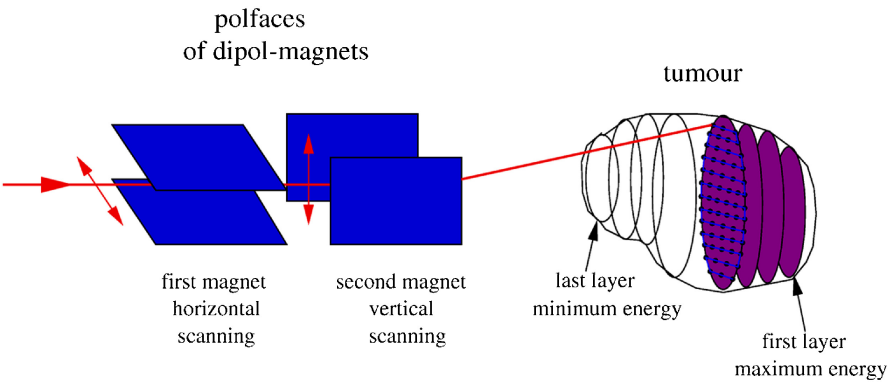

Figure 2.10: Schematic drawing illustrating fully active beam scanning procedure (Schardt et al., 2010).

healthy tissue (Bert et al., 2008; Lambert et al., 2005).

Ripple Filter (RiFi)

One method added to reduce the number of the energy layer is the application of a stationary device called a "Ripple Filter (RiFi)" (Weber and Kraft, 1999). It is a kind of mini ridge filter made of plastic material, that was developed to smoothen the ripple of the SOBP by broadening the narrow-single Bragg peaks to Gaussian peaks. For instance, a tumour with a width of 2 to 5 cm would require over 50 steps of energy of ^{12}C ions, but with an application of RiFi, only 16 energy layers are adequate to form a smooth SOBP as shown in Figure 2.11. As a result, the total irradiation time is significantly reduced. This device is extremely beneficial for the clinical use of the heavy ion beam like ^{12}C ions which has a very sharp Bragg peak but is not so necessary for the application of proton beam which usually has a broader peak.

The two types of RiFis are shown in Figure 2.12. An "1D Ripple Filter (1DRiFi)" is the first version of RiFi with 1D groove structure. The other is a newer version, i.e., "2D Ripple Filter (2DRiFi)" (Ringbæk et al., 2018). With the 2D-grooved and the cone-shaped designs, the base layer could be cut out in order to reduce the unnecessary scattering effect.

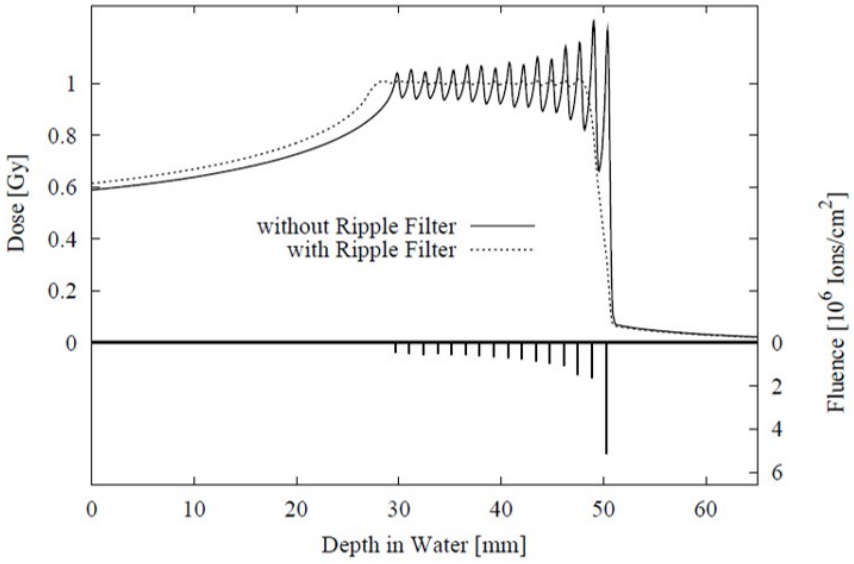

Figure 2.11: SOBPs of 16 individual ^{12}C Bragg curves with (dotted line) and without (solid line) use of the RiFi. The lower part shows the fluences of superposing Bragg curves at the individual peak position (Weber and Kraft, 1999).

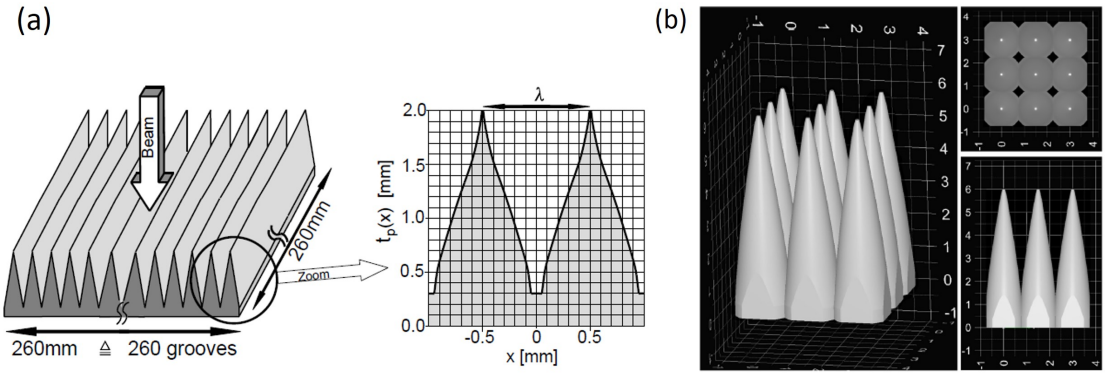

Figure 2.12: (a) General structure of the 1DRiFis with the cross-sectional shape of the groove Weber and Kraft (1999) and (b) a section of the 2DRiFi seen from side views and top view Ringbæk et al. (2018).

2.3 3D-Printed Modulator

To minimize some of the disadvantages of passive beam application and pencil beam scanning, the concept of the so-called "3D-Printed Modulator (3D-PM)" was developed. The devices are fabricated from simulated polypropylene, which has radiation properties like Plexiglass (PMMA). The chosen choice for the manufacturing process is the 3D polymer printing technique because it enables complex shapes with very high resolution. Moreover, it is also faster and cheaper compared to the other manufacturing methods, e.g., the CNC method. A number of studies in the field have proven the concept of 3D printing used for proton therapy (Lindsay et al., 2015, 2016).

3D Range-Modulator

The "3D Range-Modulator (3DRM)" (Simeonov et al., 2017, 2022) is a combination of a compensator and a very fine ridge filter. Figure 2.13 shows the prototype of the 3DRM that was designed specifically for a spherical target. The homogeneous base was adapted according to the distal end of the target serving the same purpose as a compensator. Unlike the ridge filters that create the fixed width of SOBP, the pyramid-shaped structures (ridge filter-liked structures) of the 3DRMs or "pins" have different heights which are carefully designed to create the SOBPs corresponding to the laterally variable thicknesses of the tumour. So, the final shape of the filters conforms to the proximal contour in contrast to classical passive scattering.

The 3DRMs are optimized to be irradiated with a single energy layer of the pencil beam scanning procedure. Therefore, it generates a highly conformal radiation field that is comparable to the fully active pencil beam scanning. Moreover, the irradiation of complex-shaped tumours is also possible since the dose is adapted not only to the distal but also to the proximal edge of the tumour. Figure 2.14 shows the highly conformal and homogeneous dose in the spherical target volume which can be achieved by the irradiation of mono-energetic ^{12}C ions with the application of the 3DRM. Moreover, the use of just one energy layer significantly reduces the total irradiation time ($\ll$ 1 s), allowing for reliable irradiation of mobile tumours.

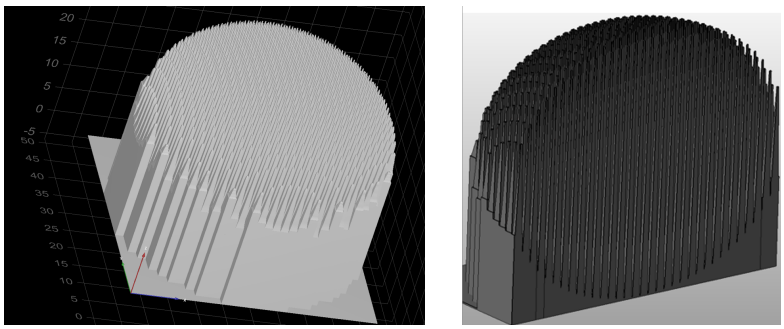

Figure 2.13: Graphical image of the 3DRM designed for a spherical target with a diameter of 5 cm (left) and its half section (right) seen from oblique views. Figure courtesy from Dr. Uli Weber, GSI, Germany.

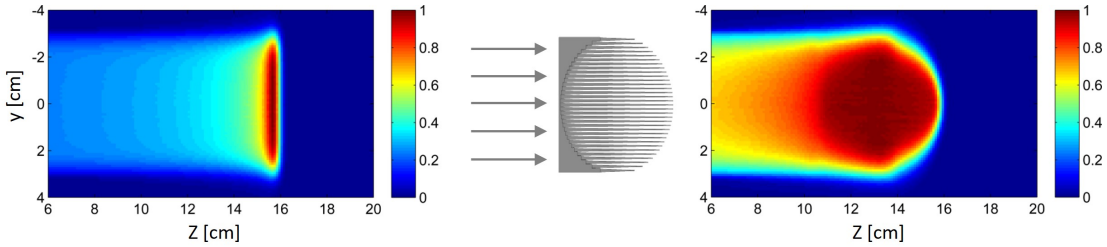

Figure 2.14: Concept of 3DRMs optimized for a spherical target with a diameter of 5 cm. 2D dose distribution in water simulated by FLUKA. Figure courtesy from Dr. Uli Weber, GSI, Germany.

2D Range-Modulator

Another type of 3D-PMs is a ”2D Range-Modulator (2DRM)” (Simeonov et al., 2021). It is a simplified version of the 3DRMs that consists of an arrangement of equal-height and identical-shaped pins which are held together by a base layer. Thus, the delivered maximum dose is not designed to conform to a specific patient tumour but to create a SOBP with one fixed width in the phantom. Rather than being used in clinics for treating patients, the 2DRMs are more likely designed for research purposes, which require a SOBP with a certain width. For instance, they have been used for radiobiological research (Tommasino et al., 2019), the determination of the beam quality correction factor for a Farmer-type ionization chamber (Holm et al., 2020), PET imaging studies (dos Santos Augusto, 2018) etc. Moreover, the constant lateral dose distribution provided by the 2DRM is also useful for detecting the dose deviation caused by the manufacturing artifacts, which is an important process for improving the precision of the 3D-PMs manufacturing.

Since the pin’s height could be one of the factors that affect the inhomogeneity induced behind the modulator, the 2DRM with an equal pin height provides an

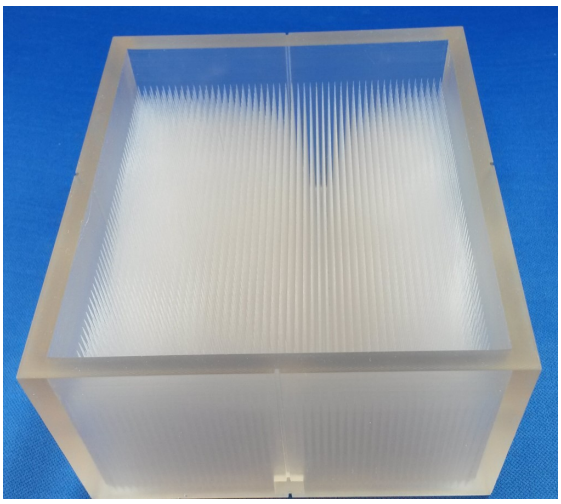

Figure 2.15: An example of 2DRM which was optimized for 150 MeV proton beams to create a 5 cm SOBP in phantom. The height of the pin is about 45 mm and the pin's base area is 2×2 mm^2

advantage for better systematics investigation. Therefore, the 2DRM was also used in this work as a kind of well-defined special case of a 3DRM.

2.4 Edge Scattering Effect and Inhomogeneity in the Near Field of 3D-Printed Modulator

One phenomenon that plays a significant part in the thesis is the "edge scattering effect". The edge scattering effect is caused by inhomogeneous scattering when the particles pass through a strong perpendicular gradient of mass density with respect to the beam axis, in another word, an "edge" of a high-density material like steel in the example of Figure 2.16. It can be seen that the particles scatter off the steel and superpose with the forwardly traveling particles in water (the lower scattering area), resulting in an increase in the particle fluence and, meanwhile, a decrease in fluence behind the steel (the stronger scattering area). The strength of such a fluence inhomogeneity depends on the scattering effect which already discussed in section 2.1 regarding elastic scattering. Besides, the orientation and thickness of the material also affect the strength of the inhomogeneity. The thicker and heavier the material is, the stronger the inhomogeneity. These were studied thoroughly by the research of the dose perturbation induced by fiducial markers (Newhauser et al., 2007; Cheung et al., 2010; Reidel et al., 2022).

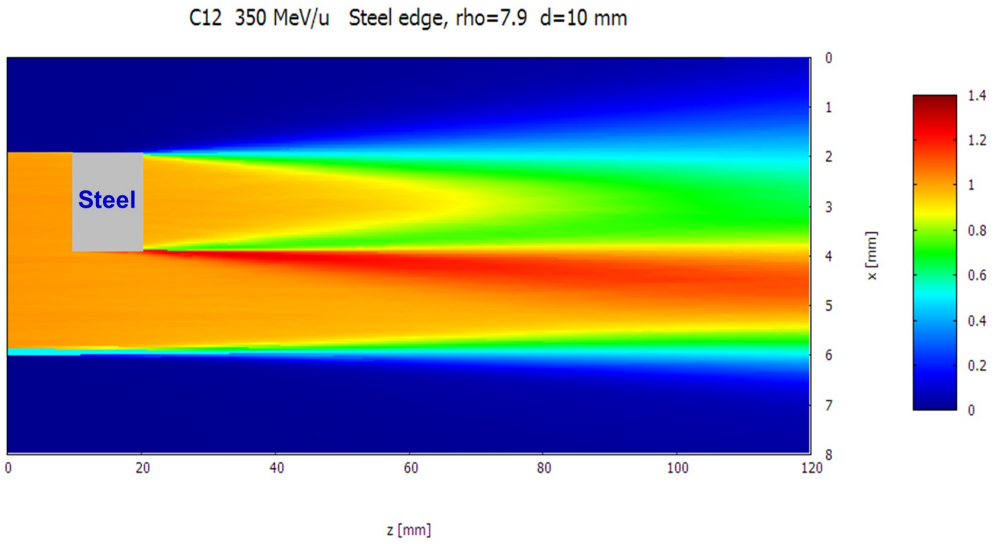

Figure 2.16: The dose distribution of the homogeneous ^{12}C ions beam in water with a steel block in the beam path calculated by a Monte Carlo Programm MC@TRiP (Iancu et al., 2015). Figure courtesy from Dr. Uli Weber, GSI, Germany.

Edge scattering also plays an important role in the clinical implementation of periodic-structured devices like RiFis and 3D-PMs. Figure 2.17 shows the strong fluence inhomogeneity which can be spotted behind the RiFi. Because of the periodic structure of the RiFi, the superposition of the scattering particles results in fluence oscillation in the near field region. In the far-field region, the fluence oscillation will be blurred out because of the overlapping contributions from the single edge scattering. For this reason, the RiFis are always placed far away in order to avoid the inhomogeneous dose in the patient's body. The study on dose inhomogeneity caused by RiFi can be found in (Ringbæk et al., 2014).

Additionally, the edge scattering and overlapping effect are the main contributors to the homogeneous dose in the SOBP when the RiFis are applied far from the target. If the particles only keep going straight without a scattering effect, the RiFi's groove pattern will be transferred to the target volume because of the different thicknesses of the absorber. Fortunately, this cannot happen in reality because the groove pattern is washed out by the blurring effect resulting from the edge scattering and multiple scattering. Hereby, the dose distribution is safe from the groove pattern.

Similarly, fluence inhomogeneity is observed behind the 3D-PMs, and is even stronger than the one induced by the RiFis due to the larger thickness of the 3D-PMs. In 2017, (Simeonov et al., 2017) reported the appearance of the fluence grid

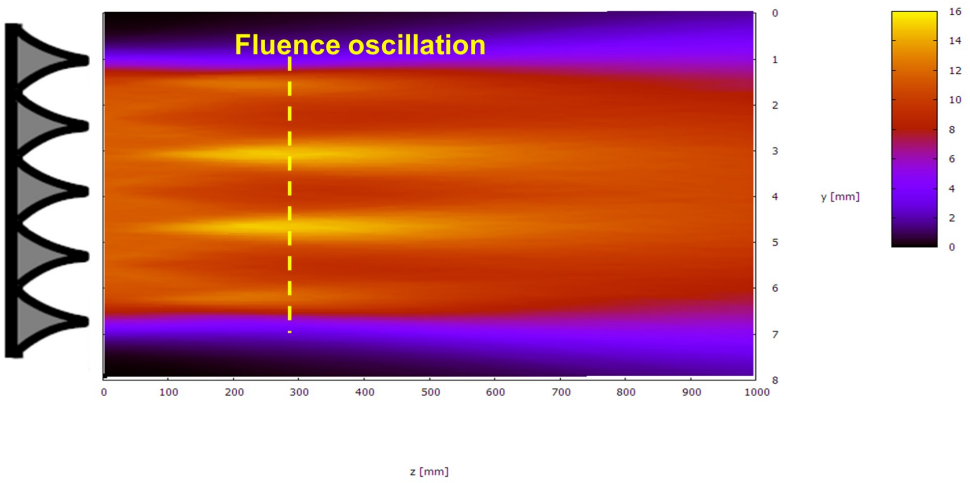

Figure 2.17: The simulated 2D fluence distribution (in xz-plane) in the air behind the RiFi. Figure courtesy from Dr. Uli Weber, GSI, Germany.

pattern at the small distances behind the first prototype of the 3DRM as shown in Figure 2.18. Thus, the 3D-PMs are usually placed far away from the patients in the same manner as the RiFis. However, placing the modulator too far from the patient will reduce the dose conformation to the target due to the enlargement of the beam (as described in section 2.1 regarding Elastic Scattering). For the best treatment efficiency, the 3D-PMs should be as close as possible to the target and the field also needs to be free from the interference of the field inhomogeneity. Leading to the first objective of the thesis, the minimum distance, where the fluence inhomogeneity starts to completely fade away will be determined.

Even though the reproducibility of the fluence grid pattern behind the 3D-PMs has been proved constantly, systematic investigation and evaluation have never been done before. Hereby, the sensitivity of the inhomogeneity induced behind the 2DRMs will be tested by various possible parameters. The procedure will be elaborated on further in Chapter III.

2.5 FLASH Therapy

The relevant research indicates that a high dose rate delivered (> 40 Gy/s) within an extremely short irradiation time (in milliseconds) might be able to trigger the radio-resistance in normal cells while maintaining tumour control as efficient as the conventional dose rate, resulting in the enhancement of the therapeutic index. This

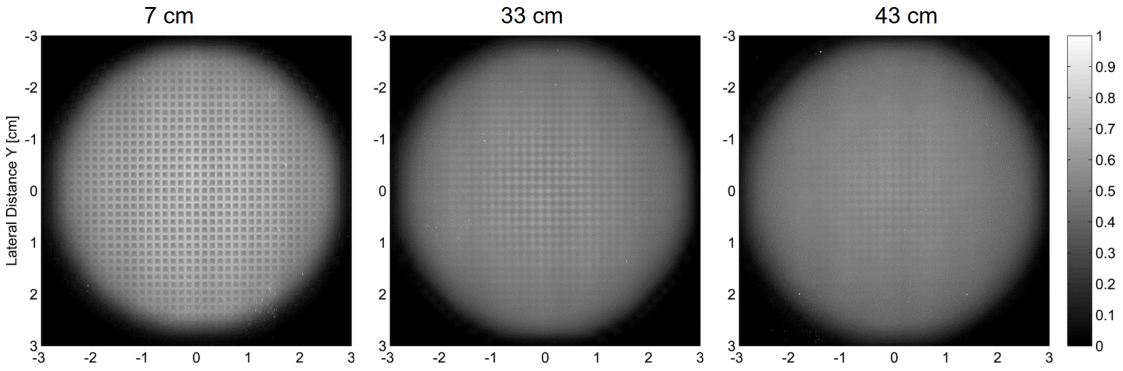

Figure 2.18: The fluence grid pattern spotted at the different distances behind the 3DRM (Simeonov et al., 2017).

astonishing beam delivery technique is called “FLASH irradiation”. Even though it is well-known for its incredible tissue sparing, the explanation for the FLASH mechanisms is still unclear. One of the most convincing hypotheses is the oxygen depletion inducing temporary-hypoxia state in normal tissue (Wilson et al., 2012). The first stimulus of the growing interest in FLASH effect was the evidence from the irradiation of electron FLASH beam, which indicated the reduction of early and late radiation-induced complications in normal tissue of small animals (Favaudon et al., 2014; Vozenin et al., 2019). Afterward, multiple experiments were conducted constantly and confirmed the reproducible FLASH effect, and the successful treatment of the first human was reported in 2019 (Bourhis et al., 2019). Not only electrons and x-ray but the spectrum has also been broadened to different types of radiation such as protons and heavy ions, which offer a large target-to-entrance dose ratio to improve the sparing of healthy tissue when combined with FLASH irradiation (Van De Water et al., 2019). However, producing a sufficient ultra-high dose rate to enable FLASH is not too straightforward due to the limitations of the current accelerator technology and beam delivery systems, thus becoming one of the challenges of FLASH clinical transfer. Even though some commercial cyclotrons can provide sufficient beam current (roughly 300 nA) for FLASH, the FLASH dose rate is impossible to achieve by performing conventional beam delivery techniques: the conventional passive scattering technique cannot reach the FLASH dose rate because of the beam loss from the scattering devices, while active scanning is stressed by the energy layer switching time.

One of the most promising methods to enable FLASH for particle therapy mentioned in different articles is the application of 3D-PMs (Jolly et al., 2020; Weber et al., 2022). Because of the capability to create a highly conformal dose dis-

tribution within a very short irradiation time (0.1 s), 3D-PMs, specifically 2DRMs have been applied in the FLASH research and already performed in animal experiments successfully (Tinganelli et al., 2022a,b).

2.6 Minibeam Particle Therapy

Another novel dose delivery concept that dedicates to improving the sparing of normal tissue is "spatially-fractionated proton minibeams" (Meyer et al., 2019). The principle is to irradiate the micro- or submillimeter-sized beams onto the patient's skin in the arrangement of grid or dot patterns as shown in Figure 2.19, with a center-to-center (ctc) distance of a few millimeters. In this way, large parts of the normal tissues in front of the tumour can be reserved from radiation toxicity. The peaks-valleys dose profile of minibeams is usually characterized by a "Peak-to-Valley Dose Ratio (PVDR)", which is desired to be as high as possible at the entrance channel for efficient minibeam therapy. Even if there are high cell death rates at the peaks, normal tissues can tolerate high doses without any significant late damage because a minibeam size is tiny. Thus, the recovery of the entire tissue can be enhanced by the migration of the spared healthy cells from the large unirradiated regions to the small-damaged region. This hypothesis that explains the correlation between the volume size of the irradiated tissue and the dose tolerance of normal tissue is known as the "dose-volume effect" (Hopewell and Trott, 2000).

Even though the inhomogeneous dose is presented on the skin of the patient, the homogeneous dose in the target volume still can be achieved by the well-defined treatment planning exploiting multiple Coulomb scattering that enlarges and merges the beams together at the SOBPs Figure 2.20. Therefore, the dose coverage of the target can still comply with standard dose criteria as conventional homogeneous

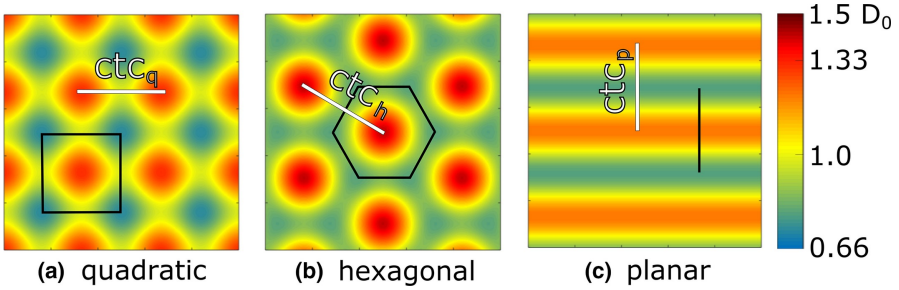

Figure 2.19: Examples of minibeam arrangement: (a) quadratic and (b) hexagonal pencil minibeam and (c) planar minibeam arrangements (Sammer et al., 2017)

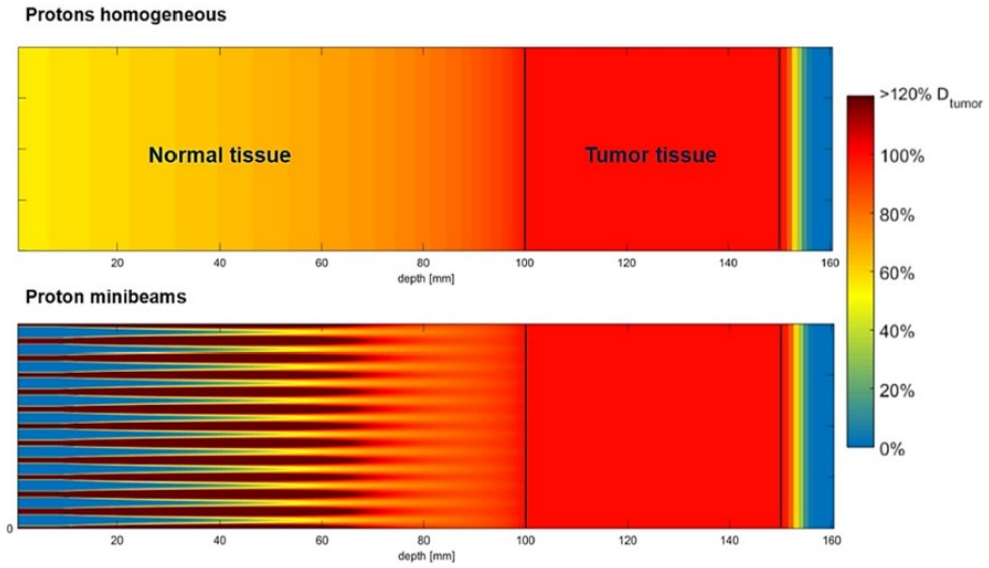

Figure 2.20: Simulated dose distributions with SOBPs for (a) homogeneous beam field (top) and fractionated beam (bottom) (Meyer et al., 2019).

dose application.

If we look back to the grid pattern produced by the 3D-PMs, we will see the dose is also spatially fractionated in a similar manner to minibeams.This gave us a question: whether this kind of fractionated beam induced by the 3D-PMs can trigger the sparing tissue effect as the minibeams do? Therefore, the dose distribution at the near field region behind the 3D-PMs will be investigated in this work as well.

2.7 Monte Carlo Simulation

The Monte Carlo method is a way of solving a deterministic problem that is time-consuming or even impossible to solve analytically (a problem with too many coupled degrees of freedom), by a stochastic approach using random numbers. The idea is to sample the value repeatedly from a given set of probability distributions until reaching a sufficiently large number of contributions. The distributions will become Gaussian which converges to the “expectation value” according to the “Central Limit Theorem”.

Particle Transport Equation

The main task of the particle transport problem is to solve Boltzmann's equation, which explains the particle propagation in space by the evolution of the probability density function given by

$$f_{det}(r,p,\alpha) = \iiint G(r,p,\alpha : r',p',\alpha') f_{src}(r',p',\alpha')\, d^3r'\, d^3p'\, d^n\alpha' \tag{2.8}$$

where r is the particle coordinates, p is the particle momentum, and α is additional variables, e.g., particle species, spin. The concept of source (where particles in an initial state of (r', p', α')) and detector (where particles in a final state of (r, p, α)) is presented. The evolution between the 2 states is defined by the propagator operator G which accounted for all the microscopic processes, e.g., geometry boundary conditions, scattering, particle production, particle absorption, and external forces. To find such multiple integral solutions, the Monte Carlo method is one possible way to solve utilizing the stochastic nature of radiation interaction. The concept is to generate the particles from pseudo-random seeds and follow them on their path through the matter. The event and outcome are selected randomly from the probability distributions in the form of interaction cross sections. After that the generated secondaries will be stored in a "bank" and will be sent to the next state. Then, the process repeats the same for a new history. The more histories (N) there are, the more accurate the result ($\sigma \propto 1/\sqrt{N}$).

The accuracy and reliability of a Monte Carlo code depend on the models or data on which the probability distribution functions are based. If it is embedded by reliable cross sections and physics models, the Monte Carlo solution can agree well with measurements with very high accuracy (Battistoni et al., 2016). For this reason, the Monte Carlo particle transport code is considered to be a "gold standard" for particle therapy, e.g., for creating data bases of treatment planning systems (Battistoni et al., 2016). In this work, the fully-integrated Monte Carlo particle transport code FLUKA (Böhlen et al., 2014) was used. The physics setting will be distributed in Chapter III.

Chapter III

MATERIAL AND METHODS

The methodology of this thesis will be divided into 4 sections, i.e., 2DRM implementation in FLUKA, generic test of near field inhomogeneity, comparison with the film measurement, and near field simulation for the clinical setup. The introduction of the Monte Carlo particle transport simulation program FLUKA as the main tool for this thesis and the physics setting for the simulations will be mentioned in the first section.

3.1 Physics Settings in FLUKA

The main tool of this thesis is the Monte Carlo particle transport code FLUKA (FLUktuierende KAskade) (Ferrari et al., 2005; Böhlen et al., 2014). It is a multi-purpose simulation package for high energy physics that can be applied to a broad range spectrum in the field, e.g., high energy physics experiment and engineering, radiation protection, detector simulation, and also hadron therapy. The program was co-developed by the European Laboratory for Particle Physics (CERN) and the Italian Institute for Nuclear Physics (INFN) in 1989 and has become one of the main Monte Carlo programs for particle therapy in Europe (Battistoni et al., 2016) because of its reliable underlying physics model and reproducible simulation. In the energy range relevant for proton therapy, the FLUKA physics models are well developed and benchmarked and therefore allow a dose calculation accuracy on the percent level (Baumann et al., 2019).

Unlike other Monte Carlo simulation code, FLUKA is a fully-integrated physics package that satisfies the goal of being user-friendly while providing the high accuracy of the modern hadronic model. Thus, the physics model cannot be changed by the user but the accuracy can be optimized by changing some physics parameters.

In this work, FLUKA version 2020.0.10 was used. The "HADROTHErapy" option was set as a physics default mode as recommended for hadron therapy calculation. By selecting this default, the particle transport threshold was set to 300 keV

for every particle except photon transport which the cutoff was set to 100 keV, and neutron which the energy can be lowered to thermal energies (cutoff energy is 10^{-5} eV and high energy threshold is 20 keV). The delta ray production threshold for this mode was 300 keV. To maximize the accuracy of hadronic simulation, the FLUKA libraries, i.e., DPMjet and RQMD were linked with the "flukadpm" executable.

Since the water target will be applied for the dose scoring implementation, the mean excitation energy of water was set to 78 eV, following the recent studies (Kumazaki et al., 2007; Paul, 2007; Schardt et al., 2007).

3.2 2D Range-Modulator Implementation in FLUKA

The biggest challenge in this work is implementing the complex geometry of the 2DRM in the simulation program. Implemented by the standard FLUKA Combinatorial Geometry is impossible to realize the realistic shape of the filters because uncountable boundaries would be required to form the specifically designed curves of the pins. Fortunately, FLUKA provides alternative functions through the user routine which the users can customize the problem by writing FORTRAN 77 scripts. The user routine dedicated to creating specified material geometries is called "USRMED.f". The calculation method inserted into this routine will be described thoroughly in this section.

Pin Shape Data

In section 2.2 regarding the energy modulator, we explained the general concept for designing the single structure of the modulators, i.e., the ridge filter, in the form of weighting factors w_j corresponding to the absorber thicknesses. The same goes for the optimization of the 3D-PM's pins. Each thickness is scaled by the water equivalent relative stopping power of the manufacturing material to achieve the desired SOBP depth in water, and the squared-areal fractions from the beam-eyed view are scaled by the weighting factors. An example of the optimization product is exhibited in Figure 3.1 (a) and the later smoothened pin with a base layer is shown in Figure 3.1 (b). The groove area scaled by w_0 is always the biggest because the SOBP always needs the largest contribution from the deepest Bragg peak. The groove can be

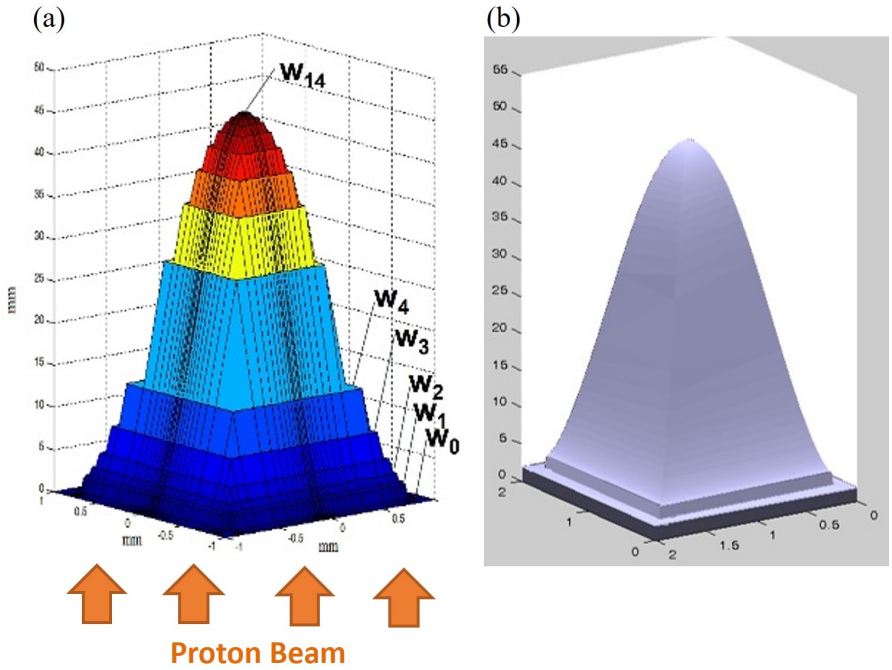

Figure 3.1: (a) The pin shape characterized by weighting factors for different thicknesses and (b) the later smoothened pin with a base layer.

even wider by cutting out the first few steps from the bottom if one desires a sharper distal edge of the SOBP (Simeonov et al., 2017). The same idea for boosting the proximal edge, the highest few step thicknesses could be cut out to widen the pin tip resulting in a flat pin tip (Simeonov et al., 2021).

In the past, as mentioned in (Simeonov et al., 2017), the pin shape was triangulated and saved in an STL (Standard Tessellation Language) file format. In this work, we saved the pin's data as a set of interpolation points with the pin height as a function of the pin radius. One of the pin data of the 2DRMs used in this thesis is presented in Figure 3.2. The base area was scaled to be 1 mm^2 for the purpose of allowing users to adjust the base size of one single pin by simply multiplying the radius by half of "pin period". Only necessary data for shaping the pin was saved in the file to minimize the file size. The others which align in a straight gradient were excluded because they can be interpolated during the calculation in the user routine. This data file is also used as an input file in which the users can define the type of the filters (2DRM, 3DRM, 1DRiFi, and 2DRiFi), the pin period, the maximum thickness of the filter, and the thickness of the base layer.

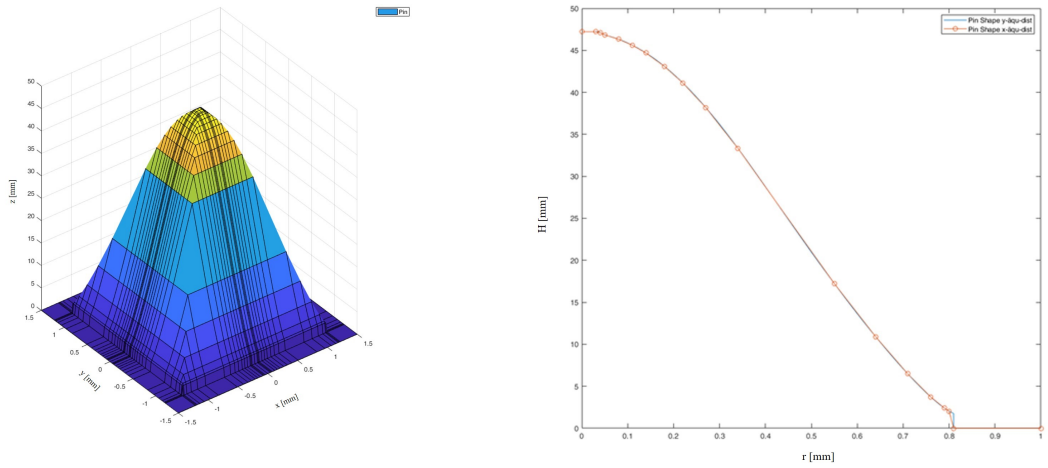

Figure 3.2: The pin shape data (as interpolation points) in the form of pin's heights with the corresponding radius.

USRMED.f Routine

As mentioned before, the USRMED.f routine was customized and written in FORTRAN77 to implement the complex geometries which are difficult or impossible to construct in FLUKA standard input. The concept of the routine is similar to the one described in (Simeonov et al., 2017). To call the USRMED.f via the "MAT-PROP card", a homogeneous "substitute" plate with the same material as the modulator was added to the FLUKA standard input. Importantly, the thickness of the substitute plate needs to be equal to the maximum height of the actual modulator. Then, every time a particle hits this plate, the USRMED.f routine will be activated and shifts the particle along its directional vector (v_x, v_y, v_z), from its initial position, (x, y, z) for the example in Figure 3.3 (a), until reaching the modulator. After that, the final coordinates (x', y', z') will be sent back to FLUKA and the absolute authority will be returned to FLUKA executable again.

Before shifting the particle, one has to calculate the distance that the particle will travel in the modulator (D_{mod}) by using the input data of the pin's profile. The intersection calculation method will be described in the next subsection. After the calculation of the D_{mod}, the distance of the particle shifting D_{shift} was calculated by the subtraction of the D_{mod} from the total distance D that the particle passes through the substitute plate. Then, the particle would be translated along its directional vector with the distance of D_{shift}.

Figure 3.3 (b) shows an example of a color wash map of the proton fluence

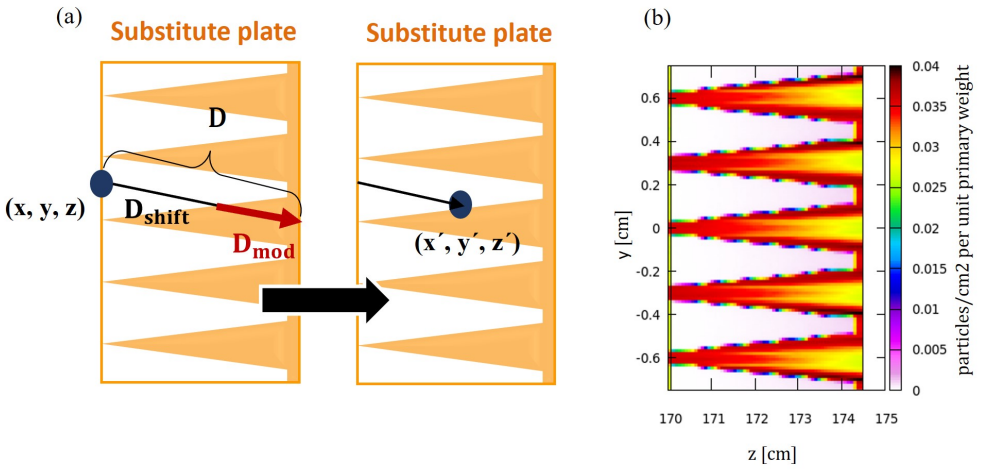

Figure 3.3: (a) The demonstration of the particle shifting through the substitute plate to realize the shape of the 2DRM and (b) the 2D fluence color plot at the substitute plate when using the USRMED.f routine.

zoomed to the substitute plate which shows the realization of the shape of the 2DRM by using the USRMED.f routine. The white spaces indicate the absence of the particles since they were shifted directly to the modulator by the USRMED.f routine.

Intersection Calculation

For the intelligible demonstration, we will use the 2DRMs which are the main tools in this work to explain our intersection calculation algorithm. Then we will elaborate further on how we extended the code for RiFis. Since FLUKA usually calls the parameters by reference, not by value, the first thing to do before starting the calculation is to transfer the directional vector (v_x, v_y, v_z) of the particle to a parameter in the user routine environment. The input data of the heights H, radius r, base layer thickness b, pin period PP, and maximum thickness of the filter D_{max} will be called and saved in the first entry of the particle. Note that the pin axis is always parallel to the the z-axis of FLUKA and the particles are always sent to +z direction.

In this work, the algorithm to calculate the D_{mod} was changed from "the ray-triangle intersection algorithm" (Simeonov et al., 2017, 2022) to this faster but less flexible method using interpolation points for the profile instead of a full STL-data set. The principle of the new calculation is the interpolation between two data points closest to the point of particle intersection. The interpolated product is the height H at which the particle intersects the pin's flank as shown in Figure 3.4.

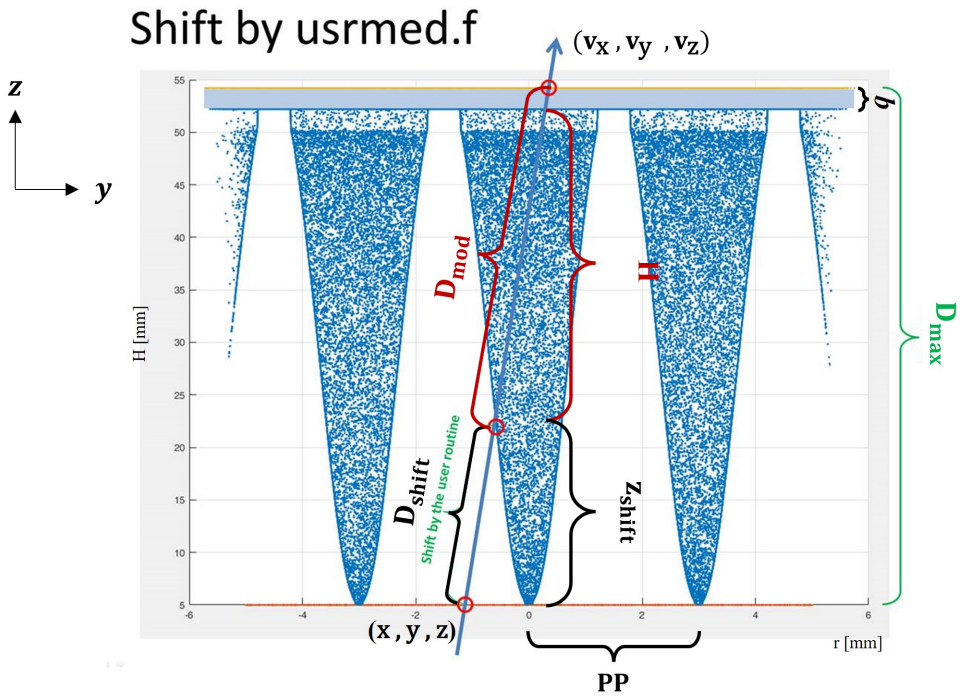

Figure 3.4: The graphical representation of a particle intersecting the 2DRM's pin at the heigh of H when the particle hit the substitute plate at position (x, y, z) with directional vector (v_x, v_y, v_z). The 2DRM has the maximum thickness of D_max, base layer thickness of b and, the pin period of PP. The scatter plots in this drawing were generated using the equivalent algorithm in MATLAB. Basically, the geometrical algorithm was first developed in MATLAB and then translated into FORTRAN.

Since all relevant variables for the calculation align on the z-axis, it is more convenient to normalize the v_z as 1 as follows:

$$\vec{v} = (\frac{v_x}{v_z}, \frac{v_y}{v_z}, 1) \tag{3.1}$$

To start the interpolation, the particle needs to be at the base of the pin or at $H = 0$ with the direction of heading to the pin tip. Therefore, the particle is translated to the base, and the directional vector is switched to the opposite by

$$\vec{x}_{trans} = (x + v_x(D_{max} - b),\ y + v_y(D_{max} - b),\ z + (D_{max} - b)) \tag{3.2}$$

and

$$\vec{v}_0 = -\vec{v}, \tag{3.3}$$

respectively. For the simplicity of the calculation, we narrowed down the boundary of the lateral coordinates to be within the range of $(-PP/2, PP/2)$ or in the area of

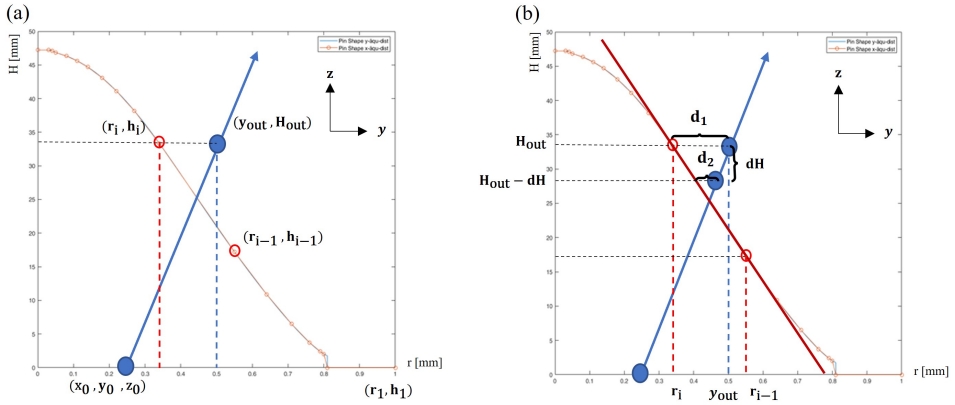

Figure 3.5: (a) The demonstration of a particle intersecting the pin's flank at H_{out} which is between $i-1^{\text{th}}$ and i^{th} pin shape data points. h_1 is the height for the first iteration and (x_0, y_0, z_0) is the new starting point of the particle which is translated from the entrance of the substitute plate. (b) The demonstration of the interpolation of H as a function of d_i or the distance between the particle trajectory and the pin's slope. The interpolated H is the height where d_i is zero.

the central pin (peak position at (0,0)) by

$$x_0 = \left[\left(x_{trans} + \frac{PP}{2}\right) mod(PP)\right] - \frac{PP}{2} \quad \text{and} \quad y_0 = \left[\left(y_{trans} + \frac{PP}{2}\right) mod(PP)\right] - \frac{PP}{2} \tag{3.4}$$

Then the starting point of the particle should be (x_0, y_0, z_0) as shown in Figure 3.5 (a).

The problem can be divided into two main steps:

1. Find the boundary of the problem or find the two data points where the particle intersects between
2. Interpolate H value within this boundary

In the first step, the code will search for the first height which it found that the particle has already left the pin, or H_{out} as shown in Figure 3.5 (a). The iteration will start from the bottom to the top of the pin and will stop if the maximum lateral coordinate of the particle exceeds the radius r_i of the pin, which can be written as

$$x_0 + v_{x_0} h_i \geq r_i \quad \text{or} \quad y_0 + v_{y_0} h_i \geq r_i, \tag{3.5}$$

As the example in Figure 3.5 (a), the particle trajectory in y-component has already left the pin at h_i. Then

$$H_{out} = h_i, \tag{3.6}$$

which means the particle intersect the pin at some point between h_{i-1} and h_i. Next, the code will simply check whether h_{i-1} equals h_i or not. If it is true, that means the particle hit the pin tip or pin groove which H_{out} will become the solution automatically without further interpolation. If they are not equal, it will move to step 2 which is demonstrated in Figure 3.5 (b).

In step 2, we will interpolate H as a function of the distance d_i between the particle trajectory (projected on yz-plane for our example), and the pin's flank with a gradient of $(r_i – r_{i-1})/(h_i – h_{i-1})$. The distance d_i at H_{out} is defined as d_1, and the one at $(H_{out} - dH)$ is defined as d_2, where the height step dH is 0.001 mm, according to Figure 3.5 (b). For the interpolation method, linear interpolation was used which the general form is given by

$$y = y_0 + (x - x_0)\frac{(y_1 - y_0)}{(x_1 - x_0)} \tag{3.7}$$

where y is an unknown at a known value x. In our problem, the equation can be interpreted as

$$H = H_{out} - d_1\frac{dH}{(d_1 - d_2)} \tag{3.8}$$

where the known value x is 0 in our case. Although the solution H is given, the extra deviation correction is needed due to the issue regarding the pin's corner. Since we only interpolate H on one projection plane (yz-plane for our example), it is possible that the particle might still be outside of the pin on the other projection if the intersecting point is very close to the corner. The deviations of the shifted particles are spotted and pointed out by the red arrows in Figure 3.6.

Hereby, the deviations of the shifted particles needs to be checked for both x and y coordinates by adding the iteration, which will be ended only when d_i is equal to or less than the iteration convergence tolerance dT or

$$d_i \leq dT \text{ where } dT = 10^{-6} \tag{3.9}$$

on both projection planes. Finally, the true value of H is determined and the particle is ready to be shifted through the air. The final coordinates of the particle can be

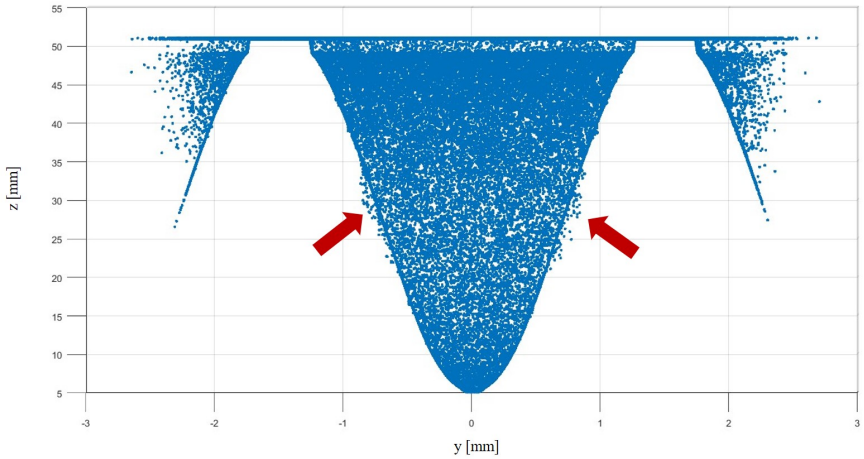

Figure 3.6: The shifted particles outside the pin calculated in MATLAB without the corner correction.

written as

$$\vec{x}' = (x + v_x z_{shift},\ y + v_y z_{shift},\ z + z_{shift}) \tag{3.10}$$

which will be sent back to FLUKA standard executable before the ending of the USRMED.f routine session. The realization of the 2DRM shape by particle shifting calculated in MATLAB is shown in Figure 3.7.

Extended Code for Ripple Filters

Even though the study in this thesis does not cover the inhomogeneity induced by the RiFis, the routine is also extended to them with the same implementation as 2DRMs except for the calculation relevant to the filter's geometries. One explicit difference between the RiFi's and the 2DRM's geometries is the size of the device which the typical thickness of the RiFis is about 3–6 mm, while the 3D-PMs is in the order of centimeters (about 5 cm for the 2DRMs used in this thesis). For the 2DRiFi's pin with a cone shape which is different from the pyramid shape of the 2DRM, the condition for checking whether the particle has already left the pin or not, needs to be adapted (Equation 3.5 for 2DRM case). The modified condition for 2DRiFis can be given as

$$\sqrt{(x_0 + v_{x_0} h_i)^2 + (y_0 + v_{y_0} h_i)^2} \geq r_i \tag{3.11}$$

For the case of 1DRiFis which the height is varied only in 1 dimension, the Equation 3.5 can also be applied for it with only one plane considering (either xz or yz-planes depending on the orientation of the filter). Besides, 1DRiFis have no

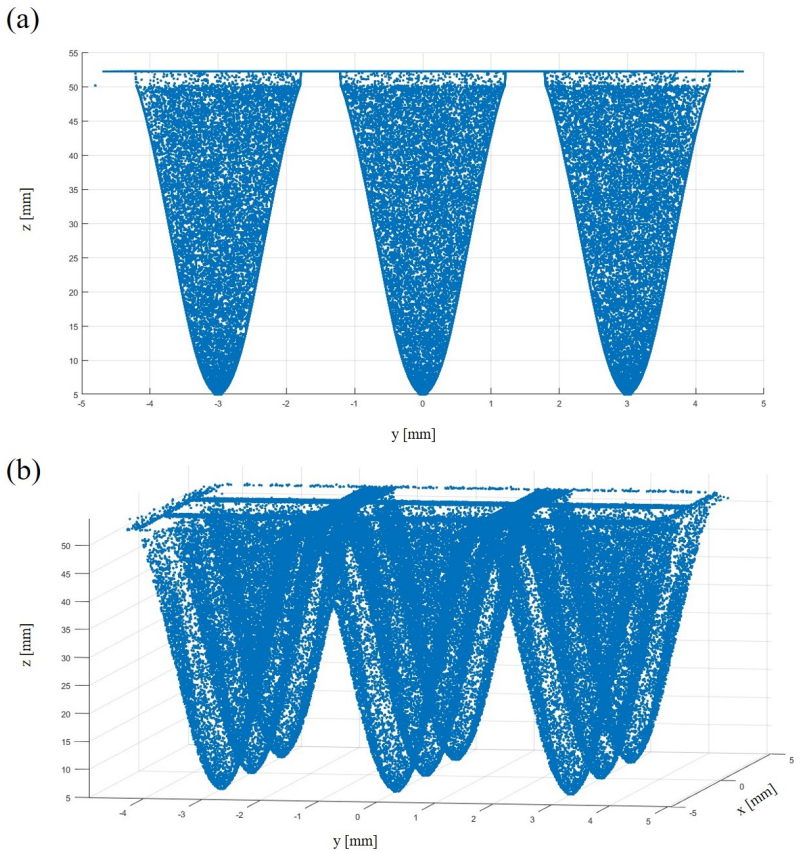

Figure 3.7: Shape of the 2DRM seen from (a) side and (b) oblique view realized by the particles shifted from the entrance of the substitute plate calculated in MATLAB (before translating the code into FORTRAN).

corners, so the correcting iteration is not necessary for this case. The results of particle shifting to the 1DRIF and 2DRiFi simulated by the MATLAB are shown in Figure 3.8

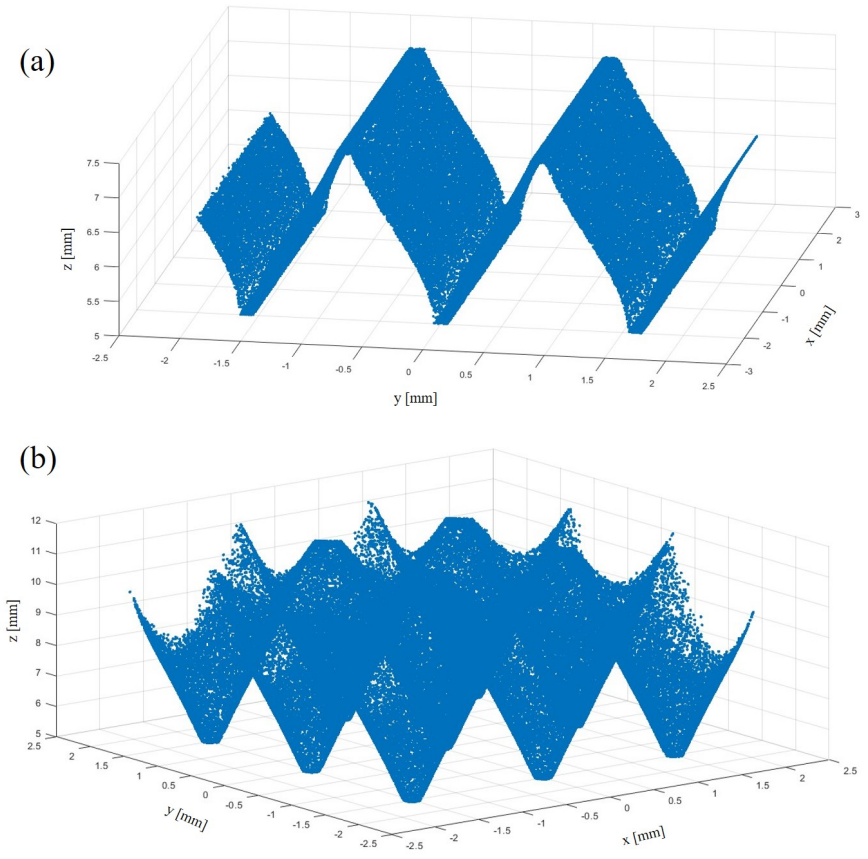

Figure 3.8: Shapes of the (a) 1DRiFi and 2DRiFi (b) realized by the particles shifting calculated in MATLAB (before translating the code into FORTRAN).

3.3 Generic Test of Near Field Inhomogeneities

After the 2DRM implementation was accomplished, the testing of the inhomogeneity simulations was performed by simulating fluence and dose distributions behind the 2DRM. The simulation results were also analyzed in order to evaluate the inhomogeneities at different distances behind the modulator and validate the minimum distance determination method. The sensitivity of the fluence inhomogeneities was also tested, and lastly, the near field simulation in the water target was investigated.

2D Range-Modulator

The 2DRM that was used in this section was optimized for protons of 150 MeV to create a SOBP with a width of 5 cm in the water target. The maximum height of the pin is 45.87 mm with a 2 mm base layer thickness and a 3 mm pin period. The material density was assumed to be 1.206 g/cm^3 with the Water Equivalent Thickness (WET) of 1.186.

Beam Configuration

For the first testing, protons with the initial energy of 150 MeV which is in the middle of the therapeutic range (generally between 70 MeV and 250 MeV of protons) were used. The energy uncertainty is 0.1% of the kinetic energy and the angular spread is relatively small, i.e., 0.5 mrad. A pattern of 10×10 Gaussian spot beams with a variance of 8 mm spot size were superposed to form a homogeneous quadratic field with a total size of about 5×5 cm^2 at the beam generated point. It is important to note that the center-to-center distance of the beams must be smaller than the Full-Width-at-Half-Maximum (FWHM) of the beam size to result in a homogeneous overlapped beam field (Kraft, 2000), therefore the step size of 5 mm was used for this simulation. The beam direction was set to the direction of +z in FLUKA and is parallel to the z-axis.

Simulation Setup

Primary

To generate multiple beams sources in FLUKA, the special source function called "SPOTBEAM" was used. In this card, the user can insert the required beam ener-

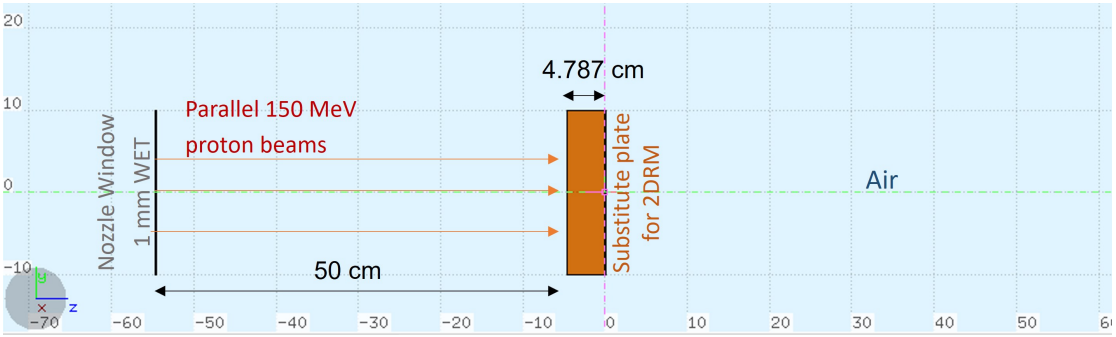

Figure 3.9: Simulation setup for 2DRM generic testing in FLUKA.

gies, energy and angular spreads, and beam geometry for each spot beam. Moreover, this function allows the users to weigh the intensity for each spot which will be beneficial for our simulation in the next sections but for this simulation, the weights will be left equal. The SPOTBEAM card works together with "SPOTDIR" and "SPOTPOS" cards which the users can use to set the spot beams directions and positions. These special source cards need to be activated by selecting the "BEAMSPOT" option in the "SPECSOUR" and, importantly, the number of beams must be specified here.

Alternatively, the users also can customize their source by using "SOURCE.f" routine which is commonly used for generating complicated sources that cannot be described by a general "BEAM" card.

Geometry and Media

The base of the 2DRM was placed at z = 0 cm and the pin tips were at z = -4.787 cm in FLUKA. The dimension of a substitute plate was $20\times20\times4.787$ cm^3 (x y z) which the thickness corresponded to the maximum pin height plus the thickness of the base layer of the modulator. A 1 mm water slab was added as a substitute nozzle window and placed in front of the 2DRM at a distance of 50 cm. The parallel proton beams were generated right in front of the nozzle window slab and the setup environment was surrounded by air. The stoichiometric composition of the 2DRM material was set to (C:5 O:2 H:8) with the density of 1.206 g/cm^3.

Scoring

The 2D proton fluence distributions in the unit of particles/cm^2 per primary weight were scored behind the 2DRM starting from z = 0 cm to z = 50 cm, both in xy- and yz-planes operated by the "USRBIN" card with the option "proton" as the type of

scoring. For xy-plane, the total lateral scoring size was $6\times6\times0.01$ cm^3 (x y z) with one bin in the z-direction and 600 bins in both x- and y- directions, while the total scoring size in yz-plane was $0.01\times6\times50$ cm^3 (x y z) with one bin in the x-direction, 600 bins in the y-direction, and 1000 bins in z-directions.

As described in section 2.4 concerning the edge scattering, the inhomogeneous field behind the periodic structure has a pattern with areas that induce lower scattering (the positions of pin grooves) and areas with stronger scattering (the positions of pin peaks). Thus, fluence distributed in the yz-plane was scored for 2 planes, i.e., at x = 0 cm which is defined as "peak plane" and x = 0.15 cm defined as "groove plane" (the pin period is 3 mm).

Data Analysis

To achieve our main task which is the determination of the "minimum distance d_{min}". behind the modulator at which the inhomogeneity completely disappears, the scored fluence at the different distances z were analyzed and evaluated in a similar manner to the work of RiFis's inhomogeneities evaluation (Ringbæk et al., 2014). For the sake of quantitative comparison, the induced inhomogeneities at a distance z behind the modulator were quantified as a numerical value which is called "fluence ripple (R)" which is mathematically defined as

$$R = \frac{F_{max} - F_{min}}{F_{max} + F_{min}}. \tag{3.12}$$

where F_{max} and F_{min} are the maximum and the minimum fluence at the 5×5 mm^2 squared region in the middle of the field in xy-plane, which the example of the fluence distribution at z = 4 cm is shown in Figure 3.10. This fluence ripple is used as an indicator of the inhomogeneity strength which will increase if the inhomogeneity is stronger. With that being said, we can spot the R that is zero or almost zero in order to determine the d_{min}.

Because of the symmetrical pattern of the fluence on xy-plane, and the fact that the F_{max} always lies in the groove plane (x = 0.15 cm) and F_{min} lies in the peak plane (x = 0 cm), the fluence on groove and peak planes, were used to search for F_{max} and F_{min}, respectively.

To search for F_{max} and F_{min}, the fluence distributions were fitted by a "multiple oscillating fit function" in order to avoid the statistical fluctuations of the data

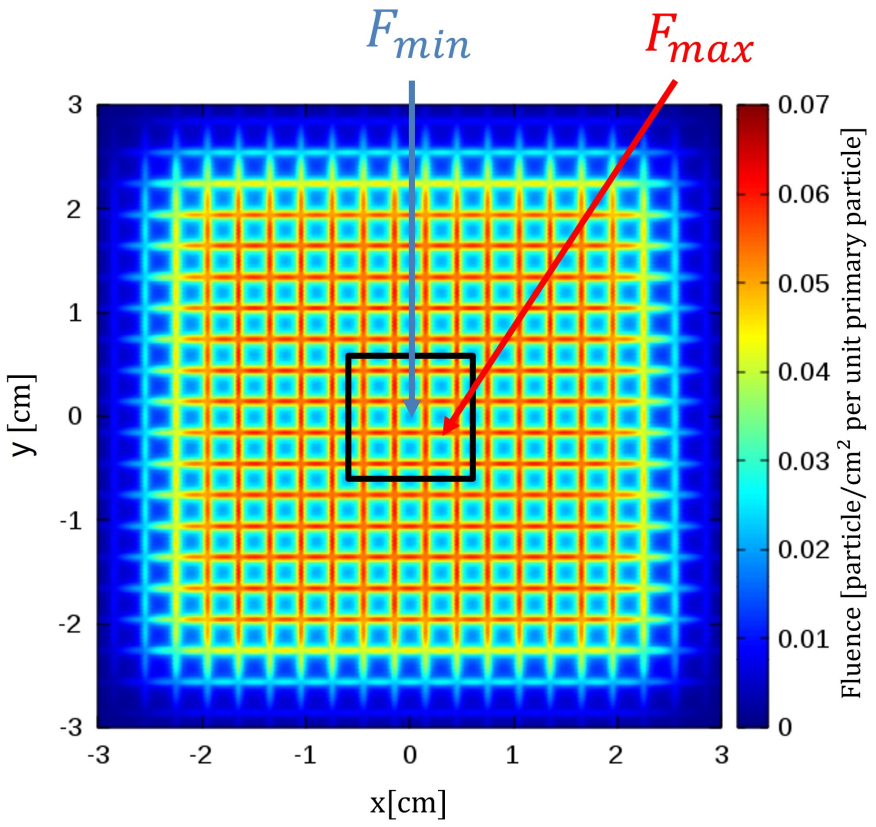

Figure 3.10: Fluence distribution in xy-plane which is at z = 4 cm behind the 2DRM.

because of the tiny volume of the scoring. The fitting equation is given by

$$F(y) = a_0 + \sum_{i=0}^{n} a_i \cos\left(\frac{2n\pi}{PP}y + \phi\right) + \sum_{j=0}^{n} b_j \sin\left(\frac{2n\pi}{PP}y + \phi\right) \tag{3.13}$$

where PP is the pin period of the 2DRM. From the testing, n = 3 is the best fit for this fluence oscillation in the sense that it agreed with the data very well for the oscillation from z = 0 to z = 50 cm, and did not overestimate the fluctuation. The example of the oscillating fit is shown in Figure 3.11. However, the statistical fluctuation can be improved by an increase in the primary particle. Finally, the calculated R can be plotted as a function of distance z behind the modulator. This method was used to evaluate and assess the field inhomogeneities for every part of the work which can be extended to the evaluation of the "dose ripple" in a target as well.

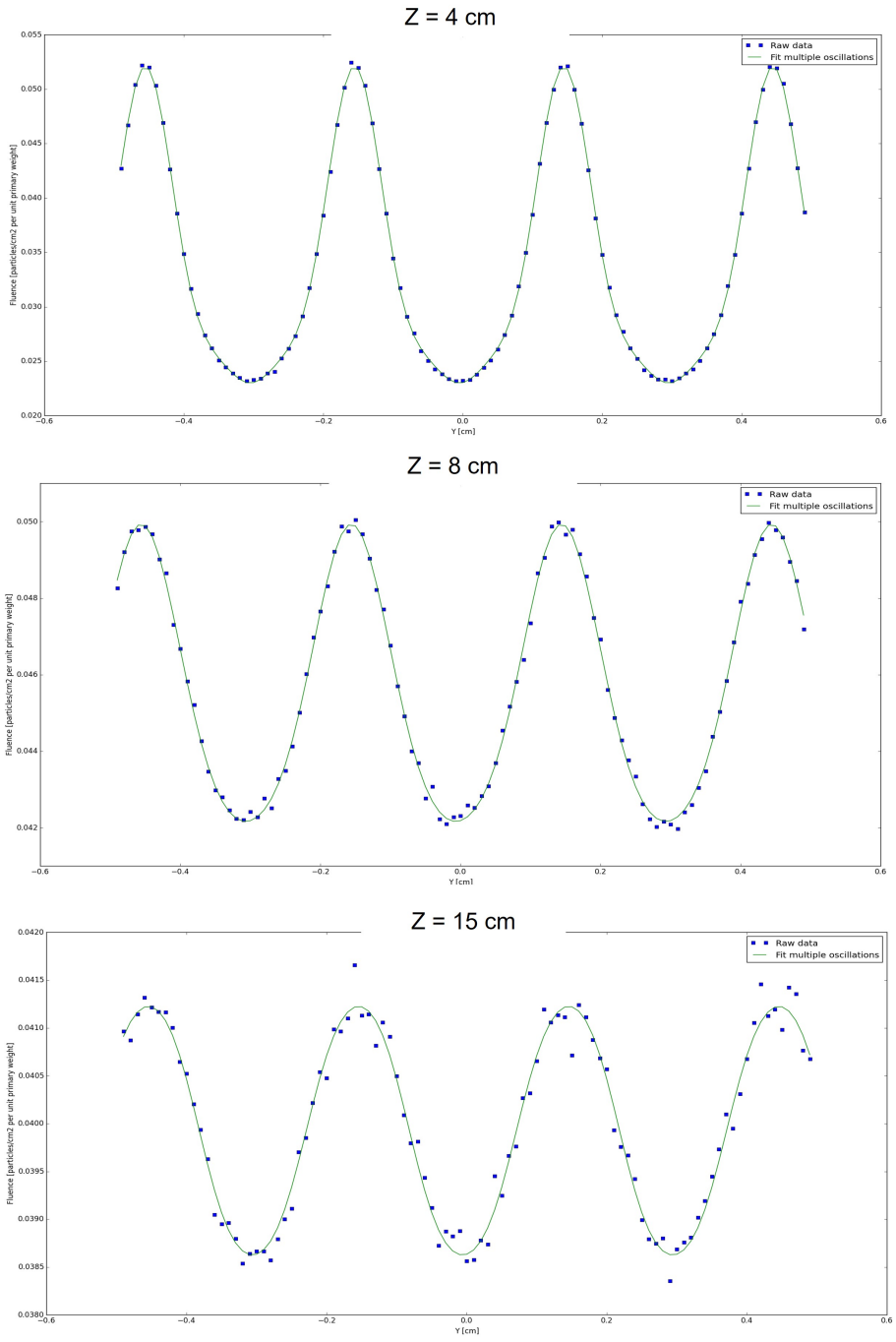

Figure 3.11: Comparison of the fluence oscillations fitted by the multiple oscillating function (green lines) and the raw data (blue dots) at different distances behind the 2DRM.

Dose Distribution in Water Target

Since water is the main component of the body's tissue, it is commonly used as a patient substitute for dosimetry and range measurement in radiotherapy research. Thus, water was added to our simulation as a target material to observe the dose inhomogeneity. After the determination of the d_{min}, water with a dimension of $20\times20\times80$ cm^3 was placed at distance d_{min} behind the 2DRM to ensure the dose homogeneity. The simulation setup remained the same as the fluence scoring and the 2D dose distribution was scored using USRBIN card, the same card as fluence scoring but switched the scoring type from "proton" to "dose". The total scoring size was $20\times20\times25$ cm^3 with 800 bins in the z-direction and 1 bin in both x- and y- directions. The depth dose distribution around the central axis was also scored with the size of $20\times20\times0.3$ cm^3 (x y z).

Sensitivity Test

Apart from the determination of d_{min}, the behavior of such inhomogeneity was also studied further by testing the sensitivity of the inhomogeneity to 3 parameters, i.e., the initial energy varied by 100, 150, 220 MeV, the initial variance of angular distribution varied by 1, 2, 3 mrad, and the pin period varied by 2, 3, 4 mm.

Moreover, in the case of energy variation, near field simulations in water were also investigated when the water target was placed 2 cm behind the modulator. The dose inhomogeneities appearing in the water were analyzed and quantified the same as the ripple function.

3.4 Comparison of the Film Experimental Data and FLUKA Simulation

For the third part of the thesis, the fluence ripple simulated by FLUKA was compared with the film measurement data in order to verify the simulation results. The film measurement was carried out at the Danish Centre for Particle Therapy (DCPT) at Aarhus University Hospital, Denmark, by the joint work of the researchers from the radiation physics group, biophysics division, GSI Helmholtzzentrum für Schwerionenforschung, Institut für Medizinische Physik und Strahlenschutz, Technische Hochschule Mittelhessen (THM), Germany, DCPT, Denmark and *Varian Medical*

Systems. The experiment was also a part of the FLASH irradiation technical testing with the clinical facilities of *Varian Medical Systems* using 2DRMs.

Gafchromic EBT-3 film Measurements

The radiochromic film is one of the dosimetry methods in radiotherapy research. Rather than being used for precise dosimetry, radiochromic films have the advantage to visualize the irradiation field projected on the film. For this reason, the radiochromic films were used for observing the field inhomogeneity behind the 2DRMs in this work. The film that we used was "*Gafchromic EBT-3*" film (Sorriaux et al., 2013) which has the property to form blue-colored polymers when the active components are exposed to radiation, which in turn reduces the light transmission property of the films. The examples of the *Gafchromic EBT-3* films are shown in Figure 3.12 where the transformed color can be seen in the middle of the films. After irradiation, all films were scanned with an *Epson Expression 12000XL Pro scanner* by using the triple-channel film dosimetry method (red, green, and blue channel) (Micke et al., 2011; Lewis et al., 2012) with a resolution of 72 ppi (1 pixel = 0.357 mm). In conjunct with the image processing software called *ImageJ*, the Optical Densities (OD) of every pixel on the films were obtained and converted to doses in Gy unit by the calibration functions which are shown in Figure 3.13 (The calibration functions and film measurement data that used in this thesis were given by Dr. Mateusz Sitarz, DCPT, Denmark). Lastly, the converted doses were averaged over red, green, and blue channels for better statistics.

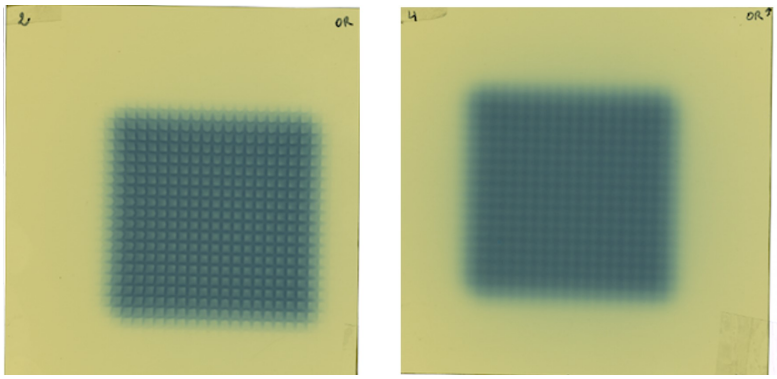

Figure 3.12: The examples of the Gafchromic EBT-3 films exposed by scanned proton beams.

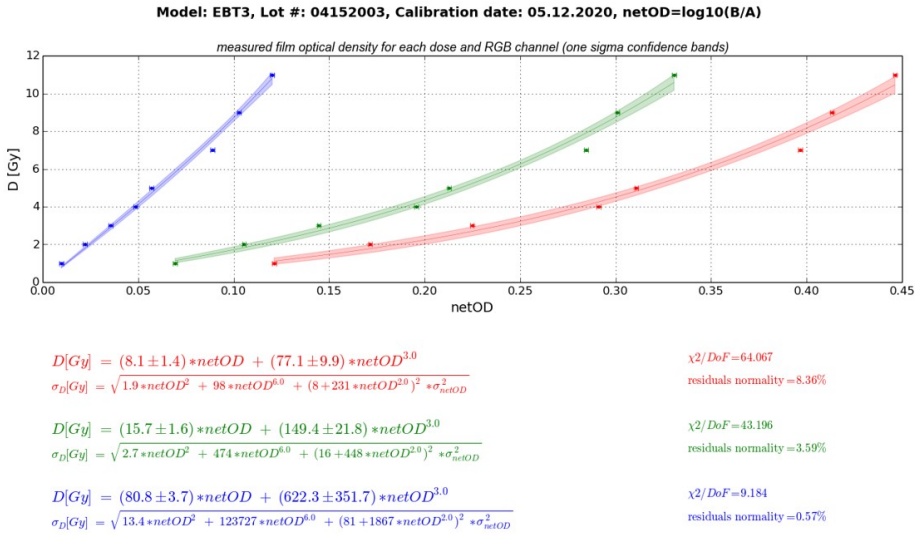

Figure 3.13: The calibration curve of dose in a unit of Gy and netOD which is the subtraction of the Optical Density (OD) of a film after and before it was irradiated. Figure courtesy from Dr. Mateusz Sitarz, DCPT, Denmark.

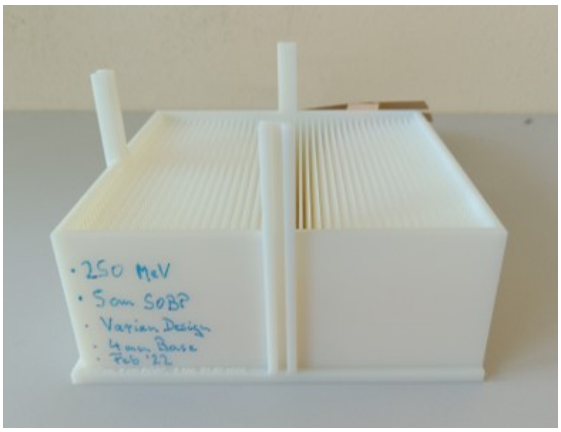

Figure 3.14: The 2DRM designed specifically for a 5 cm SOBP and for application of FLASH irradiation performed with *Varian*'s proton facilities.

2DRM for Radiochromic Film Measurements

In this part, the 2DRM with a 3×3 mm^2 base and 44 mm height which is shown in Figure 3.14 was used. It was designed for creating a 5 cm SOBP by irradiation with 250 MeV protons with the addition of the energy absorbers. A Stratasys Objet30-Pro 3D-printer and a propriety material (RIGUR RGD450, Stratasys) were used for manufacturing the modulator. Its composition is similar to Polypropylene and has a density of 1.206 g/cm^3.

Scaninng Divergency

For the other two parts of the thesis, the simulation followed the clinical setup according to the proton machine called *Varian ProBeam®* which the information was given by *Varian Medical System*. One thing that was added to improve the accuracy of the simulation is the beam divergence resulting from the magnetic scanning. The simplified schematic illustration of the scanning beam geometries is shown in Figure 3.15 in which the top is the projected view on the xz-plane and the bottom is on the yz-plane. The small pencil beam which initially focused on the central axis is deflected in the y direction by the scanner magnets y and deflected again by the scanner magnets x after penetrating in the vacuum for 56 cm.

To simulate the scanning beam in FLUKA, the deflected angles were calculated for every spot beam to hit the predetermined lateral position at the isocenter plane. The resulting angles were inserted in the SPOTDIR card in the form of direction cosines with respect to the beam axis. The schematic representation of the direction cosines is shown in Figure 3.16. Thus, if the position of the spot beam projected at the isocenter plane is (x, y) as shown in the example of Figure 3.15, the

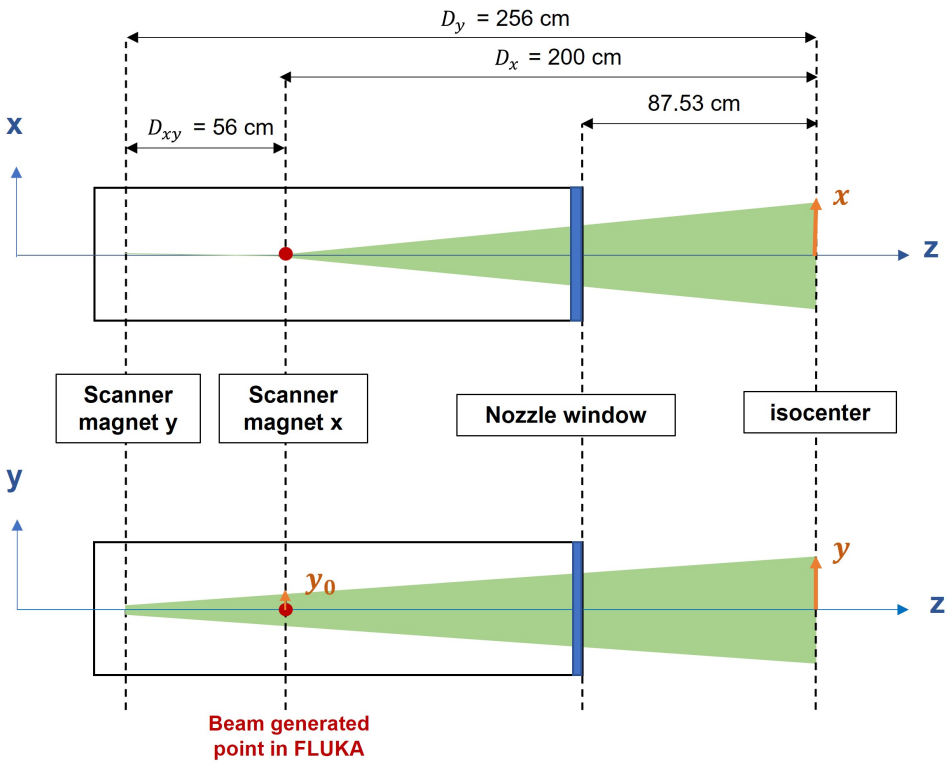

Figure 3.15: Schematic illustration of the beams deflected by the scanner magnets x (top) and y (bottom) according to the *Varian ProBeam®*.

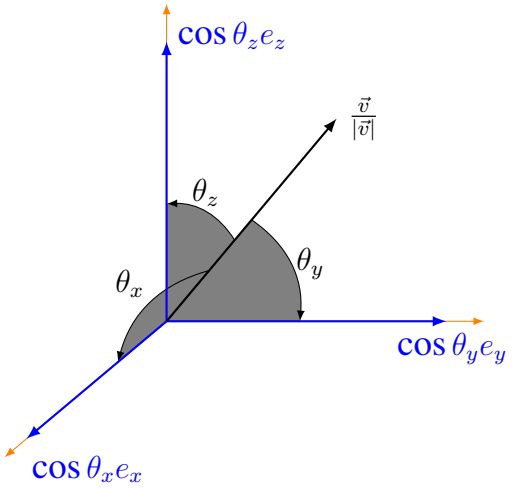

Figure 3.16: Schematic illustration of direction cosines and direction angles of vector $\vec{v}$.

direction cosines of this spot beam after being bent by the scanner magnets x and y can be calculated as

$$\cos\theta_x = \frac{x}{\sqrt{x^2+(y-y_0)^2+D_x^2}}, \quad \cos\theta_y = \frac{y-y_0}{\sqrt{x^2+(y-y_0)^2+D_x^2}}, \quad and$$
$$\cos\theta_z = \frac{D_x}{\sqrt{x^2+(y-y_0)^2+D_x^2}}. \tag{3.14}$$

Since we chose to generate the beam at the virtual position of the scanner magnets x (0 cm in FLUKA) where the beams are already deflected in y direction, the initial position of y or y_0 had to be calculated as well which can be givened by

$$y_0 = y\frac{D_{xy}}{D_y}. \tag{3.15}$$

The testing of the beam divergence calculation will be elaborated on in the beam spotlist subsection.

Beam Spotlist

The beam spotlist optimized for the experiment was also used in this simulation (provided by Dr. Simon Busold and Yuri Simeonov, THM, Germany). The spot width is roughly 8 mm FWHM at the isocenter. Total size of about 6×6 cm^2 of a homogeneous quadratic field at the isocenter was formed by a pattern of 10×10 beam spots with a 6 mm step size. Additionally, the intensities of the beam spots at the border were slightly boosted-up by 5% in order to sharpen the lateral fall-off.

Before we started the main task in FLUKA, the initial beam parameters had to be calculated and determined, i.e., the beam positions spread in the y direction (y_0), the beam scanning deflected angle, and the initial spot size which makes the spot width roughly 8 mm at the isocenter. Small testing was conducted for 2 cases. First, the beam spot was sent directly to the isocenter without the deflection, or the spot position was aimed at (0 cm, 0 cm) (x y) at the isocenter plane. Second, the aimed spot was at (-2.7 cm, -2.7 cm) which was the case that needed the largest deflection relative to the other spot in the list. The initial beam spot size was varied to accomplish the beam width of about 8 mm at the isocenter for both cases. The final solution was 5.8 mm FWHM at the beam-generated point that could send the spot beams of 8.04 and 8.06 mm to the positions (0 cm, 0 cm) and (-2.7 cm, -2.7 cm) on the isocenter plane, respectively. The resulting beam spots at the isocenter plane for both testing cases are shown in Figure 3.17 and the scanning divergency of every beam in the spotlist is shown in Figure 3.18. According to this testing, 5.8 mm was used as the initial spot size for the simulations of the last two sections of this work.

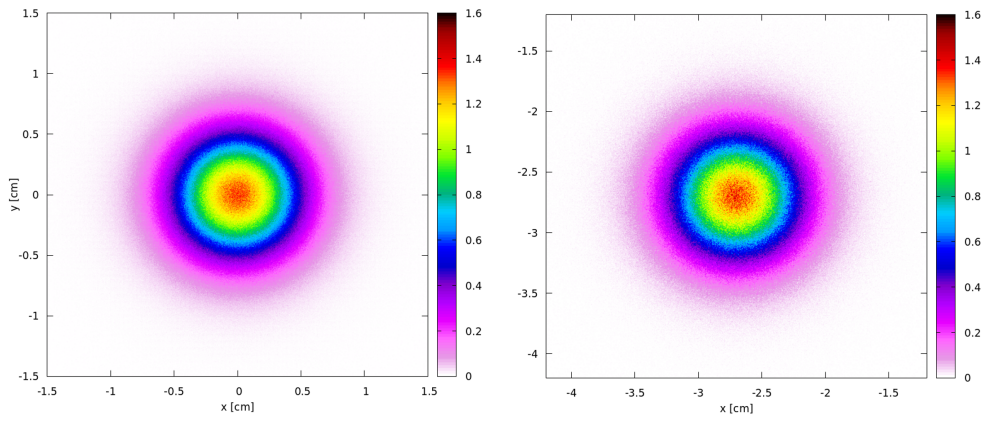

Figure 3.17: Beam spots on the isocenter plane at (0 cm, 0 cm) (left) and (-2.7 cm, -2.7 cm) (right).

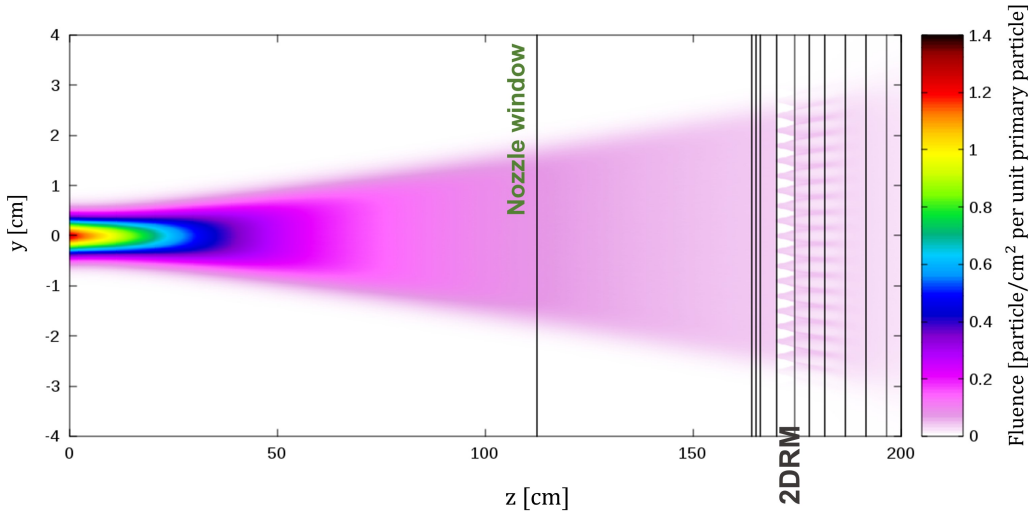

Figure 3.18: The scanning divergency in y-direction of the beams used for the simulation of film measurement setup.

Film Measurement Setup

The experimental setup is shown in Figure 3.19 where the *ProBeam®* proton therapy system from *Varian Medical Systems* was used for generating and delivering the beam to the target. The beam passed through an ionization chamber (IC), the 2DRM, PMMA absorber plates (4 plates) of 19 cm total thickness and was stopped in a water phantom (Schuy et al., 2020). The front window of the water phantom was positioned at the isocenter plane and the 2DRM was positioned 25.5 cm upstream of the isocenter.

The films were irradiated with proton beams whose configuration corresponded to the aforementioned spotlist. The energy of the proton FLASH beams which initially was 250 MeV, was decreased as the beam traversed through the energy absorber, yielding 10 Gy dose in the middle of SOBP (250 MeV was used in this experiment to achieve a sufficiently high proton current without beam loss from the scattering with the degrader in order to enable FLASH dose rate). The energy spectrums after protons passed through the PMMA absorbers with a total thickness of 19 cm are shown in Figure 3.20, in which the highest energy was around 150 MeV.

Radiochromic films (*Gafchromic EBT-3*) were placed at different distances behind the modulator to observe the development of the inhomogeneities. The film1 was attached to the front of the modulator. The other films were attached to the

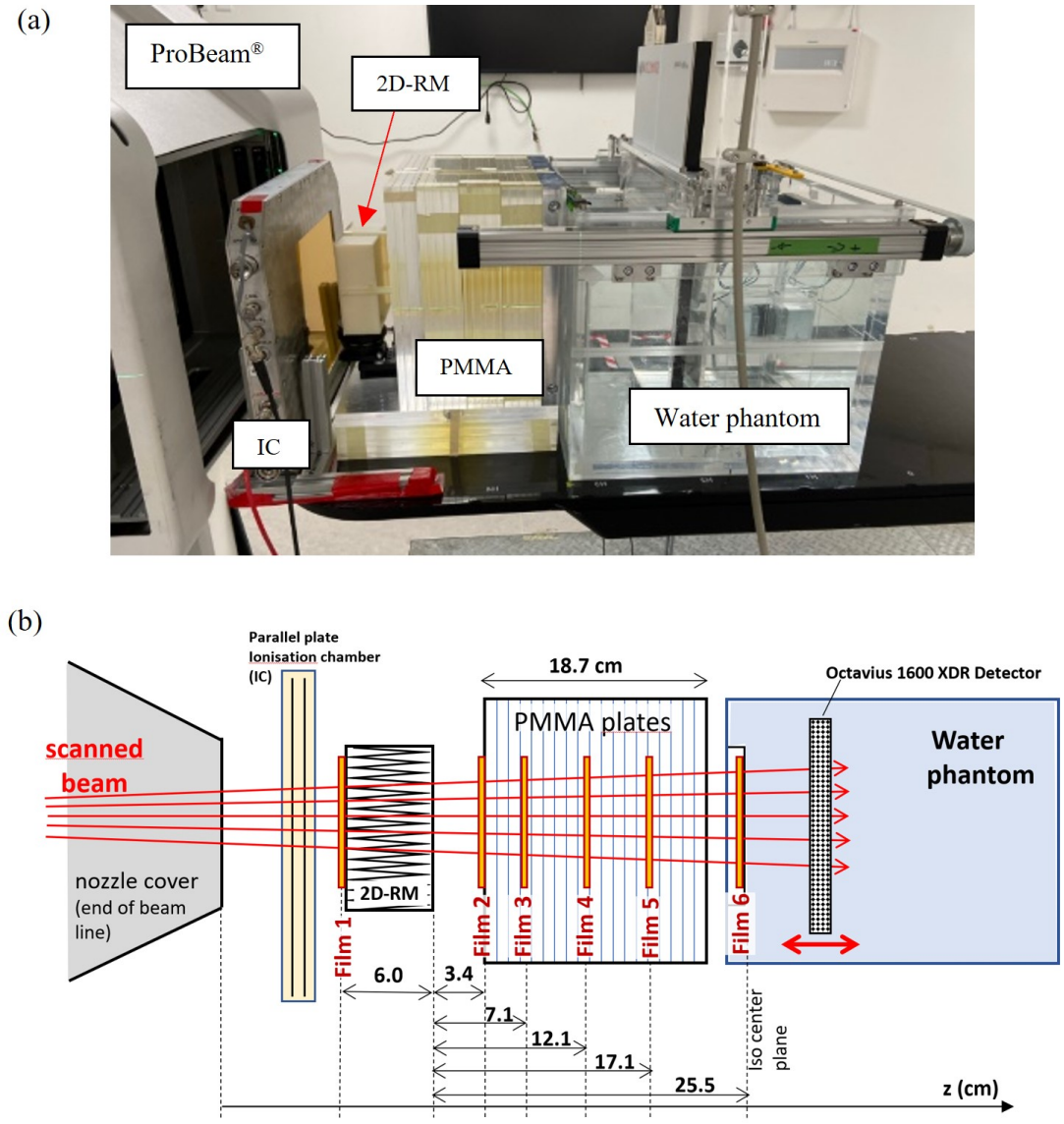

Figure 3.19: (a) Experimental setup at the Danish Centre for Particle Therapy (DCPT) at Aarhus University Hospital, Denmark, and (b) a schematic drawing of the experimental setup with the film positions.

energy absorbers where the distances from the modulator of film2 to film6 were 3.4, 7.1, 12.1, 17.1, and 25.5 cm, respectively.

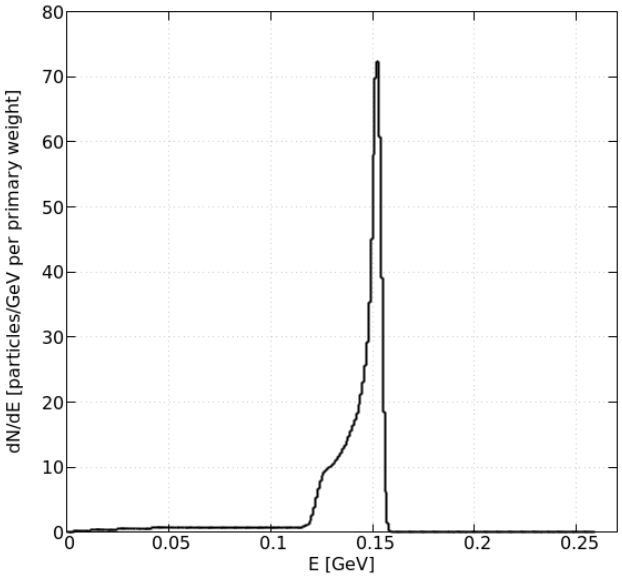

Figure 3.20: Energy spectrum of protons after passing through the PMMA absorber plates simulated by FLUKA. The peak of the spectrum after protons left the absorbers was at around 150 MeV.

FLUKA Simulation

To perform our simulation, the simplified but significant geometries, and the physical properties of the materials of the experimental devices were inserted in the FLUKA standard input file, except for the 2DRM which was implemented with the help of a special USRMED.f routine (see section 3.2). The lateral dimension of all geometries in the simulation was 20×20 cm^2 for ensuring a larger area than the beam field. The FLUKA geometrical setup corresponds to the experimental setup. The z = 0 cm is the beam origin (scanner magnets x), and z = 200 cm is the position of the isocenter. A 1 mm homogeneous water slab was added as a water equivalent nozzle substitute and was placed at the position of the exit window. The simulation setup according to the film measurement setup is shown in Figure 3.21.

The lateral fluence distributions were scored at the virtual positions of the films. The total scoring size was $80\times80\times0.03$ mm^3 (x y z) with one bin in the z-direction and 600 bins in both x- and y- directions. Moreover, the depth dose distribution around the central axis in the water phantom was also scored with the scoring size of $2\times2\times0.06$ cm^3 and $20\times2\times0.06$ cm^3.

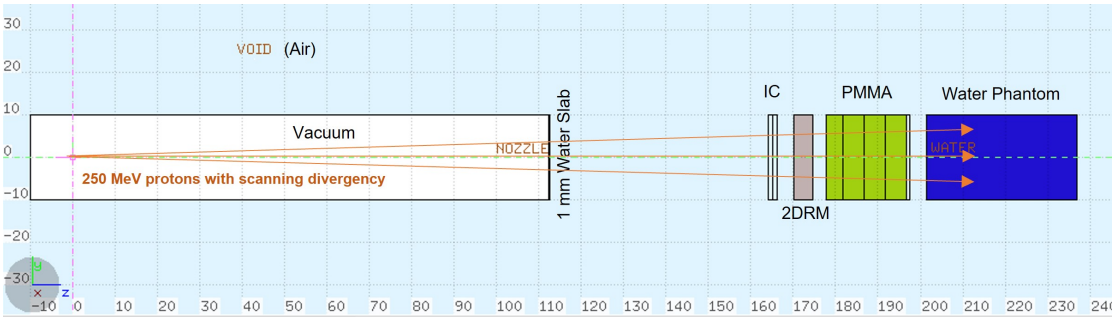

Figure 3.21: The setup for the radiochromic film measurement in FLUKA, corresponding to Figure 3.19 above.

3.5 Near Field Inhomogeneities in the Target

For the last simulation, the clinical setup of *Varian ProBeam®* with the water phantom at the isocenter position was kept as the setup of the previous section. The difference was that the ionization chamber and the PMMA absorber plates were taken off in order to put the 2DRM close to the water resulting in the near field inhomogeneity in the water target. Moreover, the distance between the modulator and the water surface was also varied by 2, 10, 16, and 50 cm to observe the fluence ripple developing in air and water. Since the energy absorbers were not included in this simulation, the proton beams with energy of 150 MeV were used instead of 250 MeV, with the same beam configuration of the spotlist. The simulation setup for the near field simulation in the water phantom is shown in Figure 3.22.

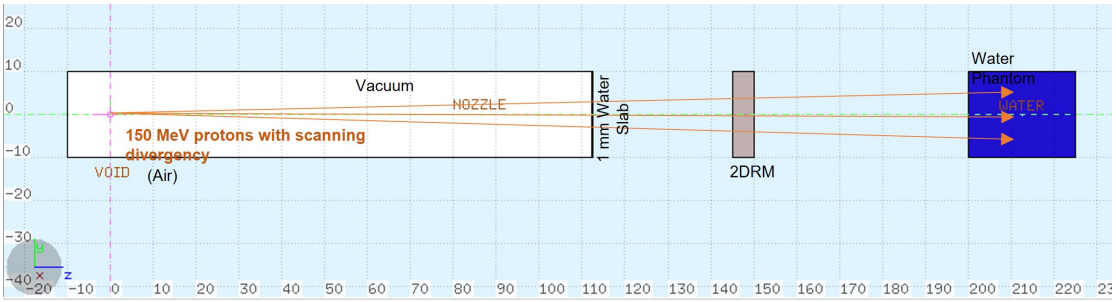

Figure 3.22: The geometrical setup for near field simulation in FLUKA according to the clinical setup of *Varian ProBeam®* for a 50 cm distance from the water phantom.

Chapter IV

RESULTS AND DISCUSSION

4.1 Generic Study of Near Field Inhomogeneities

Determination of the Required Distances of the Modulator for Treatment

Observation of the Fluence Distribution behind the Modulator

For the first generic test, the 2DRM optimized for 150 MeV protons to create a 5 cm SOBP, was simulated to observe the lateral fluence distribution at different distances in a range from 0 up to 50 cm from the modulator. The development of the inhomogeneity along the air at different distances z behind the modulator projected on the xy- and the yz-planes, were exhibited in Figure 4.1 and Figure 4.2 (a), respectively. It can be seen that the fluence pattern recreates the arrangement of the modulator's pins in which the lateral positions of the pin's grooves are painted by the maximum fluence (at first, lays between the sides of the pins and later is focused on the corners), while the lateral positions of the pin's peaks are always occupied by the minimum. The strong inhomogeneities were observed from z = 1 to z = 20 cm and then gradually blurred out due to the overlapping of the contributions from the single pins.

Since the graphical visualizations are vague to define the strength of the inhomogeneity, the inhomogeneity was quantified as the percentage of the fluence ripple which was plotted against the distance from the modulator shown in Figure 4.2 (b). In this way, the dependence of the inhomogeneity on the distance is more convenient to observe. For the tested 2DRM of 150 MeV protons, the fluence ripple starts off at 30% right behind the modulator and reaches the maximum at 4 cm with a ripple of 48.6%. Then, the ripple decreases continuously and converges to zero. According to this fluence ripple plot, the minimum distance for preventing dose ripples, which from now on will be called d_{min}, can be determined as 40 cm

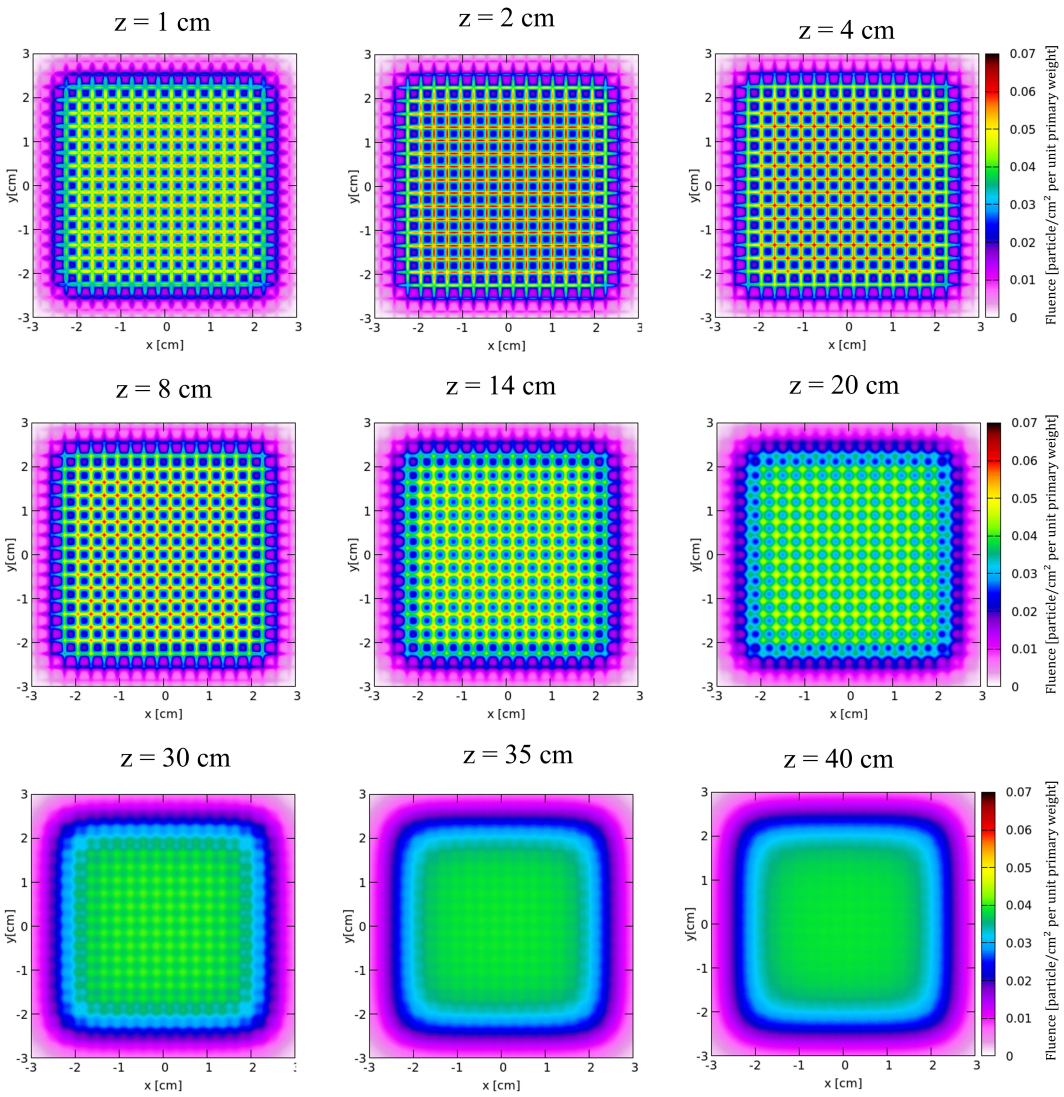

Figure 4.1: The development of the field inhomogeneity at different distances behind the 2DRM optimized for 150 MeV protons to create a 5 cm SOBP, which is visualized by the lateral fluence distribution of protons in the xy-plane.

with a ripple of 0.06%.

(a)

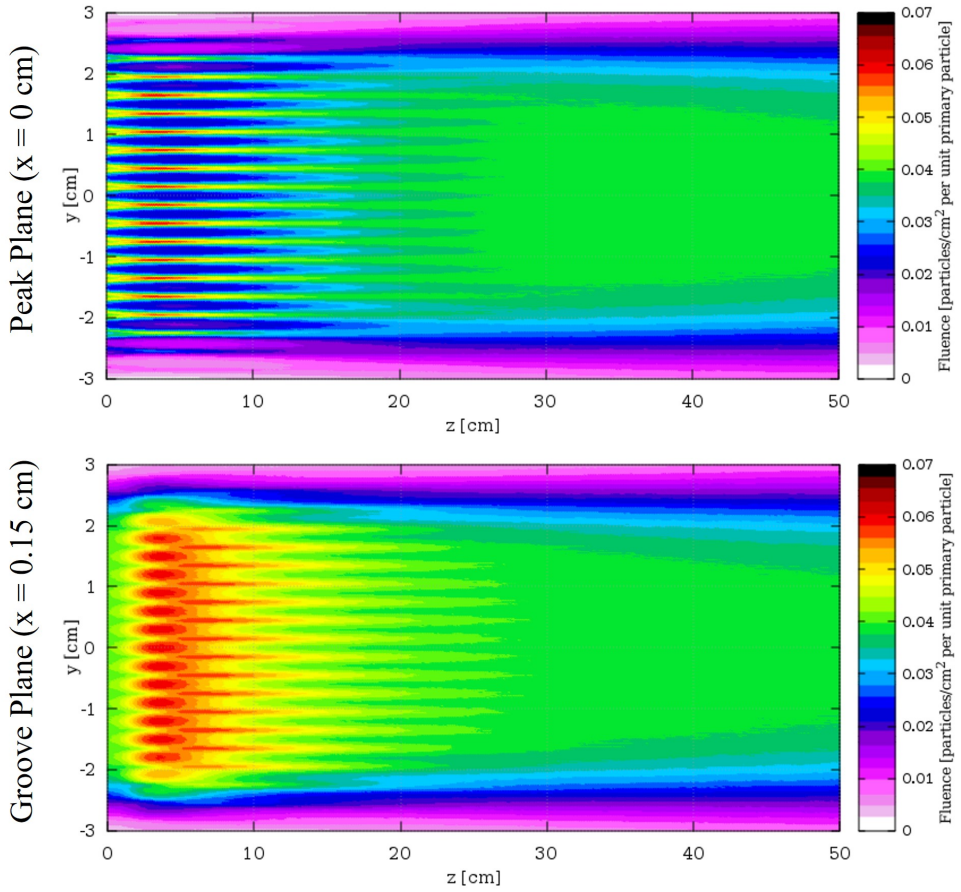

(b)

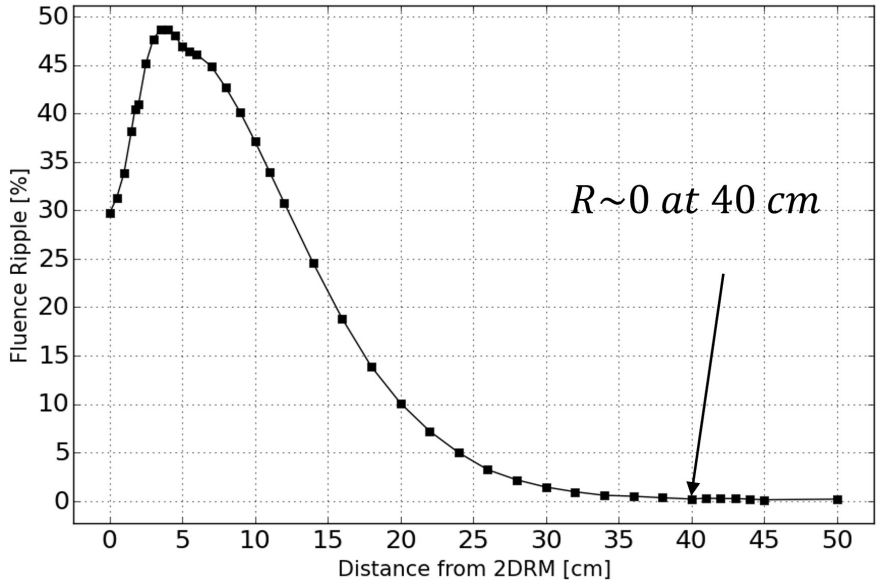

Figure 4.2: (a) 2D fluence color plots behind the 2DRM in the peak (x = 0 cm) and groove (x = 0.15 cm) planes and (b) the percentage of the fluence ripple plotted against distance from the 2DRM which is a more convenient way to determine the d_{min}.

This fluence ripple curve has the characteristic which always rising up at the beginning and reaching the peak then falling down until it becomes zero. The increasing fluence ripple at the first few centimeters is described by the large difference between the increased fluence at the groove and the decreased fluence at the peak plane induced by the scattering of the particles with the 2DRM's pins. However, the maximum fluence ripple does not occur at 0 cm because if we zoom into the area of the contact between the 2DRM and the air shown in Figure 4.3, it can be seen that the scattered particles from the two adjacent pins, do not intersect each other right behind the modulator but a few centimeters behind it. This is because of the gap between the pins that make the particle intersecting points further away which is the reason behind the location of the maximum fluence ripple located at 4 cm behind the 2DRM instead of 0 cm. Furthermore, it was also found that the larger gap of the pins, the further the location of the maximum fluence ripple, which will be described later in the discussion of the fluence ripple sensitivity from the pin period.

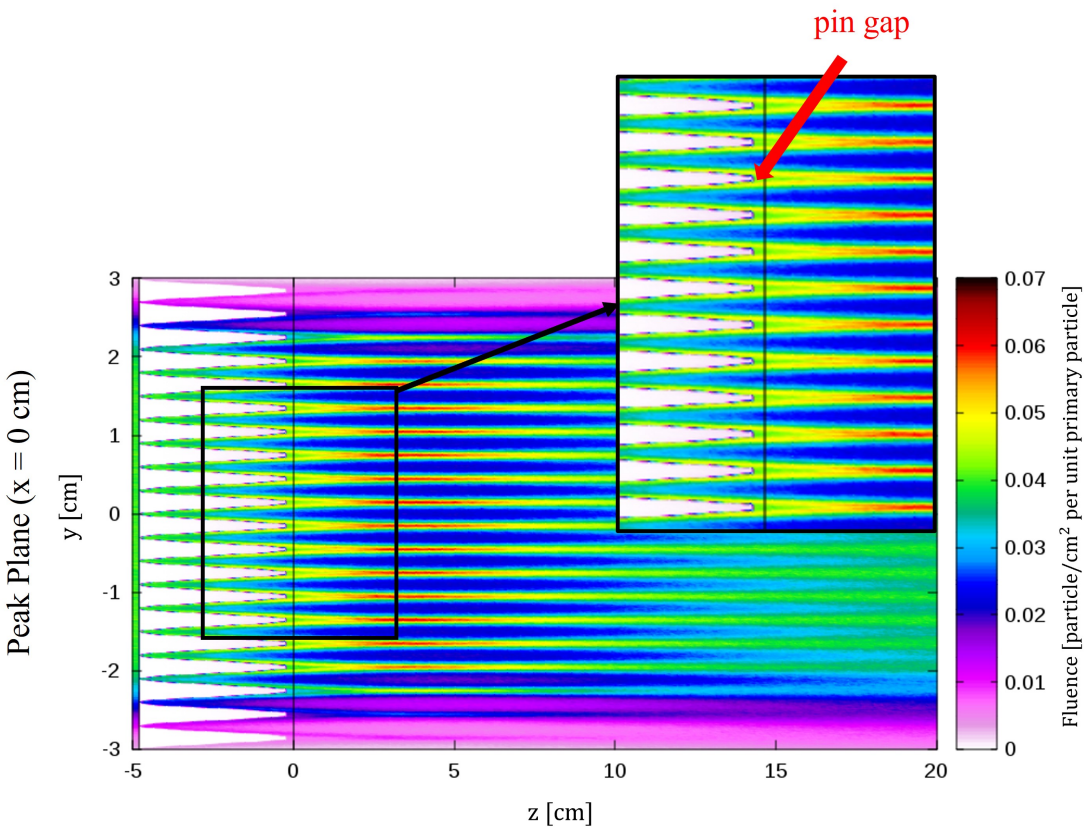

Figure 4.3: The 2D particle fluence in the peak plane (x = 0 cm) between the contact of the 2DRM and the air; area of the pins is zoomed additionally.

After the fluence ripple reaches the peak, it falls down continuously which is

mainly because of the merging of the contributions from the single pins as the beams translate in the air and therefore regaining homogeneity. The multiple Coulomb scattering is the main factor for the lateral spreading of the beam and accelerate the overlapping of the particles. This effect will be elaborated again in section 4.3 in which the fall-off of the fluence ripple was observed in different medium, i.e., air and water.

Another interesting characteristic of the fluence ripple curve induced by the 2DRM which is distinct from the RiFi is the double peak feature. This is mainly because of the nature of the F_{max} which at first, lays between the sides of the pins and later is focused on the corners which is specifically demonstrated in Figure 4.4. As mentioned above, the first peak is caused by the intersection of the scattered particles from the closest pins which is the reason why the F_{max} is spotted between the sides of the pins. Since the particles continue to expand in both lateral dimensions as they moving further away from the 2DRM, the particles gathering again at the pin's corners which is the cause of the occurrence of the second peak. 5 cm (marked by the black dash line) is the position of the valley between the two mountains-like peaks which is at the transition of the lateral positions of the F_{max}.

To determine d_{min}, one aspect to be aware of is the fluctuation of the data in the far field region (>30 cm behind the modulator). Since the field becomes homogeneous in this region, the difference between the F_{max} and F_{min} is very small. Thus, the data fluctuation becomes noisier which can cause an overestimation of the fluence ripple. For this reason, the number of the primary particles generated in the simulations should be large enough to suppress the fluctuations in the data (in this work, more than 5×10^9 primary particles were simulated). Alternatively, one can also relieve the fluctuation by lowering the order of the fitting function to a single-phase sinusoidal function in the far field region.

Another aspect that should be carefully considered are the yz-planes that were used to search for the F_{max} and F_{min} for the purpose of calculating the fluence ripple. Usually, the peak (x = 0 cm) and groove planes (x = 0.15 cm) were used to search for the F_{min} and the F_{max}, respectively (see data analysis in section 3.3). However, the F_{max} does not exactly locate in the middle of the groove between the pins for the very short distances (about one centimeter and can be further for protons with higher energy) behind the modulator because of the pin's gap which separates the scattered contributions of the adjacent pins (see Figure 4.3). This can be noticed

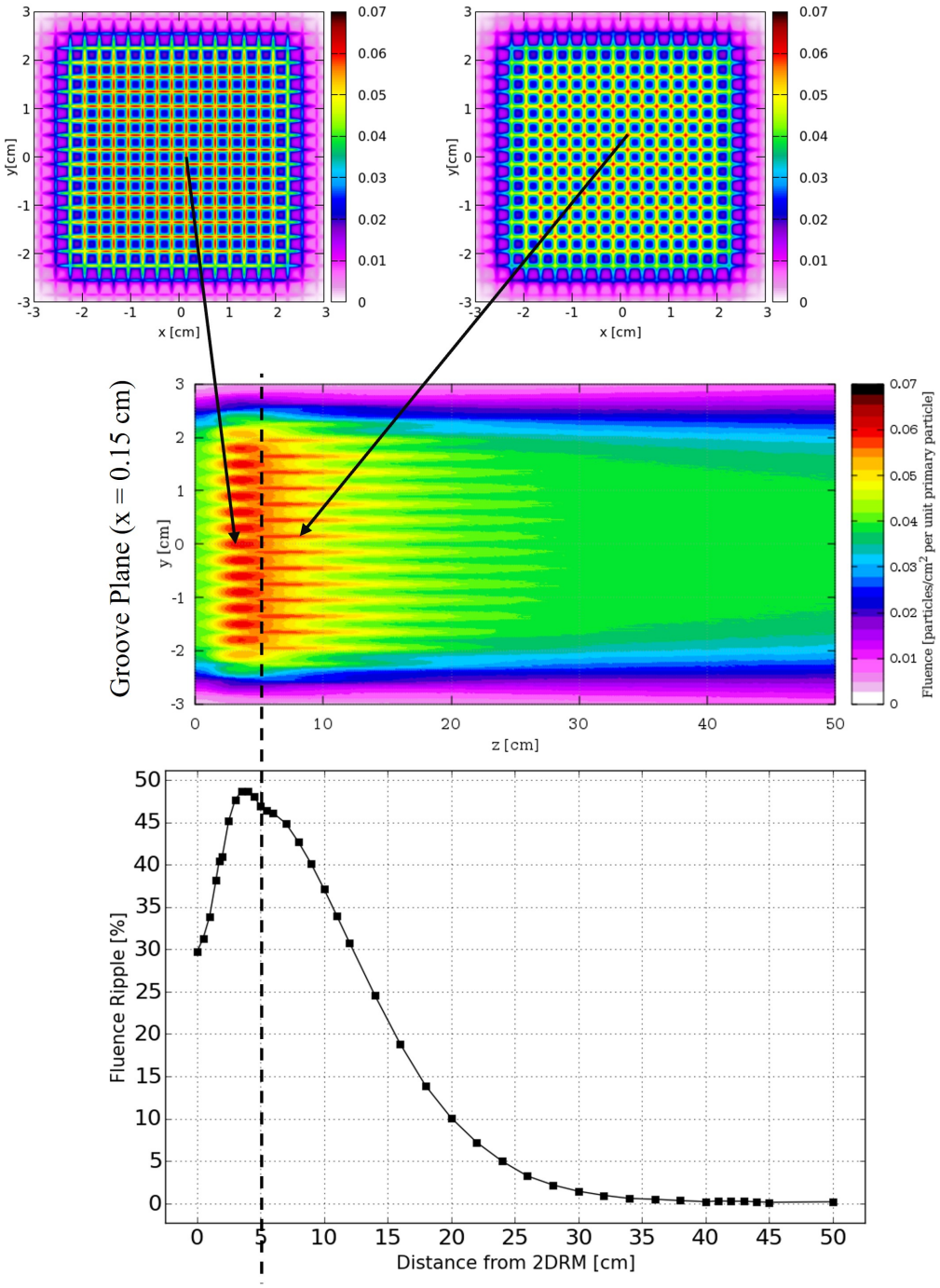

Figure 4.4: The change of the lateral positions of the maximum fluence which is the reason behind the double peak characteristic of the fluence ripple curve.

by the absence of the F_{max} in the groove plane at the very first centimeter behind the 2DRM (see Figure 4.2 (a)). Nevertheless, these separated contributions still can be seen in the peak plane. Hence, the peak plane was used to search for both the F_{max} and the F_{min} at the first one centimeter behind the modulator in order to avoid underestimated fluence ripples which caused from the lower F_{max} picked up from the groove plane.

Study of the Dose Homogeneities in Water

After the d_{min} was determined, the dose distribution in the water target was observed in order to ensure a homogeneous field at the determined distance (40 cm for this case). The 2D dose distribution and the laterally-integrated depth dose distribution presented in Figure 4.5 show that the field is completely homogeneous at the surface of the water, which makes it feasible to be applied for the treatment. Thus, 40 cm is verified to be the mandatory distance for this tested 2DRM to be placed in front of the target.

This result also shows that our simulation can produce a 5 cm SOBP which verifies the complicated design and pin shape for the tested 2DRM. Moreover, the dose homogeneity at the SOBP region also implies good modulating properties of our simulated 2DRM. This strongly confirms of our 2DRM implementation method in FLUKA.

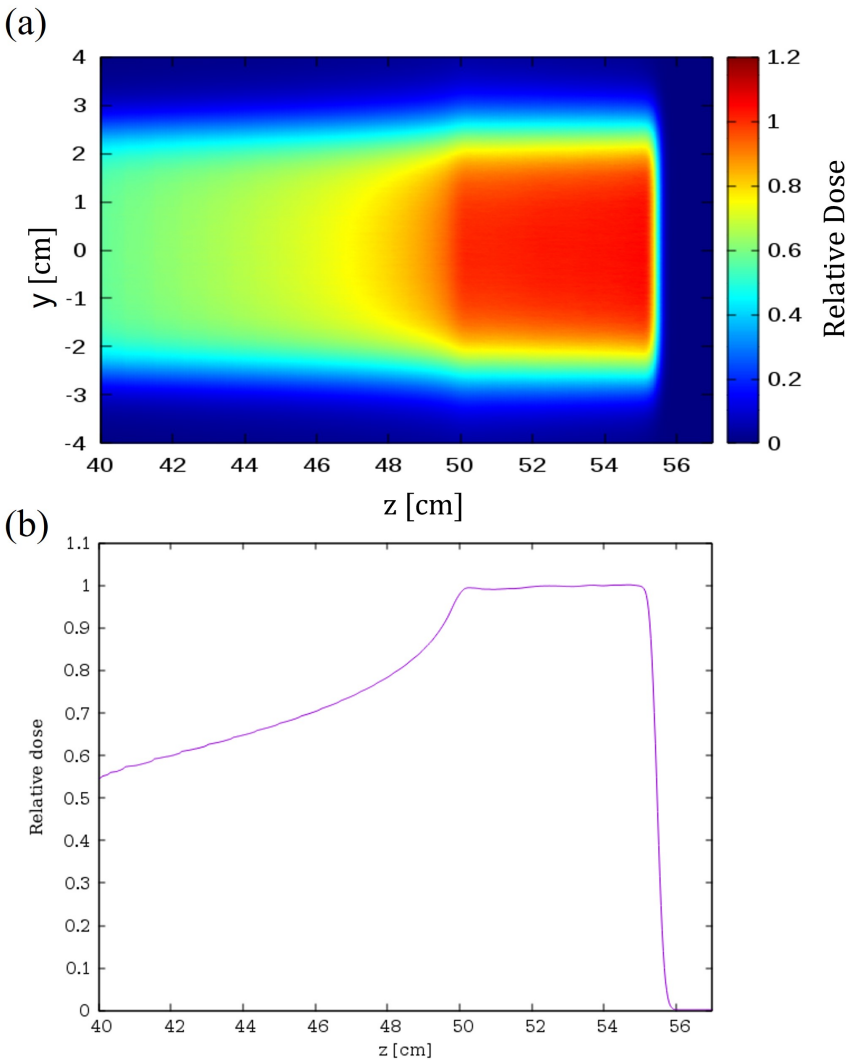

Figure 4.5: (a) 2D dose distribution and (b) fully-integrated depth dose distribution produced by the irradiation of 150 MeV protons with the 2DRM when the modulator was placed at the determined d_{min} or 40 cm behind the modulator.

Testing of Sensitivity of Fluence Ripple

Apart from the dependence on the distance from the modulator, the further investigation revealed that the inhomogeneity is sensitive to the other parameters such as the beam initial energy, the initial angular distribution, and the pin period of the modulator.

The investigation found that the fluence ripple has a strong dependence on the beam energy. For this sensitivity testing, the energy was varied by 100, 150, and 220 MeV which are considered to be low, intermediate, and high energies, respectively, in the therapeutic range. Figure 4.6 shows that the higher the energy, the further the inhomogeneity can penetrate, which agrees with the explanations of the Highland's formula (equation 2.6) and the edge scattering effect (see sections 2.1 and 2.4) regarding the correlation between the projectile's kinetic energy and the scattering angle.

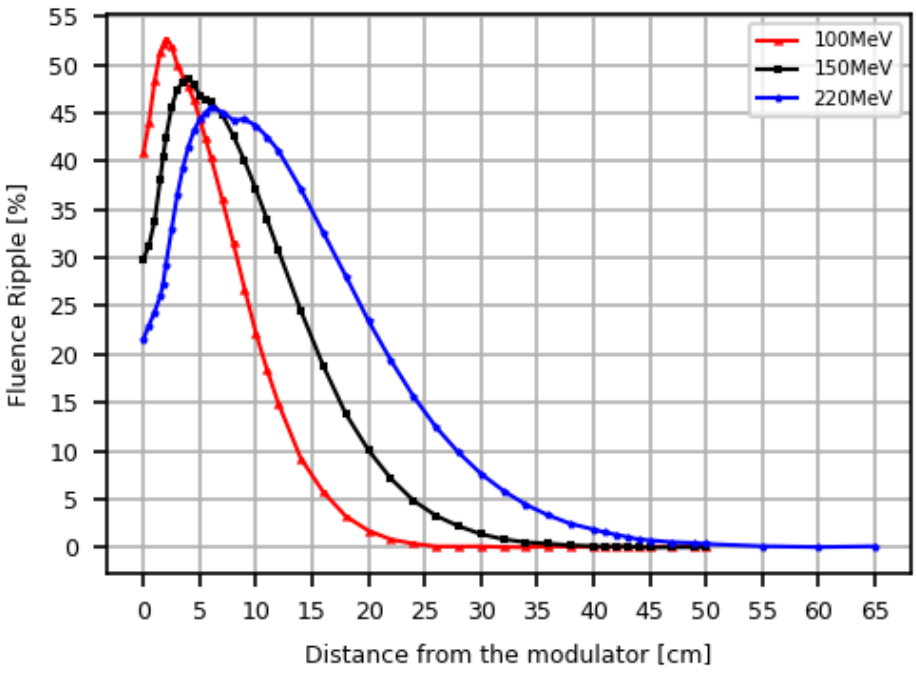

Figure 4.6: Dependence of the fluence ripple on the initial energy of particles which was tested by 100, 150, and 220 MeV of protons.

Since the lower energy protons scatter with larger angles, their traveling paths overlap faster resulting in a faster convergence to zero of the fluence ripple. For 220 MeV protons, the d_{min} is 50 cm, which is considerably larger than the d_{min} of about 30 cm for 100 MeV protons. Therefore, initial energy is one of the significant

factors that need to be considered when deciding the position to place the 3D-PMs in the clinics. Moreover, the inhomogeneity for the lower energy particles tends to be stronger, which can be explained for a similar reason above. Because of the stronger deflection for a proton with lower energy, a greater number of particles are scattered off their straightforward trajectory and gather at the focusing point, resulting in a larger difference in particle fluence between lower and stronger scattering areas, or in another words, stronger inhomogeneity.

The increase in the initial angular distribution generated in front of the nozzle window only causes a slight decrease in the strength of the inhomogeneity. Additionally, the deviations of the d_{min} are also small (< 6 cm) when compared to the sensitivity to the beam energy. In this range of deviation, the fluence ripple does not deviate so much (less than 2%) which is still acceptable for the treatment. Moreover, if we consider the case of the clinical setup, which includes the materials in the beamline, this small deviation from the initial beam divergence will be dominated by the scattering through the additional materials. So, it becomes less of a priority to be considered compared to the other testing parameters.

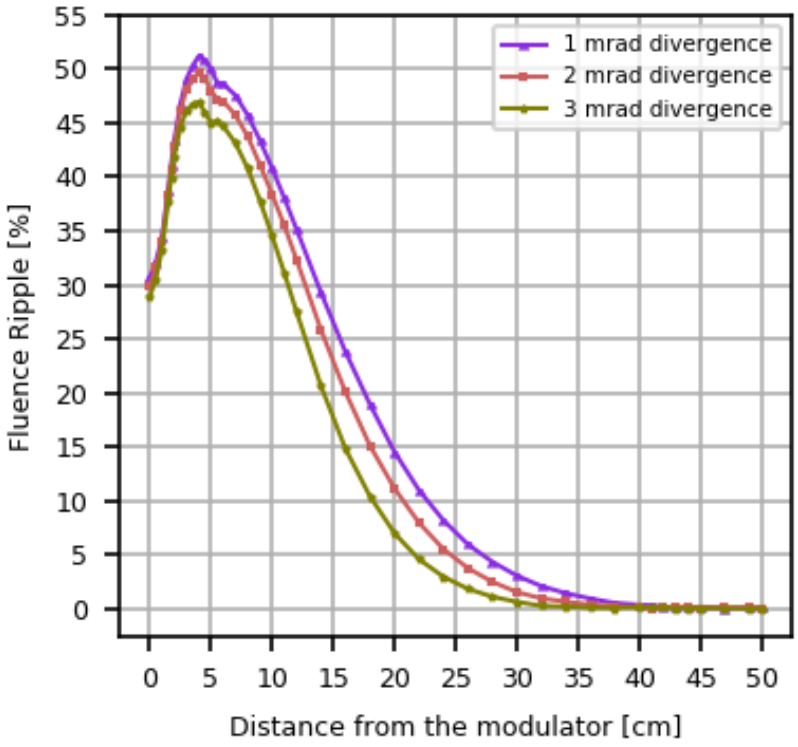

Figure 4.7: Dependence of the fluence ripple on the initial angular distribution which tested by the value of 1, 2, and 3 mrad.

Apart from the sensitivity to the beam parameters, the parameters regarding the modulator structure such as the pin period also affects the strength of the inhomogeneity. Since the beam parameters were fixed to be 150 MeV protons with a beam divergence of 0.5 mrad, the strength of the scattering effect is almost the same for the 3 cases represented in Figure 4.8 which can be noticed by the small deviation of the maximum fluence ripple (<1.6%). However, the enlarged gap between the pins increases the distance that the beams will intersect and overlap each other, resulting in a further d_{min}. Like the dependence on the beam initial energy, the minimum distance for the case of a 4 mm pin period is 50 cm, which is significantly larger than the minimum distance of about 30 cm for a 2 mm pin period. Therefore, the pin period also plays a significant role in the deviation of the inhomogeneity which should not be neglected.

According to the hypothesis of the tissue sparing effect induced by the fractionated beams (see section 2.6) plus the second advantage of higher dose conformity when the modulator is put as close as possible to the target, the near field simulation was also performed. In this case, the 2DRM was placed very close to the water surface, i.e., 2 cm, so the dose inhomogeneity appears in the water as well.

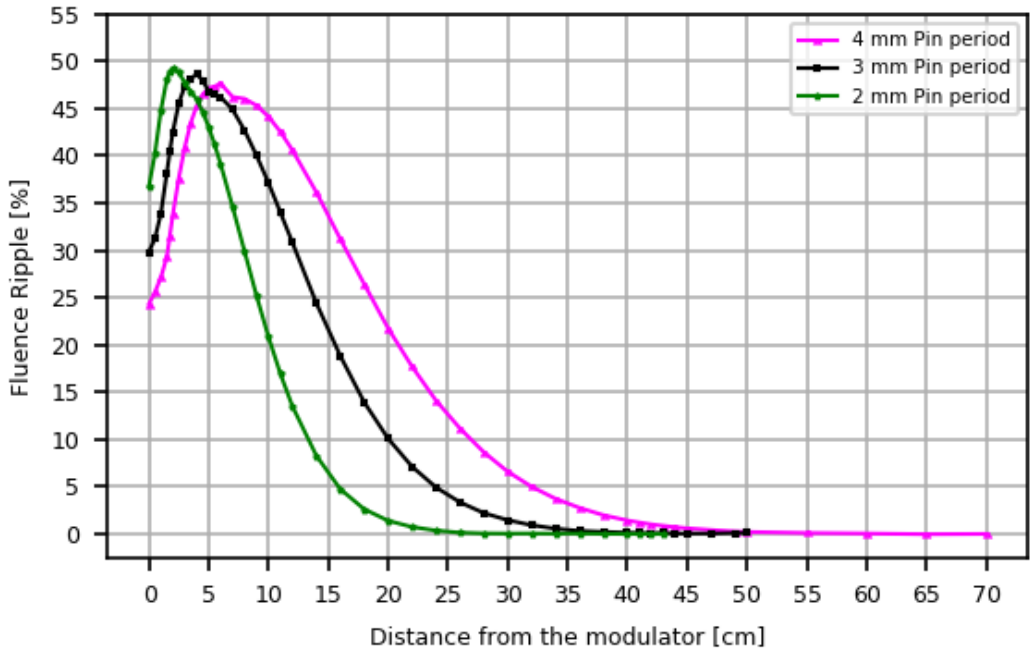

Figure 4.8: Dependence of the fluence ripple on the pin period which tested by 2, 3, and 4 mm of pin period.

The dose inhomogeneities in the water induced by protons with the energy of 100, 150, and 220 MeV passing through the 2DRM, are shown in Figure 4.9. The strong inhomogeneities are spotted in front of the target, especially in the case of 100 MeV which has a short range in water, hence the inhomogeneous dose can still reach the target region (SOBP region).

To avoid the interference of the dose inhomogeneity on the target, we also investigated further at what energy the inhomogeneity starts to leave the target region, which will be a compromise between the advantages of the small distance of the modulator and the dose homogeneity at the SOBP. The investigation results are shown in Figure 4.10 in which the percentages of the dose ripple are presented. The vertical markers indicate the positions of the proximal edge of the SOBP which are around 7, 8, and 10 cm in the depth of the water, for protons with an energy of 130, 145, and 150 MeV, respectively. It can be seen that the inhomogeneities for the protons of 130 MeV and 145 MeV do not reach zero but still have magnitudes of 2.3% and 2% at the proximal edge. The minimum energy at which the dose ripple is blurred away (with a magnitude of 0.04% at the proximal edge of the SOBP), is 150 MeV.

Hence, the minimum energy that is safe to perform the close modulator setup is 150 MeV. Note that this energy was given from the investigation of the 2DRM designed for a 5 cm SOBP. For the case of the wider SOBP, we assume the higher energy to be applicable, while the lower energy might be available for the smaller SOBP.

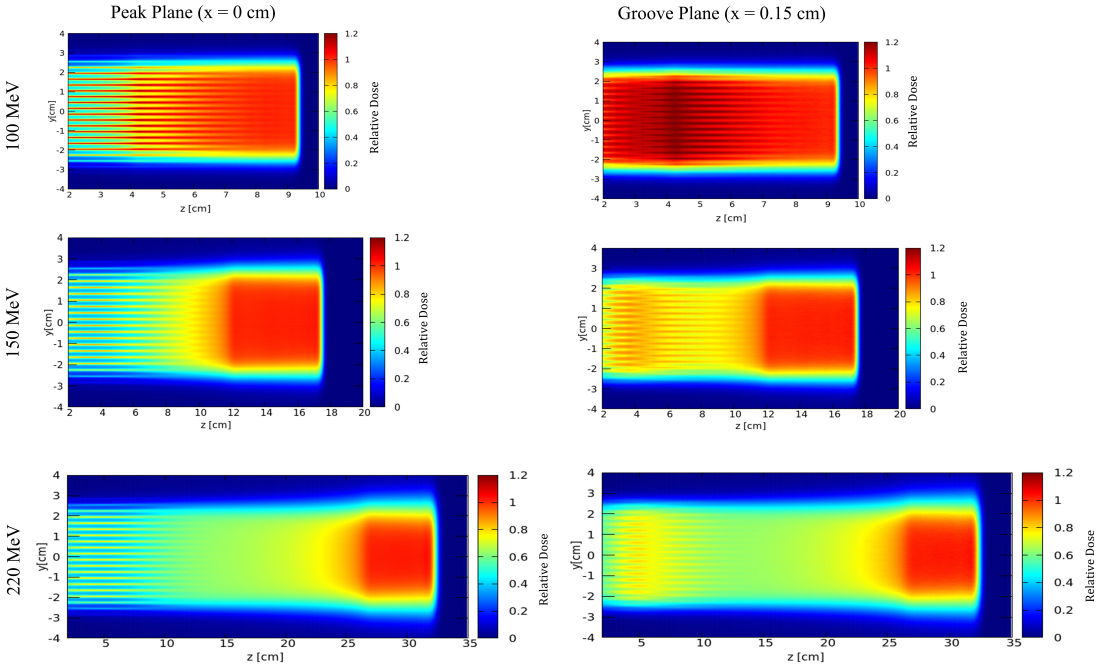

Figure 4.9: 2D dose distributions for 100, 150, and 220 MeV of protons in water when the 2DRM was placed 2 cm in front of the target.

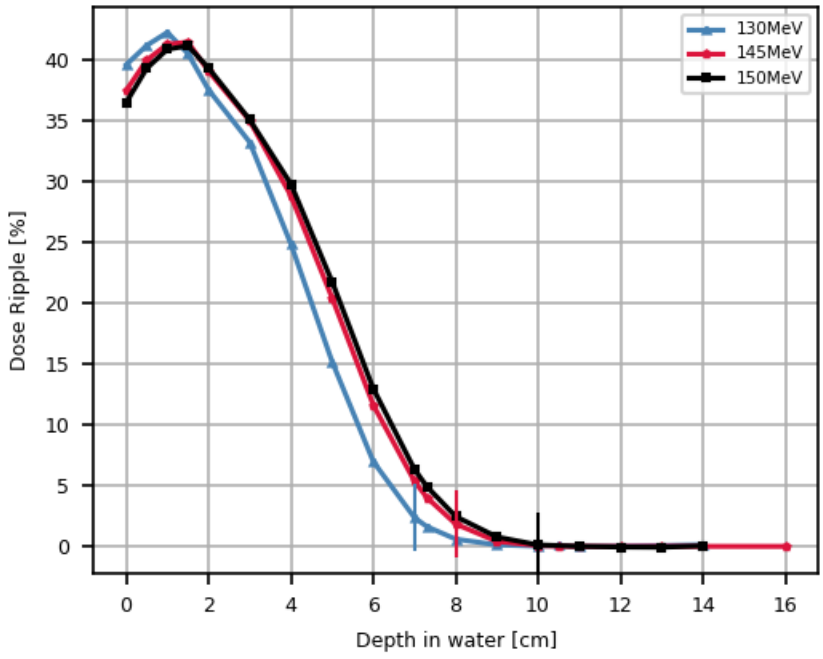

Figure 4.10: The plot of the dose ripple as a function of water depth induced by the 2DRM when the 2DRM is placed at 2 cm in front of the water.

4.2 Comparison of the Film Experimental Data and FLUKA Simulation

Comparison of the Film Measurement and FLUKA Simulation

The comparison of the lateral fluence distributions between FLUKA simulations and film measurements is shown in Figure 4.11 and their selected data are plotted in Figure 4.12 showing the comparison of the shapes of the beam field at different distances from the modulator. Note that the data were normalized by the mean values of the fluence at the middle of the field. Moreover, a visualization of the fluence oscillation induced by the periodic structure of the 2DRM is shown in Figure 4.13 (a) with the represented percentages of the fluence ripple as a function of the distance shown in Figure 4.13 (b).

The film measurement results in Figure 4.13, Figure 4.11, and Figure 4.12, show that the strongest inhomogeneity appeared on the closest film to the modulator (film2) with a fluence ripple of 29.8%, then decreased and completely blurred out at the position of the film5 or 17.1 cm behind the modulator which can ensure the homogenous field at the isocenter (position of the film6). The simulations agreed with the measurements and revealed the actual location of the maximum inhomogeneity with a ripple of 36.7% which was between the film2 and the film3 or around 6.3 cm behind the modulator.

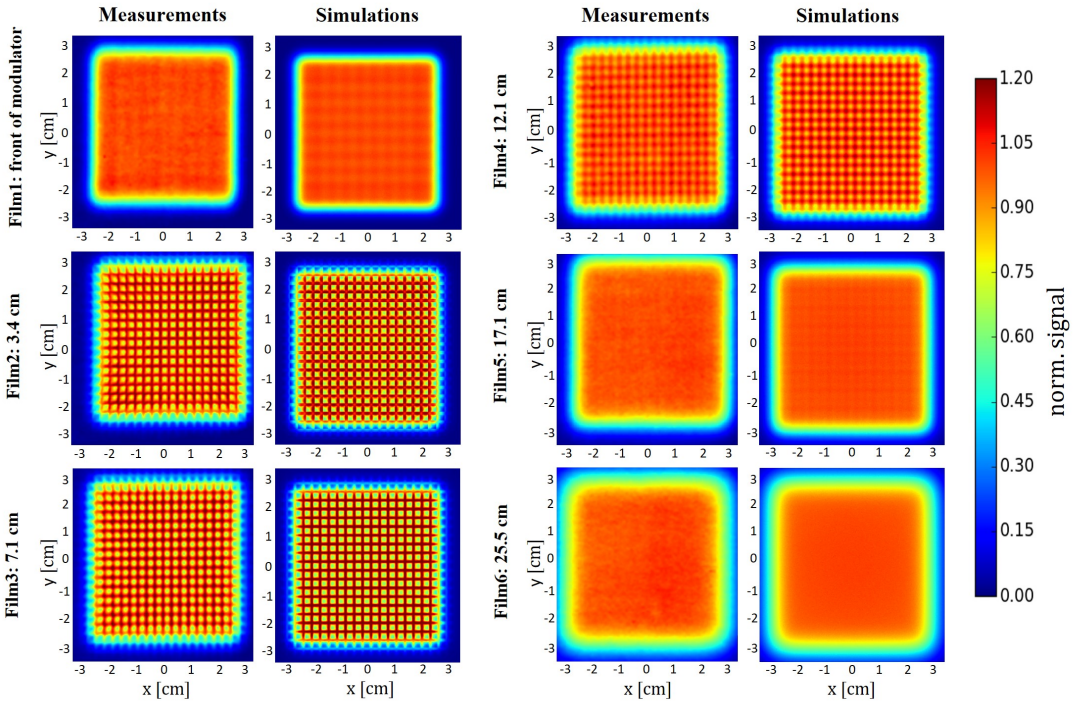

Figure 4.11: Comparisons of 2D fluence profiles from the FLUKA simulations and film measurements for 6 films at 3.4, 7.1, 12.1, 17.1, and 25.5 cm behind the 2DRM and one film in front of the 2DRM.

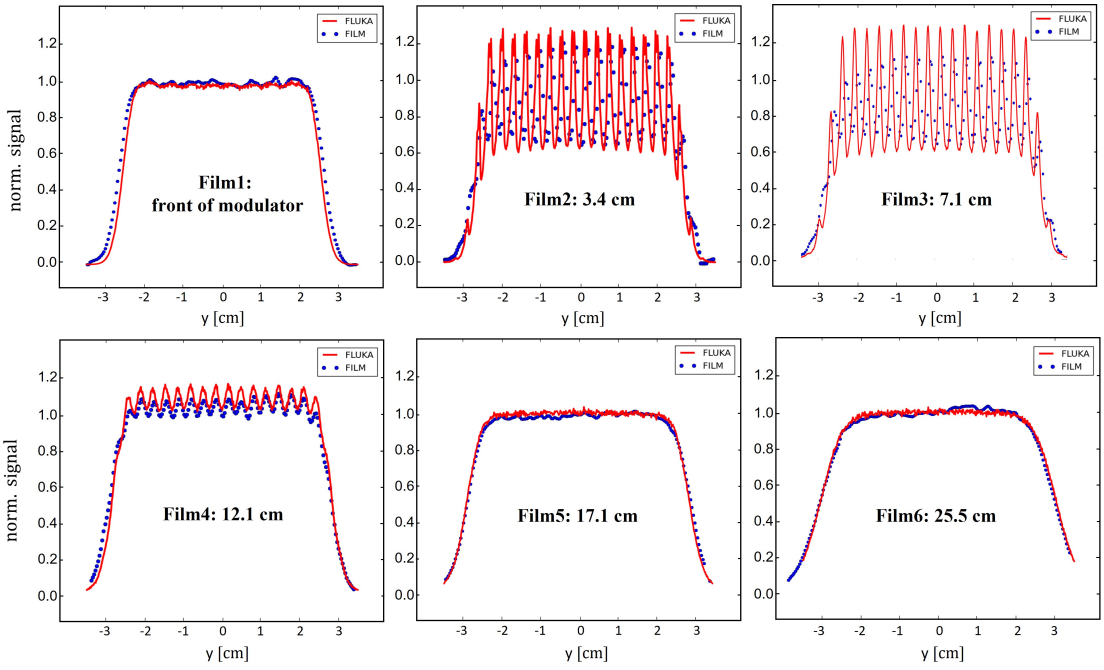

Figure 4.12: Comparisons of shapes of the beam profile from the FLUKA simulations (red solid lines) and film measurements (blue dots) for 6 films at 3.4, 7.1, 12.1, 17.1, and 25.5 cm behind the 2DRM and one film in front of the 2DRM.

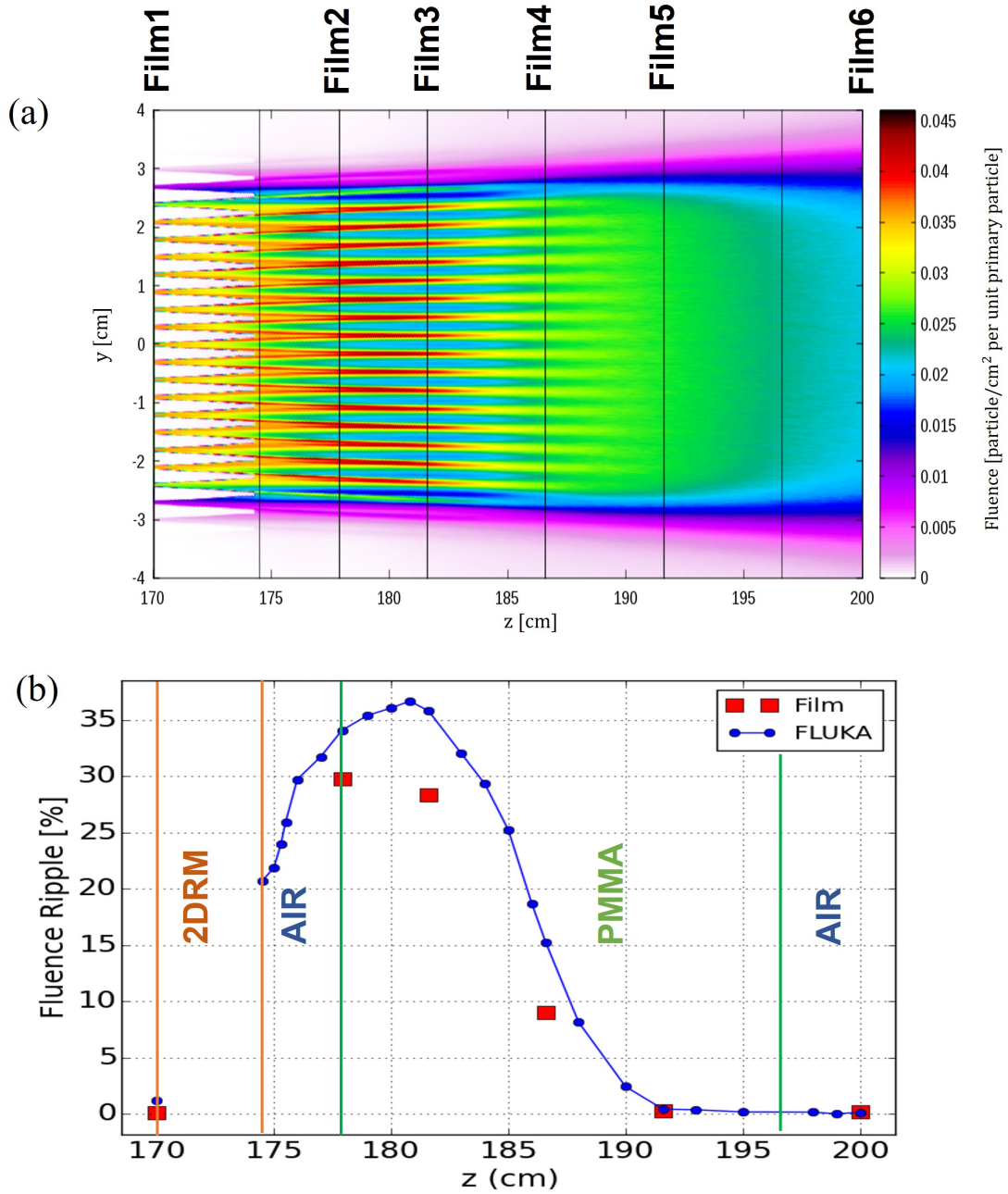

Figure 4.13: Inhomogeneities of the near field behind the modulator spotted in (a) 2D fluence color plot and represented as (b) the fluence ripple function calculated from FLUKA simulation (solid line with blue markers) and film measurement (red squared markers) data.

Although the FLUKA simulated fluence oscillation has the tendency to overestimate the measured values, Figure 4.12 shows that the shapes of the beam field produced by the simulations and measurements fit each other very well which verifies our beam preparation method for the simulation.

Two systematic uncertainties are suspected to be the causes of the deviations in the magnitude of the simulated and measured inhomogeneities. Firstly, the lower resolution of the scanned films data (72 ppi) which is 2.65 times lower compared to the simulations (191 ppi), might underestimate the scanned film data to the simulations because the fluence was averaged over the larger area for one pixel.

The second is a possibly wider angular distribution which might be caused by the additional material in the beamline and the nozzle than considered in the FLUKA model because the increase in the angular distribution can affect the reduction in the fluence ripple (see Figure 4.7). Moreover, the geometry modeling and composition of the material in the beamline can also impact the difference in the particle interactions with the material, including the scattering effect which is directly relevant to the deviation of the fluence ripple. However, the agreement of the enlargement of the beam field between the measurements and the simulations shown in Figure 4.12 can imply the accuracy of the scattering effect in the material in FLUKA. Moreover, the most relevant thing is to know the qualitative development of the inhomogeneity as a function of the depth and to validate at which depth the ripple has completely blurred-out which our FLUKA simulation shows satisfying agreement with the measurement results. Thus, the small deviation in the magnitude of the fluence ripple was not so significant.

Comparison of the Dose Measurement and FLUKA Simulation

Moreover, the measured depth dose distributions in the water phantom were also compared with the FLUKA simulation. Figure 4.14 (a) is the dose distributed on the central axis, and Figure 4.14 (b)) is the fully-integrated depth dose distribution. The deviations of the simulated and measured doses were spotted on the SOBP, the central-axis measured dose is not uniform but declines a bit, while the full integral dose bulges at the middle of the SOBP. This later was found to be caused by an unintended deformation of the 2DRM's pins which affected their modulating function. It should be noted that the pin deformation was probably caused by too warm storage of the modulator. Anyhow, the doses at the proximal build-up and the distal fall-off which are independent of the modulating properties, could be reproduced by FLUKA simulations with a satisfying agreement. This dose agreement can imply the accuracy of the water equivalent thicknesses and properties of the materials added in the virtual beamline as well as the physics model embedded in FLUKA "HADRONther" mode. Hereby, these comparisons of the simulations with the dose measurement results became one of the supporting evidence to validate the FLUKA simulation model.

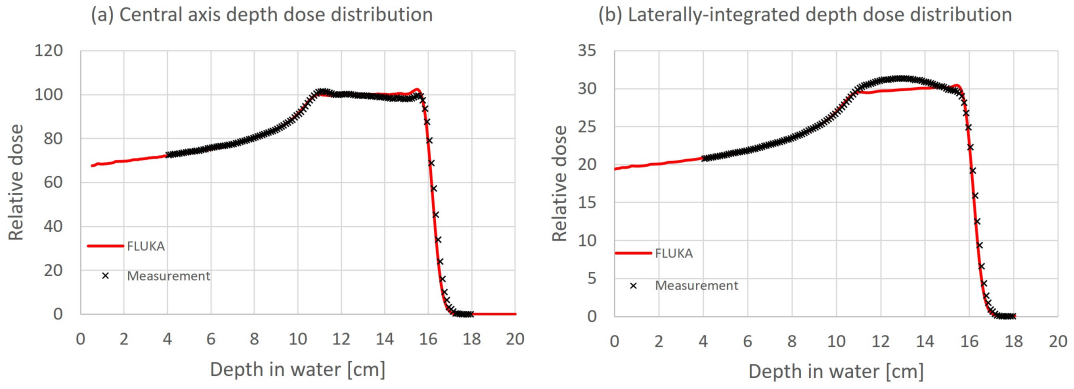

Figure 4.14: Comparisons of the measured (the black crossed markers) and simulated (red solid line) (a) central axis and (b) integral depth dose distributions.

4.3 Near Field Inhomogeneities in the Target for a Clinical Setup

For this simulation, the near field inhomogeneities were simulated by using the clinical setup according to *Varian ProBeam®* as used for reproducing the film measurements in the previous section. Anyhow, the PMMA absorber plates serving for decreasing the proton energy, were taken off in order to put the 2DRM closer to the target. The fluence ripples behind the 2DRM when the modulator was placed 2, 10, 16, and 50 cm in front of the water target were presented in Figure 4.15 (a). Considering the case of 50 cm in which the fluence ripple fully develops in air, the percentage of the fluence ripple at 40 cm, which used to be the determined d_{min} given from the generic testing, is lifted up from 0.06% to 0.82%. This can be explained by the influence of the scanning divergency which was also taken into account for the clinical setup implemented in this simulation. Since the multiple pencil beams were bent off the beam central axis, thus the overlapping of each spot beam is further away compared to the case of parallel beams.

By inspecting the fluence ripple plot which is between the contact of air and water (the slashed markers indicate the water surface), it is clearly seen that the fluence ripples drastically decline after the beam enters the water region which is because of a larger scattering power of water compared to air (mainly due to the much higher density). Hence, the earlier the fluence ripple penetrates in the water, the faster the blurred-out of the field. The dose ripple in water for the different distances of the modulator (Figure 4.15 (b)) also shows that even though the fluence ripple is initially stronger in the case of near field simulation (2 cm behind the 2DRM), the dose ripple converges to zero at the same depth, i.e., 10 cm in water, for every distance between the 2DRM and the water. Moreover, it is exactly the depth of the proximal edge of the SOBP which ensures the reservation of the dose homogeneity in the SOBP region. This is assumed to be the dominant of the strong scattering power of water which accelerates the beam overlapping when the beams start penetrating in water.

Figure 4.16 displays the visualization of the dose ripple in the water, which fades out when the modulator is at the further distance from the water target. Another aspect that is worth mentioning is the decrease in the dose conformity when the modulator is placed far away from the target, which is seen clearly between the

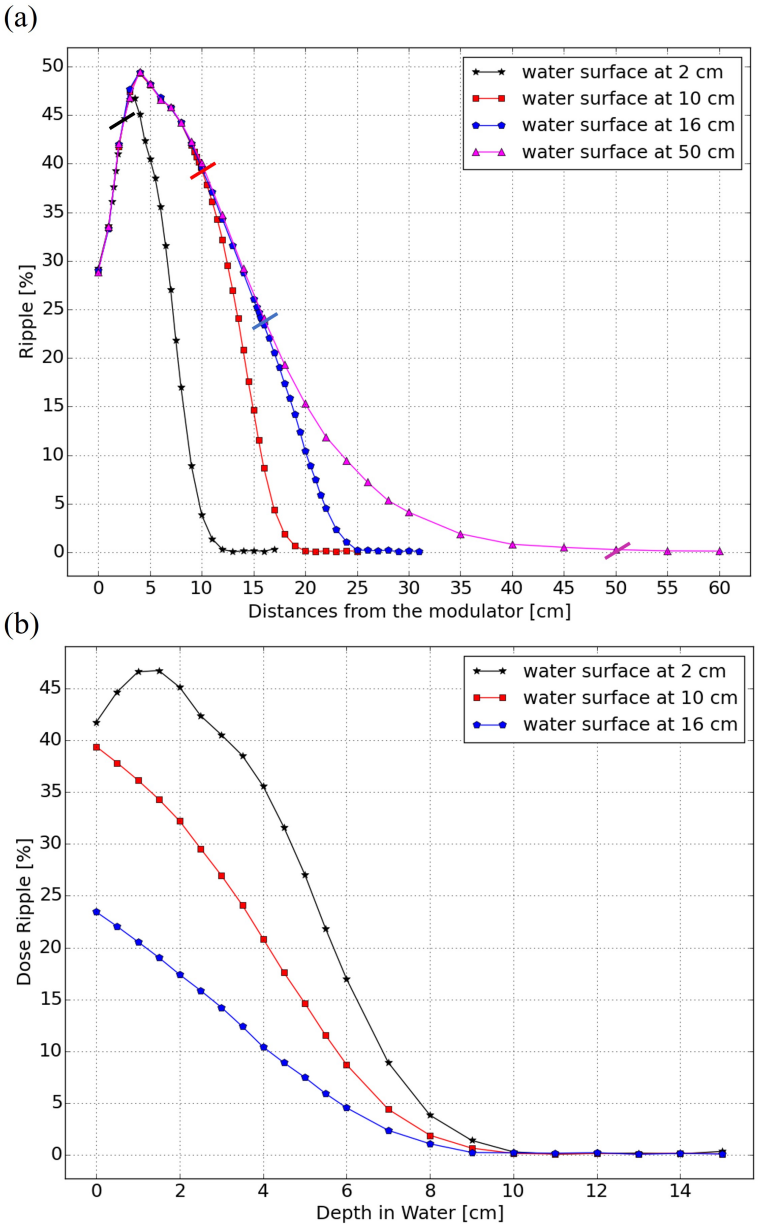

Figure 4.15: (a) Fluence ripple plotted between the contact of air and water which the slashed markers label the position of the water surface and (b) the dose ripple shown only in the water (zoom of fig a after the slash).

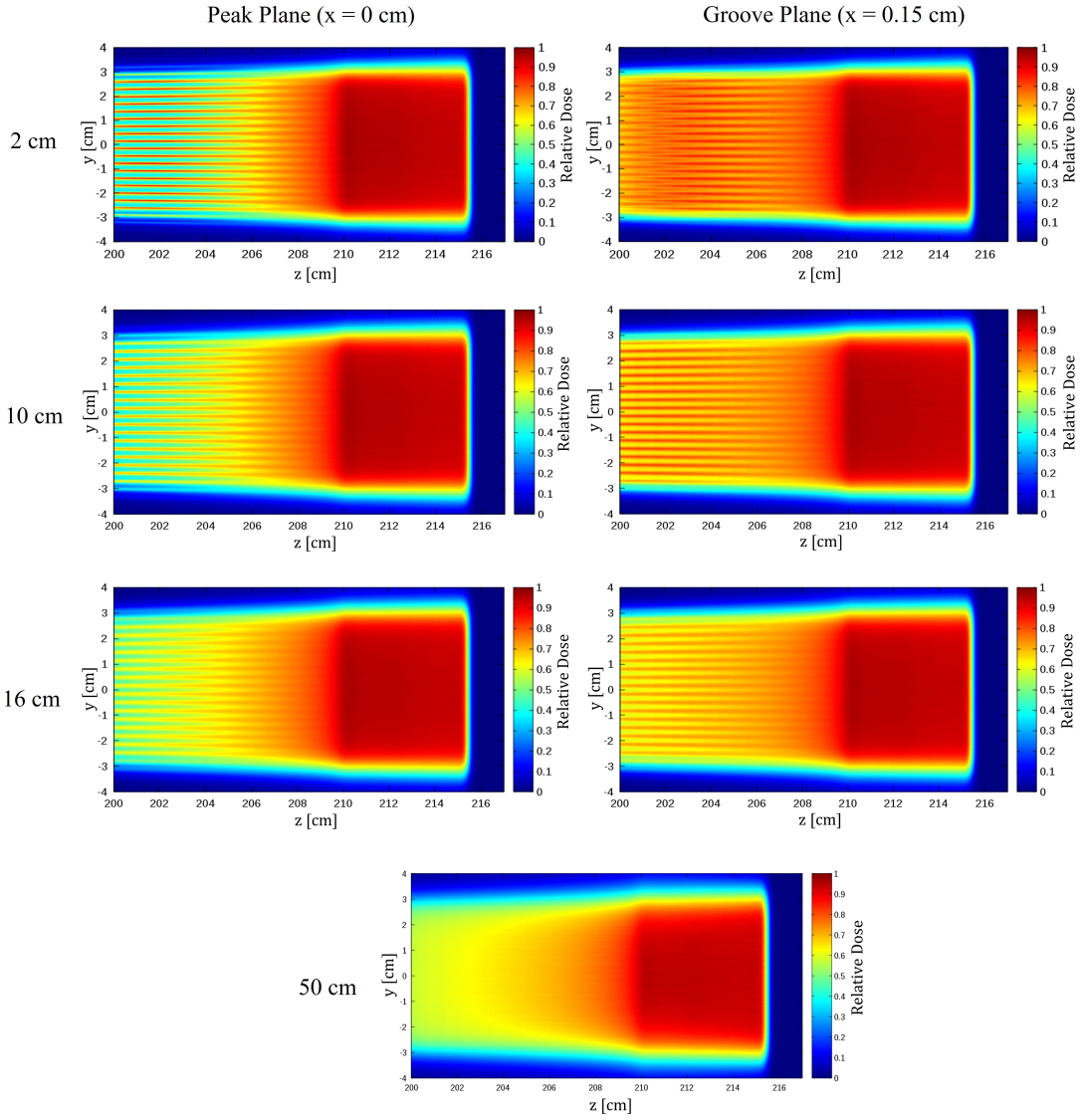

Figure 4.16: 2D dose color plot in groove and peak planes for different distances between the 2DRM and the water, i.e., 2, 10, 16, 50 cm.

cases of 2 cm and 50 cm. For a better comparison, the beam profiles at the middle of the SOBP or at the depth in the water of 12.5 cm (z = 212.5 cm) are compared for the cases of 2 cm and 50 cm which are shown in Figure 4.17. It can be clearly seen that the edge of the beam profile is dropped by 9% and the lateral fall-off sharpness is reduced for the case of 50 cm due to the beam enlargement and the multiple scattering described in section 2.1 regarding elastic scattering. Thus, the 3D-PMs should be as close as possible to the target in order to achieve the best conformation of dose when using the 3D-PMs.

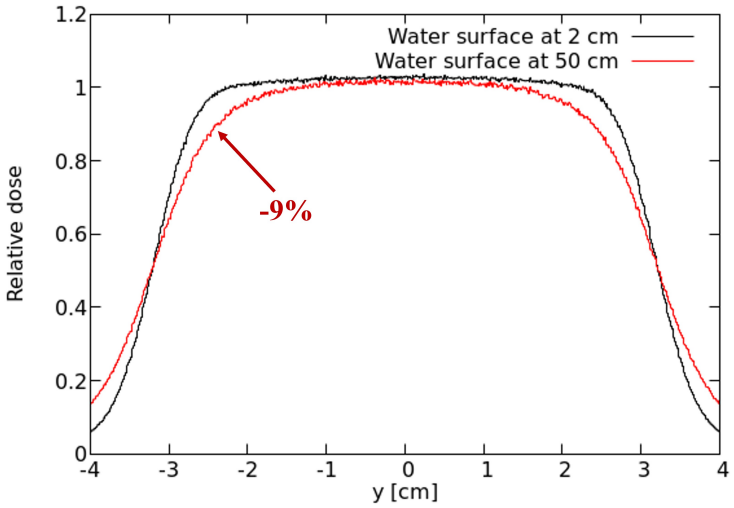

Figure 4.17: Comparison of the dose profiles at the middle of the SOBP (the dept in water of 12.5 cm or z = 212.5 cm) where the 2DRM is at 2 (black line) and 50 (red line) cm in front of the water target.

A Kind of "Minibeam" Dose Pattern for Short Modulator Distances

As mentioned before, an inhomogeneous field is usually undesirable in the case of conventional treatment plans. However, the research on minibeam particle therapy (Meyer et al., 2019) implies the possibility to exploit such a strong dose inhomogeneity for sparing the normal tissue. Figure 4.18 shows the simulated dose distribution in the water phantom when the modulator was placed at a distance of 2

cm in front of the water surface. By performing this way, the lateral dose ripple is presented on the patient's skin and also penetrates for several centimetres into the normal tissue, whereas in the target volume it is blurred-out again. This allows the hypothesis that this kind of strong dose ripple might have a positive "minibeam effect" for the skin and the proximal normal tissue, or at least no deterioration compared to a homogeneous dose application. Figure 4.18 (b) and Figure 4.18 (c) show lateral dose distributions at the water surface where Figure 4.18 (c) is the dose profile at x = 0 cm. The peak and valley of dose were spotted in a similar manner to minibeam which the Peak-to-Valley Ratios (PVDR) at the first 4 cm of the water are between the factor of 2 and 3. However, they are lower than what they normally have been in minibeam studies. Clearly, in order to verify this kind of "soft-minibeam effect", the biological response needs to be investigated in pre-clinical experiments with animals.

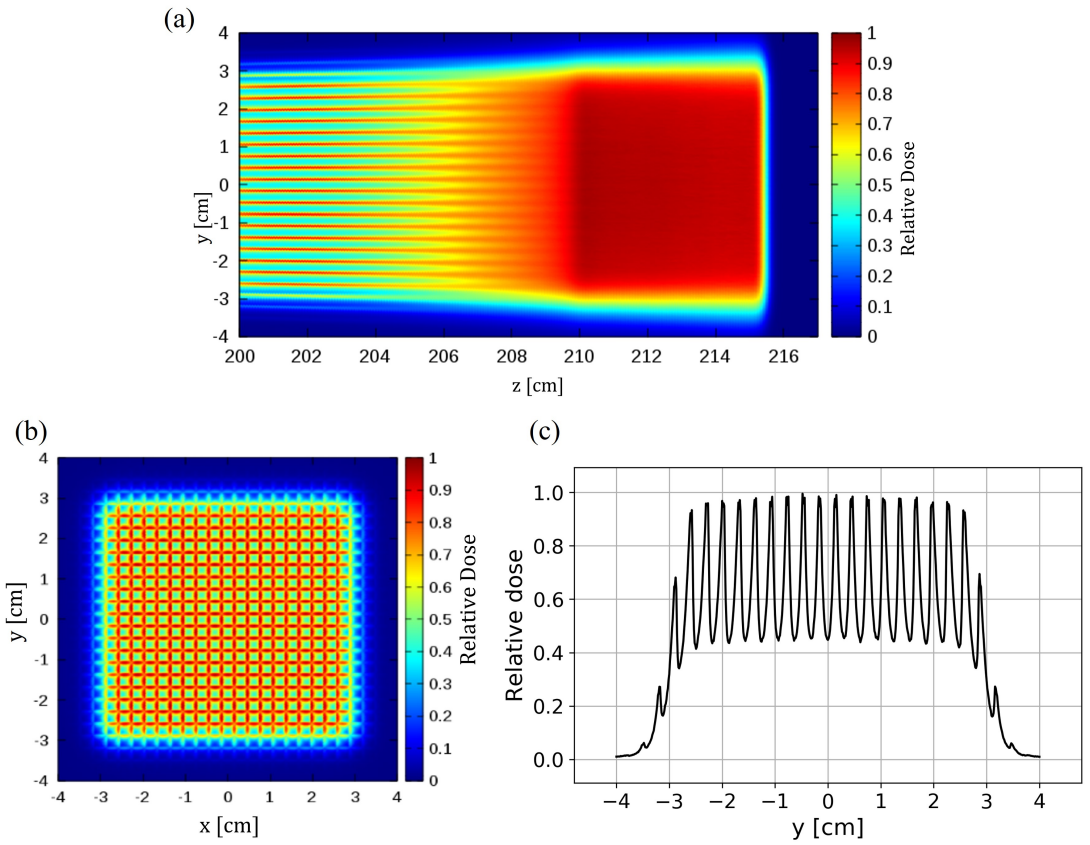

Figure 4.18: Simulated dose inhomogeneities (a) in 2D depth dose distribution, (b) at the water surface, and (c) the dose profile at x = 0 cm when the modulator is placed 2 cm in front of the water.

Chapter V

CONCLUSION

In this work, the field (fluence or dose) inhomogeneity induced by "3D-Printed Modulator (3D-PM)" (Simeonov et al., 2017, 2021) was investigated systematically by using the Monte Carlo simulation package FLUKA (Böhlen et al., 2014) which is considered to be one of the most reliable tools for particle therapy research. For better systematics, we used a simplified version of the 3D-PM, called "2D Range-Modulator (2DRM)" (Simeonov et al., 2021), in which all pins have the same shape and height for the investigation.

To simulate the complicated shape of the "2DRMs" in FLUKA, the user routine written in FORTRAN77 format was developed to cooperatively work with the standard FLUKA executable. Furthermore, the code was also extended to the implementation of "Ripple Filters (RiFis)" as well as was improved to be faster using "interpolation points for the pin's profile" instead of the "ray-triangle intersection algorithm" which was used in the previous work (Simeonov et al., 2017). Not only applicable for our study but this updated routine can be widely used for other research purposes in the field. So far, it has been utilized in particle therapy research at GSI Helmholtzzentrum für Schwerionenforschung and OncoRay – National Center for Radiation Research in Oncology, Germany.

One of the main objectives of this work is to determine the "minimum distance d_{min}" at where the induced inhomogeneity behind the 2DRMs completely fades away. The determination method was adapted from the work of the investigation of the dose inhomogeneity induced by ripple filters, which are a kind of smaller beam modulating devices (Ringbæk et al., 2014). By using this analysis, the field homogeneity was defined as a numerical value, a so-called "fluence ripple", for the purpose of quantitative comparison of the inhomogeneity at different distances behind the modulator. In this work, the fitting function used for determining the fluence ripple was changed from the "single-phase sinusoidal" to the "multiple oscillating" because of the better agreement with the fluence oscillating induced by the 2DRM. After the d_{min} was determined for the tested 2DRM, the dose distribution in water at the determined distance was simulated to verify the complete dose homogeneity in the target. The results show a homogeneous dose with a per-

fect uniform "Spread-Out-Bragg-Peak (SOBP)" which implies a good modulating property of our simulated 2DRM and validates our 2DRM's shape realization and d_{min} determination methods.

Additionally, the testing of the inhomogeneity sensitivity in air shows the strong influence of 2 tested parameters, i.e., the initial beam energy and the pin period of the modulator, which are directly related to the d_{min}. Meanwhile, the variation of the initial angular distribution slightly deviates the fluence ripple function with an inverse relation to the d_{min}, thus it is not significant compared to the other parameters. According to the results tested by suitable values for the treatment plan, the maximum fluence ripple induced by the 2DRM typically locates between 2 and 10 cm and d_{min} is between 30 and 50 cm behind the modulator.

The FLUKA simulations were also verified by radiochromic film measurement and dose measurement. The simulation setup was followed by the experimental setup with the reference of the *Varian ProBeam®* machine. For the comparison with the film measurements, the results show a good qualitative agreement. Even though there are overestimations in the magnitude of the fluence ripple, the inhomogeneities and their dependence on the modulator distance could be well reproduced by the simulations. The results of the dose distributions in the water phantom also agree well with each other at the proximal build-up and distal fall-off of the Bragg curve. However, the modulated peak from the measurement bulges up which is caused by an unintended deformation of the 2DRM'pins affecting its modulating function.

Due to the advantage of the small distance between the modulator and patients in providing a better dose conformation to tumour volume, the last section of the thesis was dedicated to performing near-field simulation with the clinical setup. By performing this way, the strong dose inhomogeneity is present in the proximal part of the water, which is usually unwanted for the conventional treatment plan. However, such fractionated beams might introduce a positive "minibeam" normal-tissue sparing. The Peak-to-Valley-Ratios (PVDR) at the first 4 cm depth in water were calculated which is found out to be lower than what they normally have been in minibeam studies. Nevertheless, the only way to verify this kind of "soft-minibeam effect" is to investigate the biological response in pre-clinical experiments with animals which could be included in future work.

Even though there is a positive assumption supporting the presence of the dose ripple on the proximal part of the tumour, the inhomogeneous dose is still prohibited for the tumour region because of the possible under dosage. The investigation revealed that the SOBP of the low-energy particles (e.g., 100 MeV protons) which traverse in water with a short range is still disturbed by the dose inhomogeneity. For the 2DRM designed for creating a 5 cm SOBP, 150 MeV is the minimum energy that can ultimately exploit the advantage of the small distance setup (the modulator is 2 cm in front of the water phantom) without the interference of the dose inhomogeneity at the SOBP. Even though there is a slight increase in d_{min} in the air for the simulation that considered the scanning divergency, the stronger scattering power of water completely washes out the dose ripple right in front of the proximal edge. Thus 150 MeV is still safe for avoiding the interference of the dose ripple in the target volume.

REFERENCES

Ahlen, S. P. 1980. Theoretical and experimental aspects of the energy loss of relativistic heavily ionizing particles. Reviews of Modern Physics 52.1 (1980): 121.

Akagi, T., Higashi, A., Tsugami, H., Sakamoto, H., Masuda, Y., and Hishikawa, Y. 2003. Ridge filter design for proton therapy at hyogo ion beam medical center. Physics in Medicine & Biology 48.22 (2003): N301.

Akanuma, A., Majima, H., Furukawa, S., Okamoto, R., Nakamura, Y. K., Tsunemoto, H., Morita, S., Arai, T., Kurisu, A., Hiraoka, T., et al. 1982. Compensation techniques in nirs proton beam radiotherapy. International Journal of Radiation Oncology* Biology* Physics 8.9 (1982): 1629–1635.

Barkas, W. H. 1963. Nuclear research emulsions. vol. 1: Techniques and theory. Pure and Applied Physics (1963):

Battistoni, G., Bauer, J., Boehlen, T. T., Cerutti, F., Chin, M. P., Dos Santos Augusto, R., Ferrari, A., Ortega, P. G., Kozłowska, W., Magro, G., et al. 2016. The fluka code: an accurate simulation tool for particle therapy. Frontiers in oncology 6 (2016): 116.

Baumann, K.-S., Horst, F., Zink, K., and Goma, C. 2019. Comparison of penh, fluka, and geant4/topas for absorbed dose calculations in air cavities representing ionization chambers in high-energy photon and proton beams. Medical physics 46.10 (2019): 4639–4653.

Bert, C., Grözinger, S. O., and Rietzel, E. 2008. Quantification of interplay effects of scanned particle beams and moving targets. Physics in Medicine & Biology 53.9 (2008): 2253.

Bethe, H. 1930. Zur theorie des durchgangs schneller korpuskularstrahlen durch materie. Annalen der Physik 397.3 (1930): 325–400.

Bloch, F. 1933. Zur bremsung rasch bewegter teilchen beim durchgang durch materie. Annalen der Physik 408.3 (1933): 285–320.

Böhlen, T., Cerutti, F., Chin, M., Fassò, A., Ferrari, A., Ortega, P. G., Mairani, A., Sala, P. R., Smirnov, G., and Vlachoudis, V. 2014. The fluka code: developments and challenges for high energy and medical applications. Nuclear data sheets 120 (2014): 211–214.

Bohr, N. 1940. Scattering and stopping of fission fragments. Physical Review 58.7 (1940): 654.

Bourhis, J., Sozzi, W. J., Jorge, P. G., Gaide, O., Bailat, C., Duclos, F., Patin, D., Ozsahin, M., Bochud, F., Germond, J.-F., et al. 2019. Treatment of a first patient with flash-radiotherapy. Radiotherapy and oncology 139 (2019): 18–22.

Bragg, W. H. and Kleeman, R. 1904. Lxxiv. on the ionization curves of radium. The London, Edinburgh, and Dublin Philosophical Magazine and Journal of Science 8.48 (1904): 726–738.

Cheung, J., Kudchadker, R. J., Zhu, X. R., Lee, A. K., and Newhauser, W. D. 2010. Dose perturbations and image artifacts caused by carbon-coated ceramic and stainless steel fiducials used in proton therapy for prostate cancer. Physics in Medicine & Biology 55.23 (2010): 7135.

Chu, W., Ludewigt, B., and Renner, T. 1993. Instrumentation for treatment of cancer using proton and light-ion beams. Review of Scientific Instruments 64.8 (1993): 2055–2122.

dos Santos Augusto, R. 2018. On the feasibility of using radioactive ion beams in hadrontherapy: dosimetric and imaging studies. PhD thesis, Munich U.

Elsässer, T., Gemmel, A., Scholz, M., Schardt, D., and Krämer, M. 2009. The relevance of very low energy ions for heavy-ion therapy. Physics in Medicine & Biology 54.7 (2009): N101.

Favaudon, V., Caplier, L., Monceau, V., Pouzoulet, F., Sayarath, M., Fouillade, C., Poupon, M.-F., Brito, I., Hupé, P., Bourhis, J., et al. 2014. Ultrahigh dose-rate flash irradiation increases the differential response between normal and tumor tissue in mice. Science translational medicine 6.245 (2014): 245ra93–245ra93.

Ferrari, A., Ranft, J., Sala, P. R., and Fassò, A. 2005. FLUKA: A multi-particle transport code (Program version 2005). Number CERN-2005-10. Cern.

Goitein, M. 1978. Compensation for inhomogeneities in charged particle radiotherapy using computed tomography. International Journal of Radiation Oncology* Biology* Physics 4.5-6 (1978): 499–508.

Gottschalk, B., Koehler, A., Schneider, R., Sisterson, J., and Wagner, M. 1993. Multiple coulomb scattering of 160 mev protons. Nuclear Instruments and Methods in Physics Research Section B: Beam Interactions with Materials and Atoms 74.4 (1993): 467–490.

Haberer, T., Becher, W., Schardt, D., and Kraft, G. 1993. Magnetic scanning system for heavy ion therapy. Nuclear Instruments and Methods in Physics Research Section A: Accelerators, Spectrometers, Detectors and Associated Equipment 330.1-2 (1993): 296–305.

Highland, V. L. 1975. Some practical remarks on multiple scattering. Nuclear Instruments and Methods 129.2 (1975): 497–499.

Highland, V. 1979. Erratum nucl. instrum. Methods 161 (1979): 171.

Holm, K. M., Weber, U., Simeonov, Y., Krauss, A., Jäkel, O., and Greilich, S. 2020. 2d range modulator for high-precision water calorimetry in scanned carbon-ion beams. Physics in Medicine & Biology 65.21 (2020): 215003.

Hopewell, J. W. and Trott, K.-R. 2000. Volume effects in radiobiology as applied to radiotherapy. Radiotherapy and Oncology 56.3 (2000): 283–288.

Iancu, G., Kraemer, M., Zink, K., Durante, M., and Weber, U. 2015. Implementation of an efficient monte carlo algorithm in trip: physical dose calculation. International journal of particle therapy 2.2 (2015): 415–425.

Jolly, S., Owen, H., Schippers, M., and Welsch, C. 2020. Technical challenges for flash proton therapy. Physica Medica 78 (2020): 71–82.

Klyachko, A. V. 2017. Gem-based dose imaging detectors for proton therapy quality assurance and proton radiography. Q Phys Rev 3 (2017):

Koehler, A., Schneider, R., and Sisterson, J. 1977. Flattening of proton dose distributions for large-field radiotherapy. Medical Physics 4.4 (1977): 297–301.

Kraft, G. 2000. Tumor therapy with heavy charged particles. Progress in particle and Nuclear Physics 45 (2000): S473–S544.

Kumazaki, Y., Akagi, T., Yanou, T., Suga, D., Hishikawa, Y., and Teshima, T. 2007. Determination of the mean excitation energy of water from proton beam ranges. Radiation Measurements 42.10 (2007): 1683–1691.

Lambert, J., Suchowerska, N., McKenzie, D., and Jackson, M. 2005. Intrafractional motion during proton beam scanning. Physics in Medicine & Biology 50.20 (2005): 4853.

Lewis, D., Micke, A., Yu, X., and Chan, M. F. 2012. An efficient protocol for radiochromic film dosimetry combining calibration and measurement in a single scan. Medical physics 39.10 (2012): 6339–6350.

Lindsay, C., Kumlin, J., Jirasek, A., Lee, R., Martinez, D., Schaffer, P., and Hoehr, C. 2015. 3d printed plastics for beam modulation in proton therapy. Physics in Medicine & Biology 60.11 (2015): N231.

Lindsay, C., Kumlin, J., Martinez, D., Jirasek, A., and Hoehr, C. 2016. Design and application of 3d-printed stepless beam modulators in proton therapy. Physics in Medicine & Biology 61.11 (2016): N276.

Meyer, J., Eley, J., Schmid, T. E., Combs, S. E., Dendale, R., and Prezado, Y. 2019. Spatially fractionated proton minibeams. The British journal of radiology 92.1095 (2019): 20180466.

Micke, A., Lewis, D. F., and Yu, X. 2011. Multichannel film dosimetry with nonuniformity correction. Medical physics 38.5 (2011): 2523–2534.

Moliere, G. 1948. Theorie der streuung schneller geladener teilchen ii mehrfach- und vielfachstreuung. Zeitschrift für Naturforschung A 3.2 (1948): 78–97.

Newhauser, W., Fontenot, J., Koch, N., Dong, L., Lee, A., Zheng, Y., Waters, L., and Mohan, R. 2007. Monte carlo simulations of the dosimetric impact of radiopaque fiducial markers for proton radiotherapy of the prostate. Physics in Medicine & Biology 52.11 (2007): 2937.

Newhauser, W. D. and Zhang, R. 2015. The physics of proton therapy. Physics in Medicine & Biology 60.8 (2015): R155.

Niita, K., Sato, T., Iwase, H., Nose, H., Nakashima, H., and Sihver, L. 2006. Phits —a particle and heavy ion transport code system. Radiation measurements 41.9-10 (2006): 1080–1090.

Paul, H. 2007. The mean ionization potential of water, and its connection to the range of energetic carbon ions in water. Nuclear Instruments and Methods in Physics Research Section B: Beam Interactions with Materials and Atoms 255.2 (2007): 435–437.

Pedroni, E., Bacher, R., Blattmann, H., Böhringer, T., Coray, A., Lomax, A., Lin, S., Munkel, G., Scheib, S., Schneider, U., et al. 1995. The 200-mev proton therapy project at the paul scherrer institute: Conceptual design and practical realization. Medical physics 22.1 (1995): 37–53.

Reidel, C.-A., Horst, F., Schuy, C., Jäkel, O., Ecker, S., Henkner, K., Brons, S., Durante, M., and Weber, U. 2022. Experimental comparison of fiducial markers used in proton therapy: Study of different imaging modalities and proton fluence perturbations measured with cmos pixel sensors. Frontiers in Oncology (2022):

Ringbæk, T. P., Weber, U., Petersen, J. B., Thomsen, B., and Bassler, N. 2014. Monte carlo simulations of new 2d ripple filters for particle therapy facilities. Acta Oncologica 53.1 (2014): 40–49.

Ringbæk, T. P., Weber, U., Santiago, A., Iancu, G., Wittig, A., Grzanka, L., Bassler, N., Engenhart-Cabillic, R., and Zink, K. 2018. Validation of new 2d ripple filters in proton treatments of spherical geometries and non-small cell lung carcinoma cases. Physics in Medicine & Biology 63.24 (2018): 245020.

Sammer, M., Greubel, C., Girst, S., and Dollinger, G. 2017. Optimization of beam arrangements in proton minibeam radiotherapy by cell survival simulations. Medical physics 44.11 (2017): 6096–6104.

Schardt, D., Steidl, P., Krämer, M., Weber, U., Parodi, K., and Brons, S. 2007. Precision bragg-curve measurements for light-ion beams in water. GSI Scientific Report 373 (2007):

Schardt, D., Elsässer, T., and Schulz-Ertner, D. 2010. Heavy-ion tumor therapy: Physical and radiobiological benefits. Reviews of modern physics 82.1 (2010): 383.

Schuy, C., Simeonov, Y., Durante, M., Zink, K., and Weber, U. 2020. Vendor-agnostic water phantom for 3d dosimetry of complex fields in particle therapy. Journal of Applied Clinical Medical Physics 21.10 (2020): 227–232.

Serber, R. 1947. Nuclear reactions at high energies. Physical Review 72.11 (1947): 1114.

Simeonov, Y., Weber, U., Penchev, P., Ringbæk, T. P., Schuy, C., Brons, S., Engenhart-Cabillic, R., Bliedtner, J., and Zink, K. 2017. 3d range-

modulator for scanned particle therapy: development, monte carlo simulations and experimental evaluation. Physics in Medicine & Biology 62.17 (2017): 7075.

Simeonov, Y., Weber, U., Schuy, C., Engenhart-Cabillic, R., Penchev, P., Durante, M., and Zink, K. 2021. Monte carlo simulations and dose measurements of 2d range-modulators for scanned particle therapy. Zeitschrift für Medizinische Physik 31.2 (2021): 203–214.

Simeonov, Y., Weber, U., Schuy, C., Engenhart-Cabillic, R., Penchev, P., Flatten, V., and Zink, K. 2022. Development, monte carlo simulations and experimental evaluation of a 3d range-modulator for a complex target in scanned proton therapy. Biomedical Physics & Engineering Express 8.3 (2022): 035006.

Sorriaux, J., Kacperek, A., Rossomme, S., Lee, J. A., Bertrand, D., Vynckier, S., and Sterpin, E. 2013. Evaluation of gafchromic® ebt3 films characteristics in therapy photon, electron and proton beams. Physica Medica 29.6 (2013): 599–606.

Tinganelli, W., Sokol, O., Quartieri, M., Puspitasari, A., Dokic, I., Abdollahi, A., Durante, M., Haberer, T., Debus, J., Boscolo, D., et al. 2022a. Ultra-high dose rate (flash) carbon ion irradiation: dosimetry and first cell experiments. International Journal of Radiation Oncology* Biology* Physics 112.4 (2022): 1012–1022.

Tinganelli, W., Weber, U., Puspitasari, A., Simoniello, P., Abdollahi, A., Oppermann, J., Schuy, C., Horst, F., Helm, A., Fournier, C., et al. 2022b. Flash with carbon ions: Tumor control, normal tissue sparing, and distal metastasis in a mouse osteosarcoma model. Radiotherapy and Oncology (2022):

Tommasino, F., Rovituso, M., Bortoli, E., La Tessa, C., Petringa, G., Lorentini, S., Verroi, E., Simeonov, Y., Weber, U., Cirrone, P., et al. 2019. A new facility for proton radiobiology at the trento proton therapy centre: Design and implementation. Physica Medica 58 (2019): 99–106.

Torikoshi, M., Minohara, S., Kanematsu, N., Komori, M., Kanazawa, M., Noda, K., Miyahara, N., Itoh, H., Endo, M., and Kanai, T. 2007. Irradiation system for himac. Journal of radiation research 48.Suppl_A (2007): A15–A25.

Tsai, Y.-S. 1974. Pair production and bremsstrahlung of charged leptons. Reviews of Modern Physics 46.4 (1974): 815.

Valentin, J. 2008. The 2007 recommendations of the international commission on radiological protection. Elsevier International Commission on Radiological Protection.

Van De Water, S., Safai, S., Schippers, J. M., Weber, D. C., and Lomax, A. J. 2019. Towards flash proton therapy: the impact of treatment planning and machine characteristics on achievable dose rates. Acta oncologica 58.10 (2019): 1463–1469.

Vavilov, P. 1957. Ionization losses of high-energy heavy particles. Soviet Phys. JETP 5 (1957):

Vozenin, M.-C., De Fornel, P., Petersson, K., Favaudon, V., Jaccard, M., Germond, J.-F., Petit, B., Burki, M., Ferrand, G., Patin, D., et al. 2019. The advantage of flash radiotherapy confirmed in mini-pig and cat-cancer patientsthe advantage of flash radiotherapy. Clinical Cancer Research 25.1 (2019): 35–42.

Weber, U. and Kraft, G. 1999. Design and construction of a ripple filter for a smoothed depth dose distribution in conformal particle therapy. Physics in Medicine & Biology 44.11 (1999): 2765.

Weber, U. and Kraft, G. 2009. Comparison of carbon ions versus protons. The Cancer Journal 15.4 (2009): 325–332.

Weber, U. A., Scifoni, E., and Durante, M. 2022. Flash radiotherapy with carbon ion beams. Medical Physics 49.3 (2022): 1974–1992.

WHO, W. H. O. Cancer. `https://www.who.int/news-room/fact-sheets/detail/cancer`.

Wilson, P., Jones, B., Yokoi, T., Hill, M., and Vojnovic, B. 2012. Revisiting the ultra-high dose rate effect: implications for charged particle radiotherapy using protons and light ions. The British journal of radiology 85.1018 (2012): e933–e939.

Yokoi, T., Cobb, J., Ken Peach, J., Morgan, G., Pozimski, J., and Easton, M. 2008. Beam injection issues of ffag for particle therapy. In Proceedings of EPAC, volume 8, p. p3401. :

Appendix I

EXTENDED ACKNOWLEDGEMENTS

I would like to thank my tutors from the radiation protection department of GSI: Dr. Ekaterina Kozlova, Dr. Alexey Sokolov, and Dr. Alexey Evdokimov, for the knowledge of FLUKA simulation, which gave me a great benefit to start off the work of this thesis with more ease. I would like to especially thank Dr. Alexey Sokolov for the FORTRAN guidance and for providing me with the executable FLUKA routine.

I appreciate the great company from the researchers in the biophysics division of GSI, especially Dr. Tabea Pfuhl, Dr. Daria Boscolo, Dr. Francesca Luoni, Dr. Tim Wagner, Lévana Gesson, and Wilfried Kraemer from the radiation physics group of GSI. I also would like to thank Dr. Tabea Pfuhl for introducing me to Python which saved me a lot of time from learning the code from scratch.

I am sincerely grateful to Mr. Tanawat Tawonwong, Dr. Ekaterina Kozlova, and Dr. Alexey Sokolov for their kind recommendation of me, which paved the way for working on this thesis in the GSI radiation physics group.

I thank my colleagues from the Particle Physics Research Laboratory of Chulalongkorn University for their valuable comments and suggestions on the research work, as well as the advice and encouragement on my master's student journey.

I thank all the staff of the science faculty, especially Ms. Varina Suphakosol and Ms. Wipawa Pinitsaksiri for taking care of my documents for the research grant, which made my research journey to Germany possible.

I also would like to express my deep gratitude to Dr. Rujikorn Dhanawittayapol for his constant support, advice, and attention to my academic life, which helped me keep up with the schedule.

Lastly, I would like to thank my family from the bottom of my heart for their sympathy and unlimited love for me. Thank them for the good food and the good living environment, which help me work effectively. Thank you to all of my cats for always recharging my batteries after hours of working with their adorableness.

Biography

Warisara Charuchinda was born in Bangkok on 19th April 1997. She graduated from Streesmutprakan School and then went to Chulalongkorn University, where she received a B.Sc in physics. Her field of interest includes various topics in high energy physics and its application to charged particle therapy. She has been granted a scholarship by the Development and Promotion of Science and Technology Talents Project (DPST) since 2016.

In 2019, she attended the International Summer Student Program at GSI-FAIR, Germany, working in the field of radiation protection. Later, in 2022, she did an internship in the radiation physics group, biophysics division at GSI Helmholtzzentrum für Schwerionenforschung, where a research project in this thesis was conducted.